Federal University of Minas Gerais
Graduate Program in Physics

Matheus Felipe de Souza Barbosa

Growth temperature effects on the structural and magnetic properties of ferromagnetic nanostructures self-assembled on vicinal surface Ag(977)

Belo Horizonte
2021

Matheus Felipe de Souza Barbosa

Growth temperature effects on the structural and magnetic properties of ferromagnetic nanostructures self-assembled on vicinal surface Ag(977)

Dissertation presented to Graduate Program in Physics of Universidade Federal de Minas Gerais in partial fulfillment of the requirement for the degree of master of science in physics.

Advisor: Prof. Dr. Roberto Magalhães Paniago

Belo Horizonte
2021

Dados Internacionais de Catalogação na Publicação (CIP)

B238g Barbosa, Matheus Felipe de Souza.
Growth temperature effects on the structural and magnetic properties of ferromagnetic nanostructures self-assembled on vicinal surface Ag(977) / Matheus Felipe de Souza Barbosa. – 2021.
100f., enc. : il.

Orientador: Roberto Magalhães Paniago.
Dissertação (mestrado) – Universidade Federal de Minas Gerais, Departamento de Física.
Bibliografia: f. 92-100.

1. Matéria condensada. 2. Física de superfície. 3. Magnetismo.
I. Título. II. Paniago, Roberto Magalhães. III. Universidade Federal de Minas Gerais, Departamento de Física.

CDU – 538.911 (043)

Ficha catalográfica elaborada por Romário Martins – CRB6 3595
Biblioteca Professor Manoel Lopes de Siqueira – Departamento de Física - UFMG

UNIVERSIDADE FEDERAL DE MINAS GERAIS
INSTITUTO DE CIÊNCIAS EXATAS
PROGRAMA DE PÓS-GRADUAÇÃO EM FÍSICA

FOLHA DE APROVAÇÃO

A presente dissertação, intitulada **"Growth temperature effects on the structural and magnetic properties of ferromagnetic nanostructures self-assembled on vicinal surface Ag(977)",** de autoria de **MATHEUS FELIPE DE SOUZA BARBOSA**, submetida à Comissão Examinadora, abaixo-assinada, foi aprovada para obtenção do grau de **MESTRE EM FÍSICA** em 05 de maio de 2021.

Belo Horizonte, 05 de maio de 2021.

Prof. Roberto Magalhães Paniago

Orientador do estudante

Departamento de Fisica/UFMG

Prof. Edmar Avellar Soares

Departamento de Física/UFMG

Prof. Luis Eugênio Fernandez Outon

Departamento de Física/UFMG

Documento assinado eletronicamente por **Roberto Magalhaes Paniago**, **Professor do Magistério Superior**, em 06/05/2021, às 09:05, conforme horário oficial de Brasília, com fundamento no art. 5º do Decreto nº 10.543, de 13 de novembro de 2020.

Documento assinado eletronicamente por **Luis Eugenio Fernandez Outon**, **Professor do Magistério Superior**, em 06/05/2021, às 09:53, conforme horário oficial de Brasília, com fundamento no art. 5º do Decreto nº 10.543, de 13 de novembro de 2020.

Documento assinado eletronicamente por **Edmar Avellar Soares**, **Professor do Magistério Superior**, em 13/05/2021, às 12:54, conforme horário oficial de Brasília, com fundamento no art. 5º do Decreto nº 10.543, de 13 de novembro de 2020.

A autenticidade deste documento pode ser conferida no site https://sei.ufmg.br/sei/controlador_externo.php?acao=documento_conferir&id_orgao_acesso_externo=0, informando o código verificador **0709089** e o código CRC **40D43701**.

Referência: Processo nº 23072.222960/2021-13 SEI nº 0709089

"If time and space can be known by intuition, each in itself and regardless of matter, this, on the contrary, can not be perceived without them. But matter has no condition time and space considered separately; It's the combination of them that constitutes its essence, residing entirely in activity and causality. Indeed, all phenomena and all possible states, which are innumerable, could, without disturb each other, coexist in infinite space, and, on the other hand, to succeed without difficulty in infinity of time."

The World as Will and Representation (1818/1819)
Arthur Schopenhauer

Acknowledgements

Um trabalho nunca é realizado sozinho e durante o meu estudo de mestrado, enfrentei diversas dificuldades que não poderiam ter sido vencidas sem ajuda de algumas pessoas. Primeiro de tudo, sou muito grato aos meus pais e meu irmão, que sempre me ajudaram quando foi necessário e aos parentes distantes por parte de mãe, que estiveram torcendo pelo meu sucesso.

No âmbito profissional, há um grupo de pessoas que foram fundamentais para a conclusão deste trabalho. Ao meu orientador, o professor Roberto Magalhães Paniago, que com seu conhecimento surpreendente e paciência acima da média, ensinou-me a pensar como físico e a fazer ciência experimental, explicando desde coisas básicas às situações mais complexas dentro de um laboratório. Ao meu colega Dr. Gustavo Fóscolo, que conhece magnetismo como poucos, ajudando-me a superar vários problemas experimentais do dia a dia. Aos professores Edmar Avellar e Vagner Eustáquio que, sendo vizinhos de laboratório, sempre ajudaram quando foram requisitados.

Em especial, necessito fazer agradecimentos aos professores e colegas que foram extremamente importantes no meu percurso acadêmico, entre eles: à Marília e Ana, secretárias da Pós-Graduação, que não mediram esforços para ajudar, sempre que eu precisava. À professora Simone Silva Alexandre, por ser uma coordenadora de pós-graduação sempre presente e atuante. À Gislene, bibliotecária, que sempre me recomendou aquele livro perfeito que eu não sabia que estava procurando. À Creuza, auxiliar de serviços gerais, por manter o laboratório sempre organizado e pelas conversas quase diárias nas primeiras horas da manhã. Aos professores Flávio Garcia e Alberto Passos Guimarães do Centro Brasileiro de Pesquisas Físicas, que me ensinaram muito sobre nanomagnetismo. Ao professores Wagner José Corradi Barbosa, Lucas Álvares da Silva Mol, Luiz Paulo Ribeiro Vaz e Gustavo Guerrero Eraso, por ensinarem tudo o que sei sobre programação de computadores e física computacional, que tem se mostrado um conhecimento para a vida toda. Ao meu colega de astrofísica, Filipe Andrade, pelas discussões quase diárias sobre futebol. Aos professores de pós-graduação Leandro Malard, Ronald Dickman e João Plascak que foram essenciais para meu melhor entendimento de física. Aos professores Nivaldo Lucio Speziali e Nelson de Oliveira Yokomizo que ensinaram e exigiram não menos do que rigor matemático e físico nos meus trabalhos. Aos professores Juan Carlos González Pérez e Klaus Krambrock que foram muito importantes durante minha transição entre graduação e pós-graduação, dando conselhos e dicas na sala do café ou nas conversas pelos corredores. E por último, mas não menos importante, ao CNPq e à Capes pelo fomento durante minha pesquisa.

Abstract

The use of thin films, and more recently of nanostructures, to optimize physical and chemical properties of materials is ubiquitous nowadays. In this context, the deposition of ultrathin films on vicinal surfaces has been an area of great scientific curiosity, given that the periodic arrangement of substrate steps in nanometric scale can lead to the ordered growth of nanostructures, and such self-organization has great technological appeal. In particular, low dimensional ferromagnetic systems have received great attention due to promising applications in magnetic memory devices and spintronics. In order to improve the understanding of these systems, here we investigate the effects of the growth temperature on the structural and magnetic properties of ultrathin iron (Fe) and cobalt (Co) ferromagnetic films on vicinal Ag(977). A few monolayers (ML) were slowly deposited by molecular beam epitaxy (MBE) between 0.5 ML and 5.0 ML. *In-situ* analysis techniques were used, such as low energy electron diffraction (LEED), scanning tunneling microscopy (STM) and magneto-optical Kerr effect (MOKE). For Fe/Ag(977) grown at room temperature, in the 2.0 ML to 5.0 ML range, we observe the formation of elongated nanostructures ("nanowires") of Fe aligned with the step edges of the vicinal surface. At 500 K, between 1.0 ML and 3.0 ML, the growth of triangular structures was observed, most probably with surface alloy formation among the thin film and the substrate. For Co/Ag(977) samples grown at 500 K, for lower thickness, we observe the formation of triangular structures, suggesting Co stacking fault (FCC) on the Ag(111) terraces, and hexagonal structures due to Co-HCP stacking for higher thickness. From the point of view of magnetic properties, which were investigated by MOKE, we have observed from a thickness of 3.0 ML Fe on Ag(977) the presence of a distinguished ferromagnetic signal, when compared to the substrate diamagnetic signal. Nevertheless, for Co/Ag(977) a ferromagnetic signature was already present from 2.0 ML. Both systems have shown strong anisotropies and the experimental results indicate that the easy magnetization axis is in-plane and aligned with the steps, while the hard axis is out-of-plane. Furthermore, the coercive field strength has a dependence with the in-plane angle (ϕ) of the applied magnetic field, with a minimum value when aligned to the steps, which is in line with the nano-structured arrangement observed by STM.

Keywords: Condensed Matter; Surfaces and Interfaces Physics; Ag(977) Vicinal Surface; Magnetism and Matter;

Resumo

O emprego de filmes finos, e mais recentemente de nanoestruturas, para otimizar propriedades físicas e químicas de materiais é onipresente no mundo atual. Nesse contexto, a deposição de filmes ultrafinos sobre superfícies vicinais tem sido uma área de grande curiosidade científica, dado que o arranjo periódico de degraus do substrato em escala nanométrica pode levar ao crescimento ordenado de nanoestruturas, e tal auto-organização tem grande potencial tecnológico. Em especial, sistemas ferromagnéticos de baixa dimensionalidade tem recebido grande atenção devido a promissoras aplicações em dispositivos de memória magnética e em spintrônica. Com o objetivo de melhorar o entendimendo destes sistemas, neste trabalho investigamos os efeitos da temperatura de crescimento nas propriedades estruturais e magnéticas de filmes ferromagnéticos ultrafinos de ferro (Fe) e cobalto (Co) em superfície vicinal Ag(977). Foram depositadas poucas monocamadas (ML) através de evaporação lenta via epitaxia por feixe molecular (MBE- *molecular beam epitaxy*) entre 0.5 ML e 5.0 ML. Foram empregadas técnicas *in-situ* de análise, tais como, difração de elétrons (LEED - *low energy electron diffraction*), microscopia de tunelamento por varredura (STM - *Scanning Tunneling Microscopy*) e efeito Kerr magneto-óptico (MOKE - *magneto optical Kerr effect*). Para amostras de Fe/Ag(977) crescidas a temperatura ambiente, na faixa entre 2.0 ML e 5.0 ML, observamos a formação de nano-estruturas alongadas ("nanofios") de Fe alinhadas com os degraus da superfície vicinal. A 500 K, entre 1.0 ML e 3.0 ML, observou-se o crescimento de estruturas triangulares, muito provavelmente com formação de liga superficial entre o filme fino e o substrato. Para as amostras de Co/Ag(977) crescidas a 500 K, para coberturas mais baixas observamos a formação de estruturas triangulares, sugerindo falha de empilhamento (FCC) do Co sobre os terraços Ag(111), e de estruturas hexagonais próprias de HCP para coberturas mais altas. Do ponto de vista das propriedades magnéticas investigadas via técnica MOKE, observamos a partir de 3.0 ML Fe/Ag(977) a presença de um sinal ferromagnético significativo, quando comparado ao sinal diamagnético do substrato. Contudo, para Co/Ag(977) uma assinatura ferromagnética já se faz presente a partir de 2.0 ML. Ambos os sistemas apresentaram forte anisotropias e as medidas experimentais indicaram que o eixo fácil permanece no plano e alinhado com os degraus, e o eixo duro fora no plano. Além disso, o campo coercivo apresenta dependência com respeito ao ângulo planar (ϕ) do campo magnético aplicado, com um valor mínimo quando alinhado aos degraus, em consonância com o arranjo nanoestruturado observado por STM.

Keywords: Matéria Condensada; Física de Superfícies e Interfaces; Superfície Vicinal Ag(977); Magnetismo e Matéria;

Contents

List of figures

List of table

Chapter 1

Introduction and motivation

In the last decades several physical phenomena caused by reduced dimensionality have been observed on thin films and nanomagnetic structures grown over metallic surfaces. Among them, stands out the giant magnetoresistence (GMR) observed in heterostructures composed by magnetic and non-magnetic layers.[1] From theoretical and experimental studies the magnetic behavior related to surface assymetries, spin reorientation transitions (SRT) and the anisotropy has been increasingly understood. The magnetic anisotropy is related to the magnetic energy due to strong molecular field caused by the exchange interaction between nearest neighbors atoms.[2,3]

In this context a large number of magnetic nanostructures has been employed in several scientific areas such as diagnostics of health disease,[4] storage media and spintronic devices. Within the scope of health research, in the last years, the technique of magnetic hyperthermia has been used as a novel tool against cancer cells. In this technique, magnetic nanoparticles are inserted into tumor cells and then an alternated magnetic field interacts with them inducing an increase of temperature (over 40°C) destroying, therefore, the external membrane of that cell[5–7] as shown in figure 1.1.a. On the other hand, magnetic thin films have been used for decades in the industry to improve the capacity of density storage media[8] and to development novel ways to record information as magnetic random access memory[9,10] as shown for instance in figure 1.1.b.

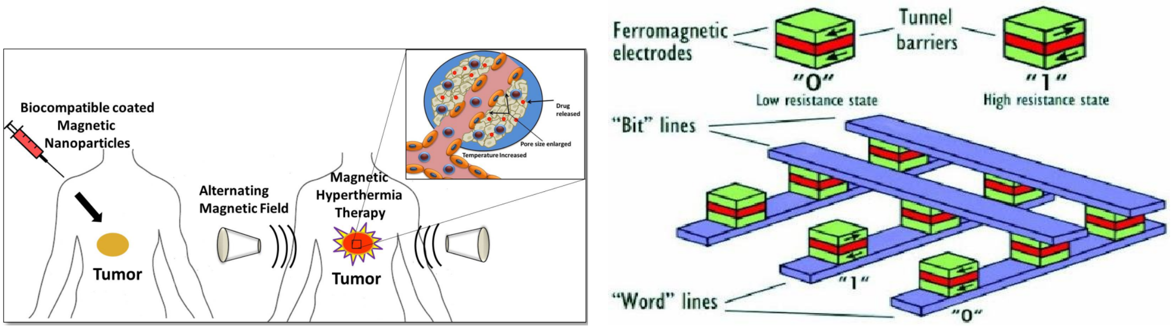

(a) Magnetic hyperthermia therapy. Reprinted from Moradiya et al. (2019).[5]

(b) Magnetic random access memory. Reprinted from Jenkins et al. (2016).[11]

Figure 1.1—Two current applications of magnetic structures. (a) Magnetic hyperthemia therapy has been used as a novel tool to treat cancer cells; (b) MRAM or Magnetic Random Access Memory is a type of non-volatile memory which stores data in magnetic domains, which will eventually become the dominant RAM method for memory storage.

Despite being applied in several areas, some aspects of magnetic nanostructures are not totally understood, and throughout the last years a lot of attention has been paid to study them. However, several topics remain unresolved, and some of the most important we can mention are: a) the mechanism of formation of magnetic domains in thin films[12, 13] and b) the theory of magnetization reversal physical process[14] of self-assembled magnetic nanostructures on top of metallic substrate and their related magnetic behavior.

In this context, stepped or vicinal surfaces have been used as a laboratory to study physical effects in low dimensionality systems.[15–19] Generally, these studies are concerned with the structural and magnetic properties of the substrate itself or with the thin films deposited there. The first studies involving vicinal surfaces took place in the 1960s, aiming to explain the diffraction pattern of surfaces with periodic and regular steps. In this context, one of the first and most important works has been carried out by Park and Farnsworth (1964)[20] which studied, by means of LEED experiments, the structure of clean nickel crystal surfaces with periodic steps and their influence on spots intensities both at the (110) and (111) planes. Schwoebel and Shipsey (1966)[21] studied the diffusion of atoms on crystalline surfaces with stepped regularity. Their work presented the growth mode theory of the adsorbed atoms amid a strong theoretical approach concerning atom movement probability on different steps and terraces. The theoretical approach of growth on stepped surfaces covered in this work was very import, and has influenced others fundamental studies, such as of Ellis and Schwoebel (1968)[22] and Lang et al. (1972).[23] Ellis and Schwoebel (1968) presented a detailed study of UO_2 single crystals both on flat and vicinal surface, showing a modern and systematic way to build stepped surface from flat crystals and presented optimal preparation methods to reach a well ordered vicinal surface. Besides that, presented a theoretical study concerning the vicinal surface model and its relationship with the spots intensities on electron diffraction patterns. Lang et al. (1972) established a new notation to designate the different kind of vicinal surfaces. This notation takes in account the number of atoms and of crystalline planes both on the terraces and on the steps. Furthermore, their work show the connection with the Miller's index, accordingly to the crystalline symmetries.

With the improvement of experimental techniques, a large number of vicinal surfaces has been investigated since 1990s, both from the structural and magnetic point of view. Some of the fundamental studies on the structure of stepped surface were carried out by Barreteau et al. (2003),[24] Rahman et al. (2003)[25] and Néel et al. (2003).[26] Barreteau et al. (2003) presented a detailed investigation regarding the electronic structure, geometry and the stability of vicinal surfaces using tight binding calculations and density functional theory (DFT). Rahman et al. (2003) have contributed to a better understanding of the thermodynamics parameters of vicinal surface, through a theoretical approach, with calculations of vibrational dynamics and vibrational free energy. Furthermore, they presented calculations of fundamental structural parameters (miscut angle, interatomic distance, terrace width and step height) of the main vicinal surfaces. Another important structural study was performed by Néel et al. (2003). Besides an overview on the current knowledge of stepped surfaces, this work presented a strong investigation of spontaneous pattern formation (self-organization) during homoepitaxial growth. Accordingly to this work, the thin film self-organization is defined by adatom diffusion and its optimal place to settle (lower energy), as well as to the so-called Erlich-Schwoebel barrier between two successive terraces. It has been shown, using theoretical approach and STM/HAS experiments, that the nanostructure formation and its stability on vicinal surfaces depends on several parameters, such as the growth rate, substrate temperature, width of the terraces and height of the steps.

The magnetism of thin films deposited on vicinal surfaces has been the goal of several studies aiming technological applications and previous studies have contributed to the understanding of low-dimensional magnetism. Shen et al. (1997)[27] studying the morphology and magnetism of Fe ultrathin films on vicinal Cu(111) have discovered the formation of self-assembled nanostrips, aligned with the steps. Analysing the hysteresis loops of these structures, they have observed that ferromagnetic behavior occurs even at submonolayer regime and that the magnetization curves depend on the temperature and time of deposition. Zhao et al. (2002)[28] using Monte Carlo simulation within a two-dimensional XY model, studied ferromagnetic thin films deposited on vicinal surfaces. Analysing theoretical hysteresis of these nanostructures, they have concluded that there is a strong uniaxial anisotropy due to the symmetry breaking produced by the stepped surface. Furthermore, they realized that the coercivity increases with the steps densities, but it has a complex relation with the film thickness. Repetto et al. (2006)[29] using experimental techniques - STM, LEED, MOKE and XMCD - studied Fe ultrathin films on Pt(111) and Pt(997). Both systems presented Spin Reorientation Transition (from perpendicular to in-plane) at the critical thickness, θ_{crit}, of 2.8ML and 3.3ML, respectively, however, the anisotropy due to the steps produced another Spin Reorientation Transition at submonolayer regime, $\theta_{crit} < 0.5$ML, evidencing the symmetry breaking of the surface.

In special, some attention has been paid to Fe, Co ferromagnetic nanostructures deposited either on Ag(100) or Ag(111) flat surfaces.[30–40] However, by reviewing previous work we have noticed a lack of studies using commonly substrates, among them silver vicinal surface. Therefore, the proposal of this work is to study the ferromagnetic structures deposited on a stepped silver surfaces, aiming to understand the influence of the substrate temperature during the epitaxial growth on the structural and magnetic properties of ferromagnetic ultrathin films. For that, we chose iron (Fe) and cobalt (Co) as magnetic material and silver Ag(977) as substrate. A large number of studies on Ag vicinal surfaces were done in the last ten years[41–47] however studies were not carried out neither in clean Ag(977) or having ferromagnetic overlayers on it. Furthermore, this work might provide a better understanding of interaction of thin film with a vicinal surface. The structural characterization of our samples was made with STM and LEED techniques, and for magnetic investigation we applied MOKE magnetometry, nevertheless, these details will be presented later in the text.

The dissertation is divided as follow: **Chapter 2** is dedicated to describe the crystalline structure both of flat and vicinal crystals and provides an overview of the most common magnetic interactions and its effects in others structures; **Chapter 3**, the experimental techniques are described and explained in details; **Chapter 4**, the experimental results are presented, at both systems Fe/Ag(977) and Co/Ag(977) concerning the structural and magnetic properties; **Chapter 5** is dedicated to analysis and physical interpretations of the experimental results; **Chapter 6** presents the summary of this work, indicating the main experimental conclusions and insights to future work.

Chapter 2

Magnetism and matter

The interaction between any solid object and the neighborhood occurs through the surface and interface. In solid state physics, an interface is the boundary between two regions occupied by different materials, however, the interface between matter and vacuum is called surface and studied in surface science. In general, solid objects are organized into periodic internal (bulk) and external (surface) layers. Although the most commonly investigated surfaces are atomically flat, in this work, we used a different kind of surface, called stepped (or vicinal) surface, whose details will be explained further.

If matter is deposited (by any method) on a surface, covering it with thicknesses in a sub-nanometer range to tens of micrometers, it is called a thin film. These structures are important for the industry due to their large applicability in several devices. Commonly these applications explore some physical effect based on the interaction between the surface (or the thin film presented there) and an optical or magnetic source. In this work, we used the vicinal surface Ag(977) and deposited Fe, Co ultra-thin films to study the structural arrangement and its connection with the magnetization dynamics. Therefore, this chapter presents a brief review of the crystalline structure and an overview of the main physical phenomena behind magnetism (and their interaction with the matter).

2.1 Crystalline structure

For a long time, the free electron model of Drude explained a large number of metallic properties of the matter. However, the use of classical statistic mechanics to predict some experimental results proved to be totally wrong. Sommerfeld tried to fix that by applying the Fermi-Dirac distribution to describe the conduction electrons, however some experimental observations remained without explanation, such as the transport coefficient of the free electron, static thermodynamics and fundamental mysteries (why some elements do not conduct?). This situation was modified by new assumptions about the electron motion. One of the most important assumptions was that electrons do not move in free space but in the presence of a static potential due to the arrangement of stationary ions. The fact is that, notably, the ions are not random distributed, but organized in a regular and periodic lattice, as confirmed by X-Ray and (later) by neutron diffraction, electronic microscopy and others experimental techniques. The fact of the atomic ordering forming the known crystalline lattices is the core of solid state physics and it is very important for the further discussion.

The crystalline structures are initially described by the Bravais (or real) lattices. The

Bravais lattice is an infinite arrangement of discrete points that repeat themselves (equally) throughout all the space. In other words, the position of each atom (or molecules, ions) in the crystal is given by

$$\mathbf{R} = n_1\,\mathbf{a}_1 + n_2\,\mathbf{a}_2 + n_3\,\mathbf{a}_3, \tag{2.1.1}$$

where n_1, n_2 and n_3 are integer values and $\mathbf{a}_1, \mathbf{a}_2$ and $\mathbf{a}_3$ are primitive vectors ($\mathbf{a}_1(\mathbf{x},\mathbf{y},\mathbf{z})$, $\mathbf{a}_2(\mathbf{x},\mathbf{y},\mathbf{z})$, $\mathbf{a}_3(\mathbf{x},\mathbf{y},\mathbf{z})$) related to the cartesian axis and lattice parameters. Commonly, the solids are ordered in several structures, the 14 Bravais lattices, that are grouped accordingly with their symmetries. Among them, there are 4 important structures, named Simple Cubic (SC), Body Centered Cubic (BCC), Face Centered Cubic (FCC) and Hexagonal Close Packed (HCP), see figure 2.1. For example, if the solid's geometry is simple cubic, the primitive vectors are $\mathbf{a}_1 = a\,\hat{\mathbf{x}}$, $\mathbf{a}_2 = a\,\hat{\mathbf{y}}$ and $\mathbf{a}_3 = a\,\hat{\mathbf{z}}$.

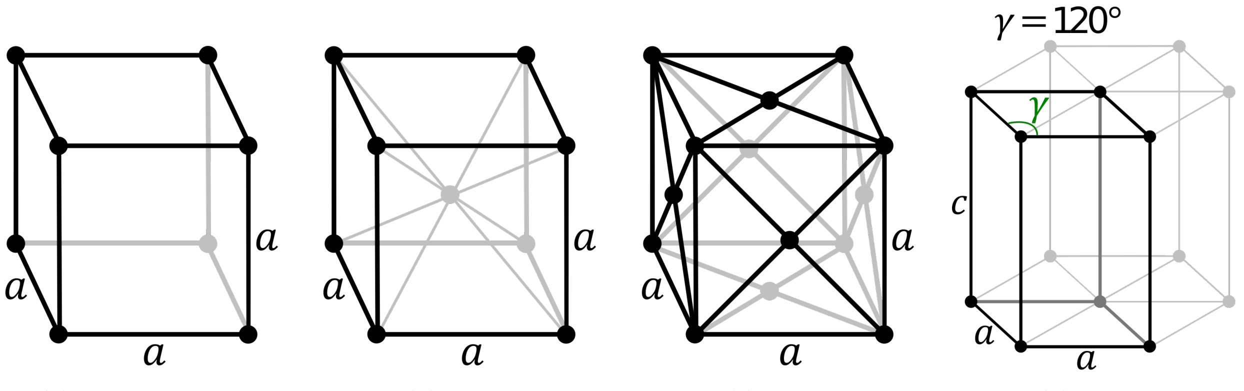

(a) Simple Cubic. (b) BCC. (c) FCC. (d) HCP.

Figure 2.1—Main Bravais lattices. (a) Simple Cubic; (b) Body Centered Cubic; (c) Face Centered Cubic; (d) Hexagonal. Reprinted from Daniel Mayer and Bob Mellish (2007).[48–50]

In this work, considering the substrate (Ag) used and the two deposited elements (Fe, Co), we have three different crystalline structures. Silver has a Face Centered Cubic structure with lattice parameter $a = 4.09$ Å; Iron is Body Centered Cubic, with $a = 2.87$ Å and the α-phase of cobalt is Hexagonal HCP, with $a = 2.51$ Å and $c = 4.07$ Å.[51] Cobalt has two stable phases, α (HCP) and β (FCC), however, the phase transition ($\alpha \rightarrow \beta$) occurs above 800 K.[52] Therefore, we assume that the deposited Co-films are HCP, even though we are aware that in the ultra-thin regime, a different stacking or even a stacking fault, may occur.

The identification of the crystalline structure of a solid can be carried out by electron diffraction or X-ray diffraction experiments. The theoretical interpretation of the x-ray reflection of parallel planes of atoms that constructively interfere, is that the difference of the incident wave vector $\vec{k}$ and the scattered wave vector $\vec{k}'$ must be equal to one of the reciprocal lattice vectors $\mathbf{K}$. The relation between $\mathbf{K}$ and the real Bravais lattice $\mathbf{R}$ is $e^{i\mathbf{K}\cdot\mathbf{R}} = 1$ and, for that, $\mathbf{K}$ can be written as

$$\mathbf{K} = h\,\mathbf{b}_1 + k\,\mathbf{b}_2 + l\,\mathbf{b}_3, \tag{2.1.2}$$

where $\mathbf{b}_1 = \frac{2\pi}{V}\mathbf{a}_2 \times \mathbf{a}_3$, $\mathbf{b}_2 = \frac{2\pi}{V}\mathbf{a}_3 \times \mathbf{a}_1$, $\mathbf{b}_3 = \frac{2\pi}{V}\mathbf{a}_1 \times \mathbf{a}_2$ and $V = \mathbf{a}_1 \cdot (\mathbf{a}_2 \times \mathbf{a}_3)$. h, k and l are integers named Miller Indices and the set (hkl) denotes a crystalline plane in Bravais lattice, as shown in figure 2.2. $\{hkl\}$ represent all the equivalents plane families of (hkl), $[hkl]$ represent the normal direction of the plane (hkl) and $< hkl >$ denotes all the set of directions that are equivalent to $[hkl]$ by symmetry.

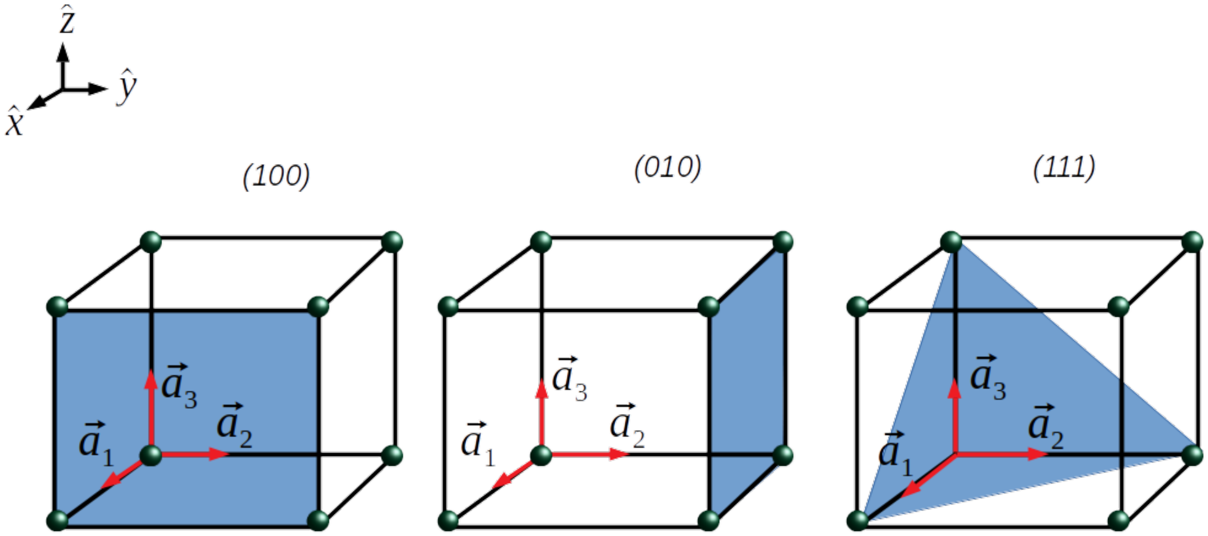

Figure 2.2—Three common crystalline planes in a Simple Cubic geometry. Online color.

An important concept in solid state physics is of the Brillouin Zone, which is defined as the Wigner-Seitz cell in the reciprocal lattice. The first Brillouin zone is defined as the smallest volume enclosed by planes that are the perpendicular bisectors of the reciprocal lattice vectors that are drawn from origin. The importance of the Brillouin zone stems from the description of waves in a periodic medium given by Bloch's theorem, whose consequences led to an understanding of the electronic band structures of solids, opening space to a large number of new discoveries.

2.1.1 Stepped surfaces

A special class of solid is formed by a bulk and a faceted surface, named stepped surface. The stepped or vicinal surface is created cutting a flat crystal in a determined direction $[hkl]$ making a θ angle (miscut angle) with a chosen crystallographic plane (hkl). This surface has two main crystallographic planes: the plane that follows the flat crystal (terrace) and the faceted plane (step). The structural stability of vicinal surfaces has been studied since the 90s and the experimental results have shown that these structures have a structurally stable phase which depends on the temperature. Theoretical arguments pointed that the unstable transitions occurs at relatively low temperatures, driven by the high vibrational entropy of steps.[53] From other point of view, the remarkable stability of such surfaces may be due to a repulsive inter-step interaction energy, making it difficult for the crystal to develop a equilibrium shape (flat).[23,53,54]

Differently from flat crystals, the vicinal surfaces have a classification that takes in account the terrace and step planes. Lang et al. (1972)[23] proposed a notation to classify these surfaces using the number of atoms both on terrace and at the step as

$$N_{terrace}(h_1k_1l_1) \times N_{step}(h_2k_2l_2), \tag{2.1.3}$$

where $N_{terrace}, N_{step}$ are the number of atoms at the terrace and at the step, respectively, while $(h_1k_1l_1)$ and $(h_2k_2l_2)$ are the crystalline planes of the terrace and step, respectively. This notation can be rewritten as function of the crystallographic Miller planes and its equivalence is shown in tables 2.1 and 2.2

Table 2.1: Equivalence between the notatations of Lang et al. and Miller for FCC structures. Adapted from Barreteau et al. (2003).[24]

Lang et al. notation	Miller notation
$N_{terrace}(111) \times N_{step}(100)$	$(N_{terrace}+1, N_{terrace}-1, N_{terrace}-1)$
$N_{terrace}(111) \times N_{step}(\bar{1}11)$	$(N_{terrace}-2, N_{terrace}, N_{terrace})$
$N_{terrace}(100) \times N_{step}(111)$	$(1, 1, 2N_{terrace}-1)$
$N_{terrace}(100) \times N_{step}(010)$	$(0, 1, N_{terrace}-1)$

Table 2.2: Structural parameters of the most common FCC vicinal surfaces. ΔH represent the height between two terraces and ω their width, both in units of lattice constant. Adapted from Rahman et al. (2003).[25] * Data extracted from Hahn et al. (1993),[55] Garbouj et al. (2009)[56] and Ayieta et al. (2010).[57]

Miller notation	Lang et al. notation	Miscut angle	ΔH	ω
(hkl)	$N_{terrace}(h_1k_1l_1) \times N_{step}(h_2k_2l_2)$	(degree)	(a)	(a)
(210)	2(110) × 1(100)	26.56	0.4472	1.1180
(331)	3(111) × 1(111)	22.00	0.5677	1.5408
(211)	3(111) × 1(100)	19.50	0.5773	1.7319
(310)	3(100) × 1(110)	18.44	0.4743	1.5810
(511)	3(100) × 1(111)	15.80	0.6800	1.8368
(410)	4(100) × 1(110)	14.04	0.4849	2.0616
(320)	3(110) × 1(100)	11.30	0.6933	1.8026
(551)	3(110) × 1(111)	8.05	0.9901	2.5247
(977)	8(111) × 1(100)	7.01	0.6078	4.7300
(997)*	8(111) × 1($\bar{1}$11)	6.50	0.5803	5.1636

In this work we have used a silver vicinal surface. This surface is based on flat silver Ag(111) and step plane (100). The terrace has 08 atoms while the height, 01 atom. Therefore, this vicinal surface is named Ag(977) and this notation was used in the whole work. By means of surface sensitive diffraction and imaging techniques (LEED and STM) we investigated the structural parameters of Ag(977) and the results are shown in figure 2.3. A large number of STM images of this surface has been recorded and the gaussian distributions of terrace width and height are shown in figure 2.3.e and 2.3.f, respectively. For that, we have used LEED optics from VG-Scientific (model RVL900) and STM from SPECS, model Aarhus 150. More details of the chamber and of these equipment's are explained in chapter 3. From the Gaussian fit, we determined that $\omega = (21.0 \pm 2.1)$ Å and $\Delta H = (2.3 \pm 0.3)$ Å, which are in good agreement with the values of the literature, $\omega = 19.35$ Å and $\Delta H = 2.48$ Å , Rahman et al. (2003).[25]

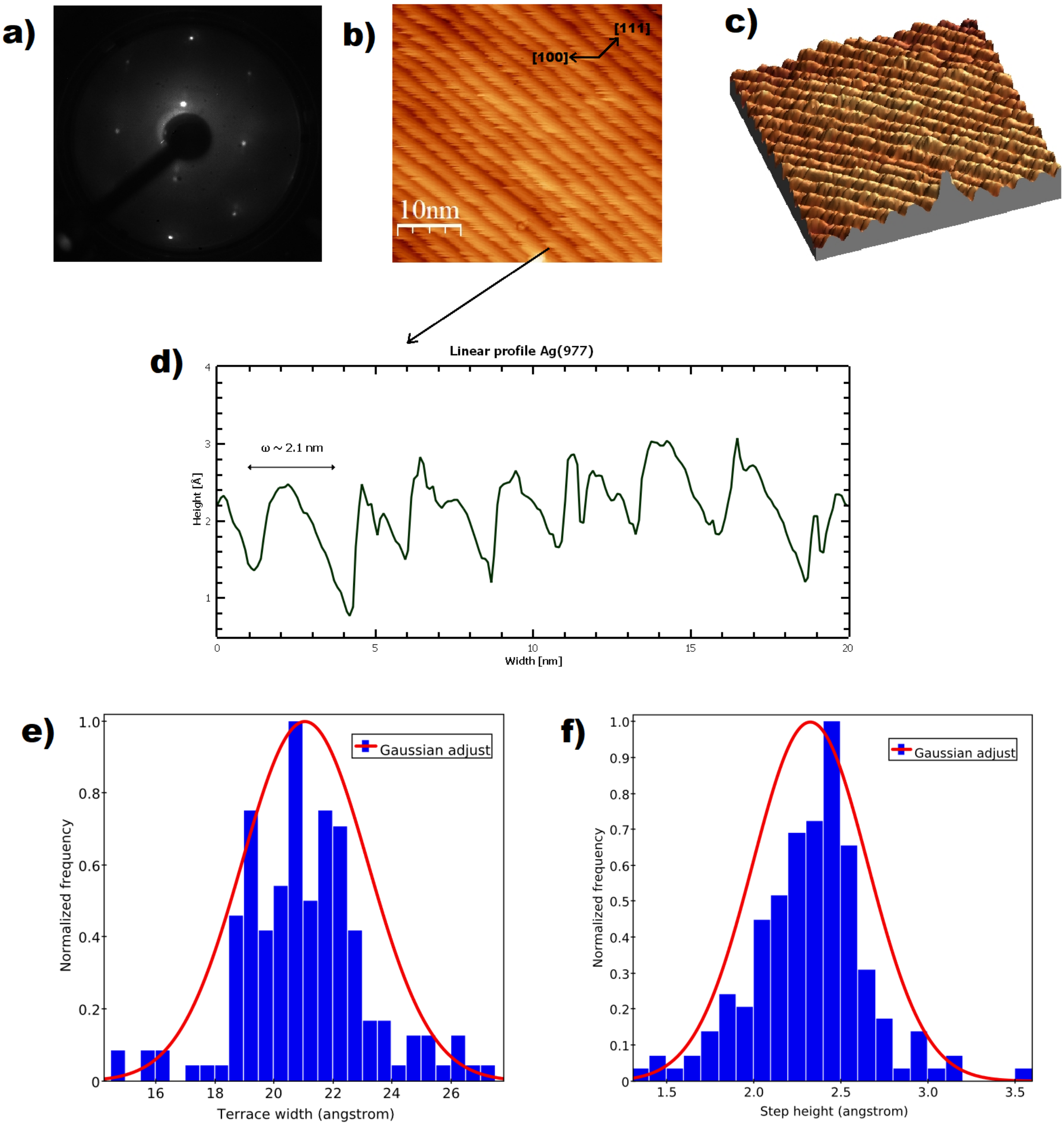

Figure 2.3—Experimental parameters of Ag(977). Here we present the experimental investigation of the vicinal surface Ag(977) by LEED (a) and STM (b)-(d). (b) represents the superficial STM image of Ag(977) and (c) is the 3D representation. (d) is a linear profile of their steps, (e) is the Gaussian fit that provided us the terrace width, and (f) the terrace height.

2.2 Self-assembled growth

In Surface and Interface Physics, the process of placing and adding atoms, ions or molecules on a substrate is called *growth*. In order to build systems with atomic level control (low-dimensional), the growth method known as *molecular beam epitaxy* (MBE) - usually performed in ultra-high vacuum environment - provides excellent deposition rate control and in many cases may result in an epitaxial growth mode. From Greek language, epitaxy means ‘on top’ plus ‘organized’, in other words, a kind of growth where the atoms or molecules are (somehow) ordered on top of a substrate. There are two types of epitaxy: homoepitaxy and heteroepitaxy. If the constituents (elements) of the epitaxially grown film are the same of the substrate, it’s called homoepitaxy. Otherwise, it is heteroepitaxy.

When material is deposited onto a flat surface, usually it forms a stable nuclei that can grow by capturing further atoms (or molecules) and this process is named nucleation. However, on the vicinal surfaces the growth process is nucleationless: it occurs superficial diffusion and the atoms deposited on this substrate move throughout the terrace, seeking for the spatial localization that requires less energy. Thermodynamics and kinetics plays a main role in this type of growth. Film deposition is understood within the thermodynamic approach (considering surface and interface energies) and the diffusion is a non-equilibrium kinetic process. Some details on this will be given in the next subsection.

2.2.1 Epitaxy on vicinal surfaces

When atoms arrive on vicinal surfaces several physical process take place. Among them, the most important ones are adsorption, superficial diffusion, desorption, island and step growth (see figure 2.4). However, the desorption effect is too small comparing with the other ones (for example, silver evaporates one atom every 10^{25} years at room temperature, Ibach (2006)[58] p. 556). So the physical effects that governs the epitaxial growth are the surface diffusion, islands formation and the atomic adsorption and their interaction with the substrate.

The diffusion of adatoms is the main process in surface growth. The atoms that reach the substrate have enough kinetic energy (mobility) to run a random walk throughout the terrace until they find an optimal place (lower binding energy) to settle down, often a lower terrace. Nevertheless, in case of a vicinal surface, they find a physical restriction caused by the stepped surface. This restriction is represented by a (reflective) energy barrier called Ehrlich-Schwöbel Barrier[59] which hinders the descent of atoms to the lower terrace, as illustrated in figure 2.4. When the atoms reach the edge, they suddenly have fewer neighbours compared to the middle of the terrace, resulting in a decrease binding energy, and resulting in an increase of diffusion over the edge. That decreases the atomic mobility and increases, therefore, the growth probability of a new layer on top of that terrace. These physical process produce a self-organized layer-by-layer growth controlled by flux rate, deposition time and substrate

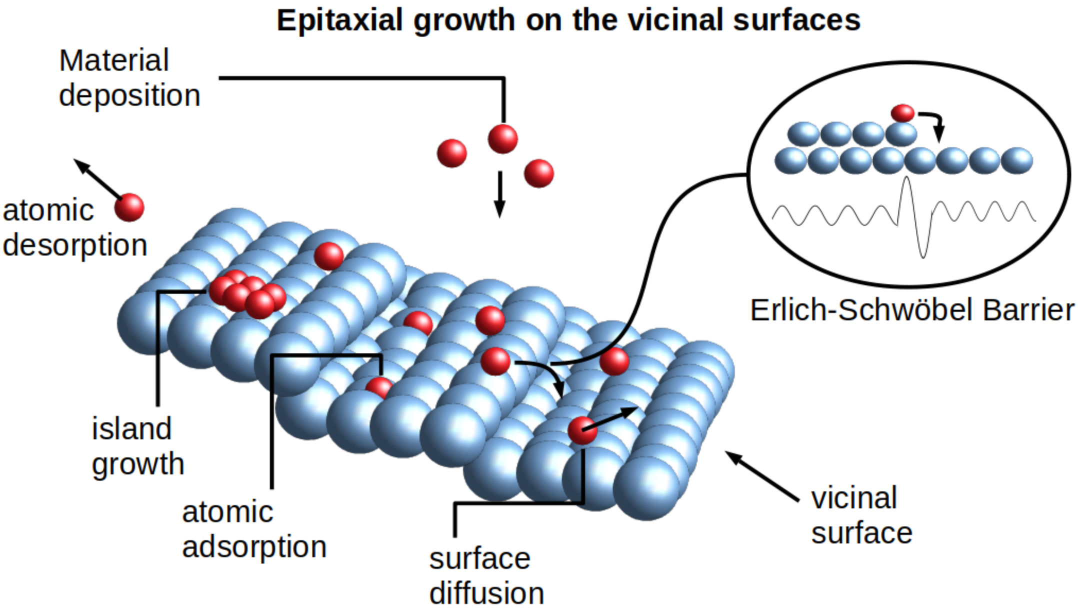

Figure 2.4—Main physical process on vicinal surface during epitaxial growth.

temperature.

The atomic diffusion starts with a random walk throughout the terrace. It can be described by the probability of atoms jump onto nearest sites with square symmetry. So, the probability to find the atom at site i after j jump is described by[58]

$$w_{ij} = \frac{w_1}{2}(w_{i+1,j-1}+w_{i-1,j-1})+\frac{w_2}{2}(w_{i+2,j-1}+w_{i-2,j-1})+\frac{w_3}{2}(w_{i+3,j-1}+w_{i-3,j-1})+\ldots \quad (2.2.4)$$

where the $w_1, w_2, w_3, \ldots$ represent the nearest neighbor distances. The transition from stochastic motion to diffusion continuum theory is made defining a coverage $\theta(x,y) = \Omega_S\rho(x,y)$, where $\rho(x,y)$ represents the density and Ω_S is the site area. Applying the continuum approach and mathematical development it's possible to establish the Fick's law of diffusion, represented by current density $\mathbf{J}(x,y)$ as follows

$$\mathbf{J}(x,y) = -D\nabla\rho(x,y), \quad (2.2.5)$$

where D represent the chemical diffusion coefficient. It postulates that the flux goes from regions of high concentration to regions of low concentration, with magnitude proportional to the gradient of the density. However, the Fick's law is a special form of a general transport equation that relates the random walk with the temperature, chemical diffusion, concentration and mobility, described as

$$\mathbf{J}(x,y) = -L_T\nabla\mu \quad (2.2.6)$$

with μ representing the chemical potential and L_T is a transport coefficient for diffusion on terraces. The calculation of L_T can be easily treated using the electrical analogy where each resistive element represents a random jump into the terrace. So, the mean jump rate $\langle\Gamma\rangle$ is proportional to $\left(\sum\limits_{i=1}^{N} 1/\Gamma_{i,i+1}\right)^{-1}$ with $\Gamma_{i,i+1}$ representing the jump rate from site i to $i+1$. After some physical assumptions outside from the scope of this work (further discussion can be found in Ibach 2006[58]) it is possible to establish that the mean jump rate is related to the physical effects taking place on the vicinal surface as follows

$$\langle\Gamma\rangle = f(E_A, E_D, E_{ES}, C_S, \nu_S, \nu_T, T), \tag{2.2.7}$$

where E_A represent the atom-terrace binding energy, E_D is the diffusion energy, E_{ES} is the wall (barrier) energy related to Erlich-Schwöbel Barrier, C_S is the step concentration, ν_S is the prefactor for jumping over the step edge, ν_T is the prefactor for terrace diffusion and T is the substrate temperature. Thereby, L_T is represented by

$$L_T = \frac{l^2 \langle\Gamma\rangle}{\Omega_S k_B T}, \tag{2.2.8}$$

l is the distance between one site and the next. Finally, the mass transport equation to atomic diffusion throughout a vicinal surface is given by

$$\mathbf{J} = -\frac{l^2 \langle\Gamma\rangle}{\Omega_S k_B T} \nabla\mu. \tag{2.2.9}$$

In case of atomic diffusion through a homogeneous substrate, the calculations mentioned above, connect it with the Mean Field Theory to describe the maximum cluster density (n_c) in a superficial area[60]

$$n_c = \eta(D_0/F)^{-1/3} exp(E_D/3k_B T) \tag{2.2.10}$$

where E_D is the diffusion energy, D_0 is the diffusion prefactor, F is the deposition rate and η is a prefactor related to atomic capture numbers. Thereby, it is possible to perform computational simulations in order to estimate the maximum cluster density for epitaxial growth on vicinal surfaces, comparing them with STM experiments. And this connection with the stochastic movement and the mass transport proposes an important tool to study the physical effects of an epitaxial process.

2.3 Magnetic interactions

Since the beginning of humanity, several magnetic effects have been known and observed, but not quite well understood. But this situation started to change in the last two centuries with the improvement of experimental methods and with the development of classical electromagnetic theory (Maxwell Equations/1865). However, it was only in the 20th century - with the advent of quantum theory - that the understanding on the magnetism of matter and of the magnetic interactions advanced in a way never seen before. The influence of chemical composition and of crystallographic structure on the magnetic properties of materials, the magnetic interactions with radiation (including light), dimension effects (e.g. magnetic anisotropy, superparamagnetic limit), surface effects (2D magnetism), all that new knowledge, has allowed mankind to develop a large number of new technologies. This section is devoted to show an overview of main magnetic phenomena in material physics, focusing on collective behavior and on magneto-optical effects.

2.3.1 Review of main magnetic phenomena

The intensity and direction of magnetic field is represented by the $\mathbf{H}$ vector, in the International System of Units (SI) its dimension is ampere per meter (A/m). The infinitesimal magnetic flux $d\Phi_B$ crossing a surface dS is $d\Phi_B = \mathbf{B} \cdot d\mathbf{S}$, where $\mathbf{B}$ is called vector magnetic flux density, whose unit in the SI base is $Tesla$ (T). If the magnetic source is in vacuum, there exists a linear dependence between the magnetic field and the flux density, $\mathbf{B} = \mu_0\mathbf{H}$, where μ_0 is the magnetic permeability of free space. If instead of free space there exists a continuous medium the material behavior is expressed in terms of magnetization $\mathbf{M}$ and the previous relation is changed to $\mathbf{B} = \mu_0(\mathbf{H} + \mathbf{M})$. The magnetization is understood as an internal collective arrangement caused by the interaction between the external field and the magnetic moments of atomic spins. Microscopically $\mathbf{M}$ is calculated in terms of the individual magnetic moments ($\mathbf{m_i}$) as $\mathbf{M} \propto 1/V \sum \langle \mathbf{m_i} \rangle$, where V is the volume. From quantum physics, each individual magnetic moment is described as

$$\langle \mathbf{m_i} \rangle = -\frac{\mu_B}{\hbar}[2\langle \mathbf{s_i} \rangle + \langle \mathbf{l_i} \rangle], \tag{2.3.11}$$

where $\langle \mathbf{s_i} \rangle$ and $\langle \mathbf{l_i} \rangle$ are the expected values of spin moment and angular moment respectively of each atom. In most cases, the magnetization of a material is directly related to the applied field as $\mathbf{M} = \chi\mathbf{H}$, where χ is the magnetic susceptibility. If the internal magnetism produces an isotropic response - magnetization vector is aligned and scales equally to applied field in all three directions - χ is a scalar constant. Otherwise, if the magnetization depends of the applied field direction then χ becomes a tensorial variable.

The magnetic susceptibility of an isotropic media assumes different values according to the internal behavior upon application of a magnetic field $\mathbf{H}$. If the material is diamagnetic,

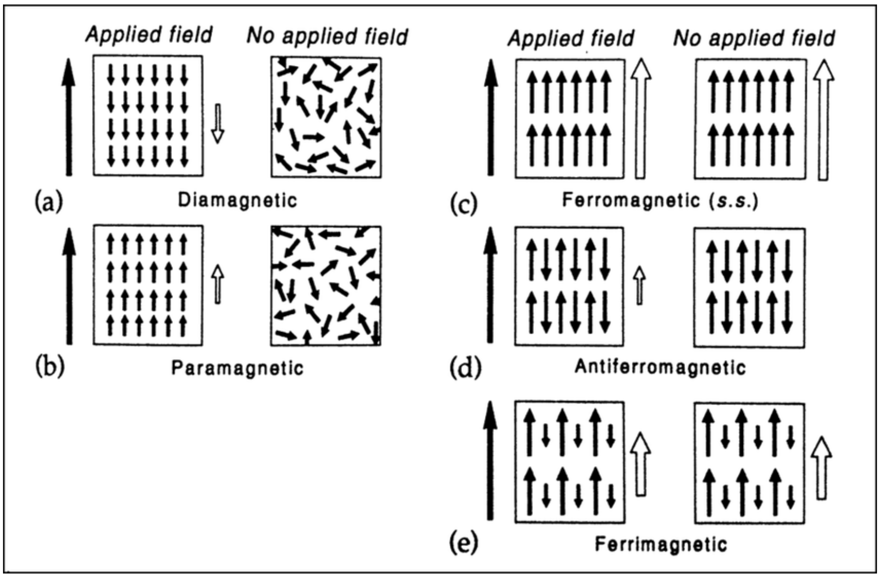

Figure 2.5—Magnetic behavior of main materials under influence of the external applied field. Extracted from Ives (2016).[61]

then χ = *constant* < 0. In this configuration, with no applied field, the atomic spins are randomly aligned without a preferential direction. When an external magnetic field is applied, they align in the opposite direction relative to **H** (due to Lenz's rule) and the total magnetization is -$|\mathbf{M}|\hat{e}_H$ as shown in figure 2.5a. Diamagnetism is present in all materials but it is only relevant in the absence of other collective phenomena (weaker than other collective magnetic phenomena). Some materials are notably diamagnetic such as organic substances, superconductors below the critical temperature and some metals like silver (Ag) and mercury (Hg). In **paramagnetism** the susceptibility is positive and temperature dependent, i.e., $\chi = \chi(T) > 0$. With no applied field the atomic spins point to random directions and align parallel to an external applied field as shown in figure 2.5b. The presence of paramagnetism is due to permanent magnetic moments that align with **H**. They can be classified as localized or itinerant moments: the first one is caused by electrons of an inner shell which is only partially filled and it is called Langevin paramagnetism, with $\chi^{Langevin}(T) = cT^{-1}$, c is a constant. In contrast, itinerant moments are due to free electrons in the valence band which carry out a permanent moment of 1 μ_B, that is the so called Pauli paramagnetism and χ is nearly temperature independent, with $\chi^{Pauli} << \chi^{Langevin}$.

One of the most important magnetic behavior is **ferromagnetism**. In this case χ presents a complex dependence with temperature, applied field and its history of the material, i.e. $\chi = \chi(T, \mathbf{H}, history)$. The magnetic state of a ferromagnetic material (e.g. Fe, Co and Ni) strongly depends on the history (or cycle) of the applied field, as well as on the temperature. Even in absence of **H**, small magnetic domains (of a ferromagnetic material) may point towards a certain direction, this is known as spontaneous magnetization (see figure 2.5c). In the range $0 < T < T_c$ (Curie temperature) by applying a high enough magnetic field, all magnetic domains align towards the direction of $\mathbf{H}$, remaining in this state after removal of this field. Heating above the Curie temperature, the system is brought to a randomly disordered (paramagnetic) state and the material loses its previous magnetic order, and even if the material is cooled down to a temperature lower than T_c all the spins will remain randomly aligned without an external field. Close to ferromagnetism, there is **antiferromagnetism**. In this case, two sublattices (a and b) are formed with magnetizations (in absence of $\mathbf{H}$) $\mathbf{M}_a$ and $\mathbf{M}_b$, where $\mathbf{M}_a = -\mathbf{M}_b$ bellow Néel's temperature (T_N). Even by applying $\mathbf{H}$ it is not possible to flip the magnetic moments of single domains and the material remains without a preferential orientation (see figure 2.5d). Above T_N the system behaves such as a paramagnet. A special case of antiferromagnetism is the **ferrimagnetism**. In this situation, $\mathbf{M}_a \neq \mathbf{M}_b$. By applying a magnetic field, $\mathbf{M}_a$ and $\mathbf{M}_b$ align antiparallel to each other with the largest $\mathbf{M}$ (in modulus) orienting itself towards the $\mathbf{H}$ direction (see figure 2.5e). Just as in ferromagnetism, ferrimagnetic systems become paramagnetic above the Curie temperature.

Besides that, there is another important type of magnetic behavior called **superparamagnetism** or **superparamagnetic regime**. This phenomena appears in small ($\sim 3nm$) ferromagnetic or ferrimagnetic nanoparticles, and is also temperature dependent. Because of the nanoparticle's magnetic anisotropy (that will be explain further) there is a stable orientation, however it has a finite probability for the magnetization to flip and reverse its direction under the influence of temperature. The time between two flips is called Néel relaxation time. In the absence of external field, when the measurement's time is longer than the Néel relaxation time, the magnetization appears to be equal (in average) to zero - superparamagnetic state. Thus, an external magnetic field is able to magnetize these particles, such as a paramagnet, but, in that case, the magnetic susceptibility of a superparamagnetic particle is much larger than in the case of paramagnetism. Superparamagnetic behavior can also be observed in ultra-thin films at room temperature.[62,63]

2.3.2 Ferromagnetism in thin films

Ferromagnetism is a collective phenomenon determined by the interaction of the external magnetic field and the internal domains of the material. The relation between the applied magnetic field $\mathbf{H}$ and the sample magnetization $\mathbf{M}$ is observed through the hysteresis loop, as shown in figure 2.6. A ferromagnetic sample initially with a net magnetization equal to zero (unmagnetized) is submitted to $\mathbf{H}$. Increasing the applied field the magnetization increases up to the saturation magnetization $\mathbf{M}_s$ at higher fields. The magnetic field that saturates the magnetization is called saturation field $\mathbf{H}_s$. Decreasing $\mathbf{H}$ to zero, the system is brought to a remnant magnetization $\mathbf{M}_r$. Applying an increasing magnetic field in the opposite direction, the magnetization decreases and reaches a zero value at the field $\mathbf{H}_c$, known as the coercive field. As one continues to increase $\mathbf{H}$ in the opposite direction, the system reaches again a (negative) saturation magnetization. By increasing positively the field the cycle is closed, forming the hysteresis loop.

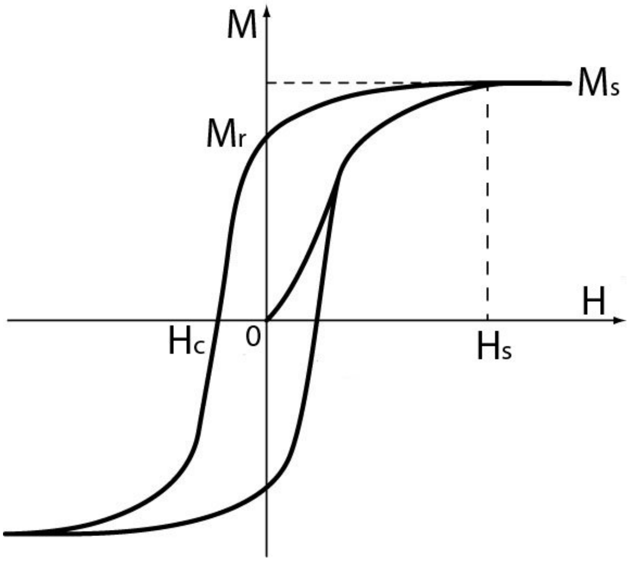

Figure 2.6—Hysteresis loop of ferromagnetic materials, showing the applied field **H**, the total magnetization **M**, the saturation magnetization $\mathbf{M}_s$, the remanent magnetization $\mathbf{M}_r$ and the coercive field $\mathbf{H}_c$. Extracted from Arora (2018).[64]

Classical physics is unable to explain any form of magnetic phenomenon, so that magnetism of matter remains in the quantum mechanics theory. From the magnetic point of view, the atoms are described by the magnetic dipoles originating from both orbital and spin momentum, The total angular momentum **J** of the atom is composed by the orbital angular **L** and the spin **S** momenta: $\mathbf{J} = \mathbf{L} + \mathbf{S}$. The magnetic dipole momentum modulus is proportional to total angular momentum, i.e., $|\vec{\mu}| = \gamma|\mathbf{J}|$, where $\gamma = e/(2m_e)$ is the gyromagnetic ratio. By employing the Schrödinger formalism we have that

$$\hat{\mathbf{J}}^2\Psi = \hbar^2 j(j+1)\Psi \;\; \rightarrow \;\; |\mathbf{J}| = \hbar\sqrt{j(j+1)} \;\; \rightarrow \;\; |\vec{\mu}| = \mu_B\sqrt{j(j+1)}, \tag{2.3.12}$$

where $\mu_B = e\hbar/(2m_e)$ is called Bohr Magneton. When magnetic dipoles interact with each other, they orient themselves in particular arrangements that minimize the total energy of the material. As electrons are fermions, their wavefunctions Ψ are antisymmetric (because of the Pauli's exclusion principle) and in the special case of ferromagnetism, the overlapping of Ψ forces the electronic spin to align parallel (exchange interaction). This situation is described by the hamiltonian of the system with two electrons, i.e.

$$\hat{\mathcal{H}} = \hat{\mathcal{H}}_1 + \hat{\mathcal{H}}_2 + \hat{\mathcal{H}}_{ex}, \tag{2.3.13}$$

where $\hat{\mathcal{H}}_{1,2}$ represents the hamiltonian of the electron 1 and 2. $\hat{\mathcal{H}}_{ex}$ is the exchange interaction hamiltonian (Heisenberg Hamiltonian). It provides a pairwise coupling between adjacent spins,

$$\hat{\mathcal{H}}_{ex} = -2J_{ex}\,\hat{\mathcal{S}}_1\,\hat{\mathcal{S}}_2 \tag{2.3.14}$$

where J_{ex} is called overlap integral, which takes in account the proximity of the two electrons. The exchange interaction is very strong but decreases (exponentially) with distance being strong enough to spontaneously order neighboring magnetic dipoles at room temperature. When an external magnetic field is applied, the total Hamiltonian is changed to

$$\hat{\mathcal{H}} = \hat{\mathcal{H}}_1 + \hat{\mathcal{H}}_2 + \hat{\mathcal{H}}_{ex} + \hat{\mathcal{H}}_{1,\mathbf{H}} + \hat{\mathcal{H}}_{2,\mathbf{H}}, \tag{2.3.15}$$

with $\hat{\mathcal{H}}_{1,2,\mathbf{H}}$ representing the interaction of each electron with the external field $\mathbf{H}$. The interaction energy between the magnetic field and the magnetic dipole is given by $E = \vec{\mu} \cdot \mathbf{H}$, such that the total hamiltonian becomes

$$\hat{\mathcal{H}} = \hat{\mathcal{H}}_1 + \hat{\mathcal{H}}_2 - 2J_{ex}\hat{S}_1\,\hat{S}_2 + \vec{\mu}_1 \cdot \mathbf{H} + \vec{\mu}_2 \cdot \mathbf{H} = \hat{\mathcal{H}}_1 + \hat{\mathcal{H}}_2 + \hat{\mathcal{H}}_{magnetic}. \tag{2.3.16}$$

The magnetic dipoles $\vec{\mu}_{1,2}$ can be written as $\vec{\mu}_{1,2} = \mu_B \mathbf{S}_{1,2}/\hbar$, and then the part of the hamiltonian associated solely to magnetic interactions can be isolated,

$$\mathcal{H}_{magnetic} = -J_{12}\mathbf{S}_1\,\mathbf{S}_2 + \frac{\mu_B}{\hbar}\mathbf{H} \cdot \mathbf{S}_1 + \frac{\mu_B}{\hbar}\mathbf{H} \cdot \mathbf{S}_2, \tag{2.3.17}$$

where $J_{12} = 2J_{ex}$ represents the overlap between two electrons.

For magnetic field applied to a large collection of magnetic dipoles, the magnetic hamiltonian assumes the form

$$\mathcal{H}_{magnetic} = -\sum_{i,j} J_{ij}\mathbf{S}_i \cdot \mathbf{S}_j + \frac{\mu_B}{\hbar}\sum_i \mathbf{S}_i \cdot \mathbf{H} = \sum_i \left[-J_{ij}\mathbf{S}_j + \frac{\mu_B}{\hbar}\mathbf{H}\right] \cdot \mathbf{S}_i. \tag{2.3.18}$$

The Weiss model proposes an approximation taking in account that the interaction of a magnetic ion with its neighbors is described using a specific kind of field, named exchange molecular field $\mathbf{B}_{mf} = \lambda \mathbf{M} = -\hbar \sum J_{ij}\mathbf{S}_j/\mu_B$, and λ being the molecular field constant. The total magnetic field can be represented as $\mathbf{B}_T = \mathbf{B}_{mf} + \mathbf{H}$. For that,

$$\mathcal{H}_{magnetic} = \frac{\mu_B}{\hbar}\sum_i [\mathbf{B}_{mf} + \mathbf{H}] \cdot \mathbf{S}_i = \frac{\mu_B}{\hbar}\sum_i \mathbf{B}_T \cdot \mathbf{S}_i. \tag{2.3.19}$$

On the other hand, the magnetization $\mathbf{M}$ of the sample can be calculated by using statistic mechanics. The magnetization $\mathbf{M}$ of a system is related to the partition function Z as

$$M = nk_BT\frac{\partial Z}{\partial B_T}, \tag{2.3.20}$$

where k_B, T and n are the Boltzmann constant, temperature and number of electrons, respectively. The partition function Z is related to total magnetic moment m_J, g_J factor, $\mathbf{B_T}$ and T as

$$Z = \sum_{m_J=-J}^{-J} e^{(m_J g_J \mu_B |\mathbf{B}_T|/k_B T)}, \tag{2.3.21}$$

and from these calculations (see more in Getzlaff 2008[65]) it is possible to describe the magnetization of the system as

$$\frac{M}{M_s} = \frac{1}{2J}\frac{1}{Z}\frac{\partial Z}{\partial(y/2J)} = \frac{2J+1}{2J} coth\left[\frac{2J+1}{2J}y\right] - \frac{1}{2J} coth\left[\frac{y}{2J}\right], \tag{2.3.22}$$

where M_s is the saturation magnetization and $y = g_J \mu_B J |\mathbf{B}_T|/(k_B T)$. The right side of the equation above is known as Brillouin function $B_J(y)$ (further details are presented in Appendix A) and then we can write

$$M = M_s B_J(y). \tag{2.3.23}$$

This theoretical relation can be used to explain the shape of hysteresis loop of ferromagnetic materials (see figure 2.6), accordingly to the experimental results. Moreover, here the influence of temperature is important to determinate the phase transition point, that is the temperature at which the ferromagnetic material changes its behavior to paramagnetic, called Curie Temperature T_C.

2.3.3 Magnetic anisotropies

As previously discussed (see subsection 2.3.2), the interaction between the external magnetic field and the ferromagnetic sample is represented by the hamiltonian of the system, composed by Heisenberg Hamiltonian and the energy term due to Zeeman interaction. The total hamiltonian is isotropic and the energy levels do not depend on the direction in space in which the crystal is magnetized. However, real magnetic materials may not be isotropic and this induces magnetic anisotropies in the materials. Mainly, there are five kind of anisotropies: I) magnetocrystalline anisotropy; II) shape anisotropy; III) induced magnetic anisotropy; IV) stress anisotropy and V) surface and interface anisotropy. The most relevant anisotropies are the magnetocrystalline and the shape one, which will be described bellow.

The **magnetocrystalline anisotropy** is caused by the spin-orbit interaction of the electrons, that are linked to crystalographic structure (coupling between the electron orbital motion and the crystal electric field). The interaction energy acts to align the magnetic moments parallel, whatever the chosen direction. The direction of this alignment depends on the spin interaction with structure, as it prefers to align itself along well-define crystallographic axes. The magnetization direction, $\mathbf{m} = \mathbf{M}/|\mathbf{M}| = (\alpha_1, \alpha_2, \alpha_3)$, is represented by the direction cosines in spherical coordinates,

$$\alpha_1 = sin\theta cos\phi, \quad \alpha_2 = sin\theta sin\phi \quad and \quad \alpha_3 = cos\theta, \tag{2.3.24}$$

with $\alpha_1^2 + \alpha_2^2 + \alpha_3^2 = 1$. The crystalline energy due to anisotropy can be expanded around the free energy equation ($F = F_0 + aM^2 + bM^4$), and there is no difference in energy between oppositely magnetized systems, $E(\mathbf{M}) = E(-\mathbf{M})$, so that

$$E_{crys} = E_0 + \sum_{ij} b_{ij}\alpha_i\alpha_j + \sum_{ijkl} b_{ijkl}\alpha_i\alpha_j\alpha_k\alpha_l. \tag{2.3.25}$$

For a cubic system, this energy can be expressed as

$$E_{crys}^{cubic} = K_0 + K_1(\alpha_1^2\alpha_2^2 + \alpha_1^2\alpha_3^2 + \alpha_2^2\alpha_3^2) + K_2\alpha_1^2\alpha_2^2\alpha_3^2 + ... \tag{2.3.26}$$

and

$$E_{(100)} = K_0, \quad E_{(110)} = K_0 + \frac{1}{4}K_1, \quad E_{(111)} = K_0 + \frac{1}{3}K_1 + \frac{1}{27}K_2, \tag{2.3.27}$$

where K_0, K_1 and K_2 represent the anisotropy constants and $E_{(100),(110),(111)}$ represent the anisotropy energies due to the crystallographic planes (hkl). These crystal anisotropy constants have remarkable importance in this study, because they depend on the material and on the temperature. Besides that the sign of those constants determine the easy magnetization axis, the direction in which it is easier to magnetize the system (with a lower applied field), as compared to other directions. Crystallographic directions in which it is necessary to apply high fields to magnetize the system are called hard axes, and that is caused by their larger magneto-crystalline energy. The easy axis of magnetization is the direction in which E_{crys} is smaller.

The **shape anisotropy** is another type of anisotropic effect. Polycrystalline samples with randomly oriented grains, and specially if the grains have spherical shape, they do not possess any magnetocrystalline anisotropy and then the magnetization points to a random direction. On the other hand, if a grain is not spherical then it has one (or more) specific direction that is easier to magnetize. In this case, the energy is

$$E_{shape} = \frac{1}{2}\int \mu\mathbf{M}\cdot\mathcal{N}\mathbf{M}\, dV, \tag{2.3.28}$$

where $\mathcal{N}$ is the demagnetizing tensor and μ is the magnetic permeability of the medium. An important result is reached if we consider the grain as a very thin film. In this case, the shape anisotropy energy is

$$E_{shape} = K_0 + K_{shape}\, sin^2\, \theta. \tag{2.3.29}$$

From the above equation it can be seen that for $\theta = 90^\circ$ (spherical coordinates - perpendicular to the thin film), E_{shape} reaches its minimum value, which means that the easy axis is in the film plane. The magnetocrystalline anisotropy constants K_1, K_2 are smaller than the shape anisotropy constant K_{shape}. For example, in bcc-Fe the constants are $K_1 = 5.48 \times 10^4\ J/m^3$

and $K_2 = 1.96 \times 10^2\ J/m^3$ while $K_{shape} = 1.92 \times 10^6\ J/m^3$, $K_{shape} > K_1 > K_2$ (these values depend on thickness of the thin film). For this reason, in general, the in-plane magnetization for thin films systems is dominant over the magnetocrystalline anisotropy.

2.3.4 Magneto-Optical Effects

An important magnetic phenomenon of paramount significance in this work, is the so-called magneto-optical effect - the modulation of optical state of light through of the interaction with magnetic material. Magneto-optical effects include the Faraday and Voigt (Cotton–Mouton) effects that alter the polarization of the transmitted light through the material. In contrast, the magneto-optic Kerr effect is related to the change of polarization state of the reflected light.

The **Faraday effect** was discovered in 1845 by Michael Faraday when he was studying the interaction of electromagnetic radiation with magnetic materials. He found out that when polarized light passes through a transparent material under an applied magnetic field the polarization angle rotates by β (see figure 2.7). From Faraday's observations the rotation angle is given by

$$\beta = \mathcal{V}Bd, \tag{2.3.30}$$

where $B = |\mathbf{B}|$ is the magnetic flux density, d is the material thickness crossed by light and $\mathcal{V}$ is named Verdet's constant. To explain this effect it is necessary to use the dispersion quantum theory, that treats the interaction at the atomic scale. Otherwise, for non-magnetic materials, the classical theory of light provides a good understanding of the Faraday effect.[66] It can be treated as circular birefringence (or optical activity) causing a difference in the refractive indices (Δn) between the two circular polarizations, which causes the polarization rotation. The right and left refraction indices (n_l, n_r) are affected by the Larmor frequency ν_L (precession rate of magnetic moment around external magnetic field), by the incident light frequency ν and the refractive index n of the material; $n_l = n(\nu - \nu_L)$ and $n_r = n(\nu + \nu_L)$. The phase change due to left and right rotation is $\phi_r = (n_r d/\lambda)/2\pi$ and $\phi_l = (n_l d/\lambda)/2\pi$, consequently $\beta = 1/2(\phi_l - \phi_r)$. For that, the Verdet constant can be represented by[67]

$$\mathcal{V} = \frac{e}{2m_e c}\lambda\frac{dn}{d\lambda}, \tag{2.3.31}$$

where e, m_e, c and λ are the electrical charge, electron mass, light velocity and light wavelength, respectively, and $dn/d\lambda$ is the change ratio of refraction index with the light wavelength.

Similarly to Faraday effect, in 1875 John Kerr observed the change in the refractive index of a material in response to an applied electric field, later named Kerr effect. On electro-optical Kerr effect, the electrical field provokes alteration of refraction index and the material behaves as birefrigent, with $\Delta n = \lambda K E^2$, where λ, K and E are the incident wavelength, Kerr constant and electrical field modulus, respectively. This promotes the

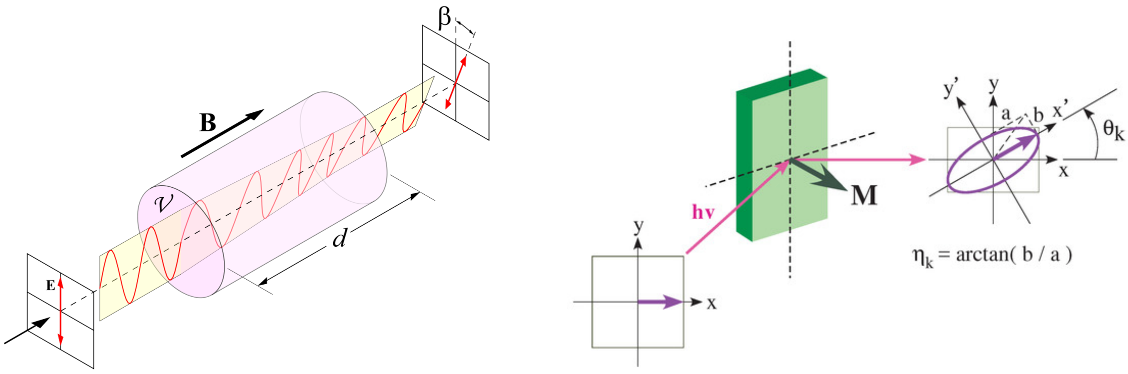

(a) Faraday effect.

(b) Magneto-optical Kerr Effect.

Figure 2.7—Magneto-optical effects: Faraday effect (a) and MOKE (b). The transmitted and reflected lights have their polarization angles rotated by β and θ_k, respectively. Reprinted from DrBob (2006)[68] and Yamamoto (2017).[69]

appearance of Optical Kerr effect, present on nonlinear optics. Meanwhile, the most import Kerr effect variant for this work is the **Magneto-Optical Kerr Effect**.[70] In this situation the polarization angle of the reflected light is rotated by θ due to the magnetization $\mathbf{M}$ present at the sample (see figure 2.7).The refraction index of the ultra-thin film is a complex number, therefore part of the incident light is absorbed. Thus, a linearly polarized light after reflection becomes elliptically polarized. From the classical point of view, this effect can be understood using the Maxwell Equations and their derivatives assumptions.

The interaction between light and matter is mediated by the electrical field $\mathbf{E}$ of the light and the electrical displacement $\mathbf{D}$ inside the material. From Maxwell equations we have $\nabla \cdot \mathbf{D} = \rho$, where $\rho = \rho_b + \rho_f$, with ρ_b and ρ_f representing the bound and free charge densities, respectively. The bound charge density is related to the response of the medium under an external influence as

$$\rho_b = -\nabla \cdot \mathbf{P}, \tag{2.3.32}$$

where $\mathbf{P}$ is the polarization. So, the electrical displacement can be rewritten as $\mathbf{D} = \epsilon_0 \mathbf{E} + \mathbf{P}$, with ϵ_0 representing the vacuum electrical permittivity. For the most common materials, there is a linear relation between the polarization and the electrical field. However, in case the polarization depends on the direction of the applied field, then $\mathbf{P} = \epsilon_0 \overleftrightarrow{\chi}_e \mathbf{E}$, where $\overleftrightarrow{\chi}_e$ is the electrical susceptibility tensor that depends on the magnetization $\mathbf{M}$. Thus, $\mathbf{D}$ is represented by

$$\mathbf{D} = \epsilon_0 \mathbf{E} + \mathbf{P} = \epsilon_0 \mathbf{E} + \epsilon_0 \overleftrightarrow{\chi}_e \mathbf{E} = \epsilon_0 \overleftrightarrow{\epsilon}_r \mathbf{E} = \overleftrightarrow{\epsilon} \mathbf{E}, \tag{2.3.33}$$

where $\overleftrightarrow{\epsilon}_r$ is the dielectric tensor, $\overleftrightarrow{\epsilon}_r = 1 + \overleftrightarrow{\chi}_e(\mathbf{M})$, and $\overleftrightarrow{\epsilon}$ is the medium permittivity, $\overleftrightarrow{\epsilon} = \epsilon_0[1 + \overleftrightarrow{\chi}_e(\mathbf{M})]$. Ultimately, the electrical permittivity tensor $\overleftrightarrow{\epsilon}$ depends on the magnetization. The magnetization provokes a splitting of the fundamental or excited state energy levels of the optical transitions.[71] Thus, we can write the electrical permittivity components as $\epsilon_{ij} = \epsilon^0_{ij} + \Delta\epsilon_{ij}(\mathbf{M})$, where the second (magnetization dependent) term $\Delta\epsilon_{ij}(\mathbf{M})$ is much smaller than ϵ^0_{ij}. So, using perturbation theory, this tensor can be expanded as[71–73]

$$\epsilon_{ij} = \epsilon^0_{ij} + \left[\frac{\partial \epsilon_{ij}}{\partial M_k}\right]_{\mathbf{M}=0} M_k + \frac{1}{2}\left[\frac{\partial^2 \epsilon_{ij}}{\partial M_k \partial M_l}\right]_{\mathbf{M}=0} M_k M_l + ... \tag{2.3.34}$$

$$\epsilon_{ij} = \epsilon^0_{ij} + K_{ijk}M_k + G_{ijkl}M_kM_l + ...$$

where K_{ijk} is called third rank linear magneto-optic tensor and G_{ijkl} is a tensor of fourth rank. Terms of order greater than 2 are very small and can be neglected. In addition, for a cubic symmetry crystal, $K_{123} = K_{231} = K_{312} = -K_{213} = -K_{321} = -K_{132} = K$ (Kerr constant) and all other K_{iii} are null. Finally, its possible rewrite equation (2.3.33) as

$$\mathbf{D} = \overset{\leftrightarrow}{\epsilon}{}^0 \mathbf{E} + K(\mathbf{M} \times \mathbf{E}), \tag{2.3.35}$$

with Tr $(\overset{\leftrightarrow}{\epsilon}{}^0) = 3\epsilon$. So, matricially the electrical displacement is

$$\mathbf{D} = \begin{pmatrix} \epsilon & 0 & 0 \\ 0 & \epsilon & 0 \\ 0 & 0 & \epsilon \end{pmatrix} \begin{bmatrix} E_x \\ E_y \\ E_z \end{bmatrix} + K \begin{pmatrix} 0 & -M_z & M_y \\ M_z & 0 & -M_x \\ -M_y & M_x & 0 \end{pmatrix} \begin{bmatrix} E_x \\ E_y \\ E_z \end{bmatrix} = \overset{\leftrightarrow}{\Phi}\mathbf{E}. \tag{2.3.36}$$

Using the Voigt constant (or magneto-optical constant) $Q = -iKM_S\epsilon$ with M_S representing the saturation magnetization, we have

$$\overset{\leftrightarrow}{\Phi} = \epsilon \begin{pmatrix} 1 & -im_zQ & im_yQ \\ im_zQ & 1 & -im_xQ \\ -im_yQ & im_xQ & 1 \end{pmatrix}, \tag{2.3.37}$$

where $m_{xyz} = M_{xyz}/M_S$. A polarized light can be written as $\mathbf{E} = E_0 sen\,\theta\,\hat{\mathbf{s}} + E_0 cos\,\theta\,\hat{\mathbf{p}}$, where $\hat{\mathbf{s}}$ and $\hat{\mathbf{p}}$ represent the perpendicular and parallel directions with respect to the incidence plane respectively and θ is the angle between polarization axis and the $\hat{\mathbf{p}}$ direction. The Kerr rotation θ_p and θ_s are related to Fresnel coefficients as

$$\theta_p = \theta'_p + i\theta''_p = \frac{r_{sp}}{r_{pp}} \quad and \quad \theta_s = \theta'_s + i\theta''_s = \frac{r_{ps}}{r_{ss}}, \tag{2.3.38}$$

where θ'_j, θ''_j are Kerr rotation and Kerr ellipticity for each polarization, respectivelly, while r_{ij} represent the Fresnell coefficients. Similarly, it is possible to describe the change on the amplitudes of the electric field components (E_p and E_s), again in terms of the Fresnel coefficients, as follows[74]

$$\begin{pmatrix} E_p^r \\ E_s^r \end{pmatrix} = \overset{\leftrightarrow}{S} \begin{pmatrix} E_p^i \\ E_s^i \end{pmatrix} = \begin{pmatrix} r_{pp} & r_{ps} \\ r_{sp} & r_{ss} \end{pmatrix} \begin{pmatrix} E_p^i \\ E_s^i \end{pmatrix}, \tag{2.3.39}$$

where (E_p^i, E_s^i) and (E_p^r, E_s^r) are the amplitudes of the incident and reflected waves, respectively. These Fresnel coefficients are related to the ratio of reflected and incident waves intensities. G. Gomes in his master thesis (2009)[75] calculated in details these coefficients

$$r_{ss} = \frac{\mu_2 n_1 cos\,\theta_1 - \mu_1 n_2 cos\,\theta_2}{\mu_2 n_1 cos\,\theta_1 + \mu_1 n_2 cos\,\theta_2}, \tag{2.3.40}$$

$$r_{pp} = \frac{\mu_1 n_2 cos\,\theta_1 - \mu_2 n_1 cos\,\theta_2}{\mu_1 n_2 cos\,\theta_1 + \mu_2 n_1 cos\,\theta_2} + \frac{2i\mu_1\mu_2 n_1 n_2 cos\,\theta_1 sin\,\theta_2 m_x Q}{\mu_1 n_2 cos\,\theta_1 + \mu_2 n_1 cos\,\theta_2}, \tag{2.3.41}$$

$$r_{ps} = -\frac{i\mu_1\mu_2 n_1 n_2 cos\,\theta_1 (m_y sin\,\theta_2 + m_z cos\,\theta_2) Q}{(\mu_1 n_2 cos\,\theta_1 + \mu_2 n_1 cos\,\theta_2)(\mu_2 n_1 cos\,\theta_1 + \mu_1 n_2 cos\,\theta_2) cos\,\theta_2}, \tag{2.3.42}$$

$$r_{sp} = \frac{i\mu_1\mu_2 n_1 n_2 cos\,\theta_1 (m_y sin\,\theta_2 - m_z cos\,\theta_2) Q}{(\mu_1 n_2 cos\,\theta_1 + \mu_2 n_1 cos\,\theta_2)(\mu_2 n_1 cos\,\theta_1 + \mu_1 n_2 cos\,\theta_2) cos\,\theta_2}, \tag{2.3.43}$$

where n_1 and n_2 are the media refractive indices, μ_1 and μ_2 are the media magnetic permeability, θ_1 and θ_2 are the incidence and refraction angles, respectively, m_x, m_y and m_z are the normalised magnetization projections, and $Q = Q' + iQ''$ is the complex magneto-optical constant. Experimentally it is possible to have access to the reflected intensity (often named Kerr signal) that is related to the these Fresnel coefficients, this will be explained in details in chapter 3 (Experimental Techniques).

Depending on the plane of incidence of the light beam and on the direction of the applied magnetic field, the Kerr effect (MOKE) can assume different configurations. If the magnetic field is applied in the film plane and the incidence plane is parallel to this magnetization direction then is called Longitudinal MOKE or, simply, L-MOKE, otherwise, if the incidence plane is perpendicular to magnetic field, it's called Transverse MOKE, or T-MOKE. If the magnetic field is applied perpendicularly to the film plane, then it is known as Polar MOKE, or P-MOKE. Measuring in different configurations, we can address the magnetization dynamics of ultrathin systems ($\sim$ 20 nm[75]) under external influences, such as temperature (T), chemical concentration (μ), etc, whose details will be present in the next chapter.

Chapter 3

Experimental techniques

In this work the experimental investigation of ultrathin films on vicinal surfaces was carried out in Ultra High Vacuum (UHV) environment. The preparation of well-ordered surfaces and interfaces with negligible contamination requires systems with pressure in the 10^{-10}mbar (10^{-8} N/m^2) range.[76] Such pressures are obtained by using stainless steel sealed UHV chambers, pumped by turbomolecular and ion pumps. At this pressure (10^{-10}mbar) the contamination of one monolayer from the residual gas - considering a sticking coefficient of one - has a deposition time of 3hrs, which is more than the time of typical measurements, justifying the use of this kind of environment.

Prior to experiments, all chambers of the UHV-system (see fig. 3.1) were baked out, which means they were warmed up to 410K (150C) - and maintained at this temperature for 3 days - in order to eliminate water and other contaminants from the inner walls. After that the system is cooled down to room temperature and the system achieves UHV-pressure after one or two days. The vicinal crystal mounted on a sample holder was inserted into the system through a load lock chamber. As substrate we have used the vicinal surface Ag(977), purchased from *Surface Preparation Laboratory* (Netherlands). It is fabricated by cutting the flat Ag(111) at an angle of 7.01^o from the(111) plane. This surface consists of (111) terraces containing eight $< 01\bar{1} >$ chains, and a (100) step face. Here, the ultrathin film depositions on Ag(977) and all the measurements were performed *in situ*.

Preparation of a well-ordered surface is obtained by cycles of sputtering and annealing procedures. The sputtering process is a cathodic bombardment of ionized argon (Ar$^+$) accelerated by high voltage and collimated by a magnetic field. Argon is let into the sputter gun through a controlled needle inlet valve, so that the argon pressure in the chamber achieves 1.8×10^{-6} mbar, while the acceleration voltage can be selected between 1.0 keV and 2.5 keV. The ion beam collides with the superficial atoms, transferring kinetic energy to break up their bound with the superficial crystalline lattice. This process destroys the first monolayers of the substrate, but also removes contaminants and an eventual film layer that previously has been grown on top of that surface.

Surface reconstruction is induced by annealing (heating) which increases the mobility of the atoms, bringing them to lower energy sites and ultimately flattening the surface. The heating of the sample occurs by electron beam - thermionic excited electrons from a tungsten filament are accelerated towards the back side of the sample holder. The best annealing recipe was: 30 minutes at 760 K (cycling with Ar-ion sputtering at 1keV) and after the last heating the sample is brought to room temperature at a 5K/min rate. Usually when a film was previously grown the sputtering started at 2.5keV (several hours) and lowered to 1keV

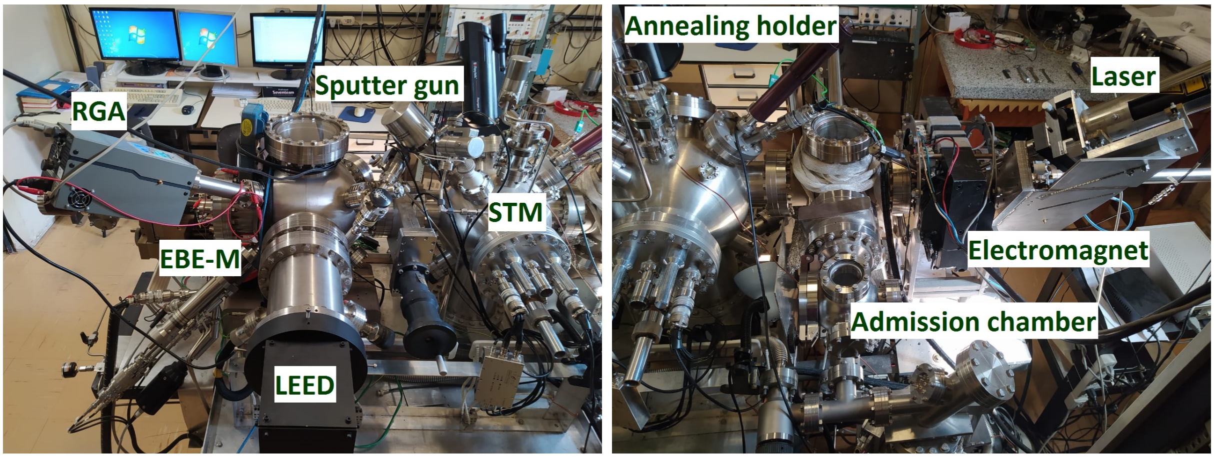

(a) LEED, e-BEAM and STM.

(b) Annealing Stage and Kerr Magnetometer.

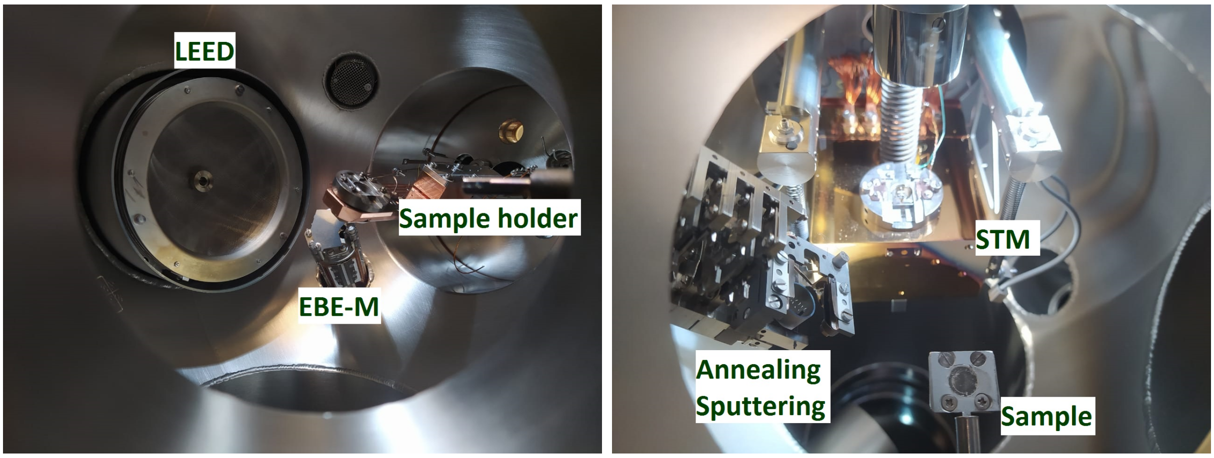

(c) Evaporation chamber.

(d) STM chamber.

Figure 3.1—Experimental setup. Image (a) shows an upper view of the UHV system evidencing the STM apparatus, the Sputter gun, RGA (Residual Gas Analyzer), the LEED optics and the evaporator EBE-M model (Specs). Image (b) shows the external magneto-optical setup evidencing the He-Ne Laser, the electromagnet and the load lock chamber. Image (c) is a internal view of the evaporation chamber, showing the EBE-M evaporator, the arm of the sample stage and the LEED-optics. Image (d) shows the internal view of the STM chamber, evidencing the tunneling microscope, the holder used for annealing and sputtering, and the sample itself.

for the cycling. The well-ordered (substrate) surface was frequently verified by STM imaging and LEED pattern. The best preparation parameters were achieved when a clear vicinal surface reconstruction (without impurities) was observed by both techniques.

After the preparation of the substrate, it is transferred from the sputtering/annealing stage (see figure 3.1) to the evaporation chamber, using a long magnetically coupled mechanical arm. Immediately after the growth of the film, the sample is transferred back to the STM chamber for analysis of its structural properties using the microscope. The magnetic properties could be then investigated when the sample is transferred to the MOKE chamber. The sample must first be perfectly placed at the center of the electromagnet, and aligned with the laser beam for MOKE measurements. More details about those experiments are provided in the next sections.

This work focuses on the investigation of the structural, morphological and magnetic properties of few monolayers (ML) of Fe and Co deposited on Ag(977). Iron thickness were of 0.5, 1.0, 2.0, 3.0, 4.0, 5.0 ML, while cobalt thickness were 0.5, 2.0, 3.0, 4.0, 5.0 ML. Both systems were prepared at evaporation temperature of 300K, 400K and 500K.

3.1 LEED - Low Energy Electron Diffraction

LEED is a technique based on the diffraction of low energy electrons to investigate surface structure. From the diffraction pattern we have access to the structural arrangement, and it can be used either for a qualitative or quantitative analysis. Aiming only the atoms at the surface (against the bulk) it is necessary to use low energy atoms, ions or electrons, which do not penetrate deeply into the sample.[76] The diffraction with electrons is very appropriated, because it penetrates only few Angstroms into matter. A low energy electron beam is directed towards a sample surface causing backscattering of electrons. The crystallographic arrangement of the surface atoms produces constructive interference at specific angles which can be visualized on a phosphor LEED screen, as shown in figure 3.2a. Typically the electron energy is in the range of 20 to 1000 eV. In this work we have used energy in the range 40-400 eV.

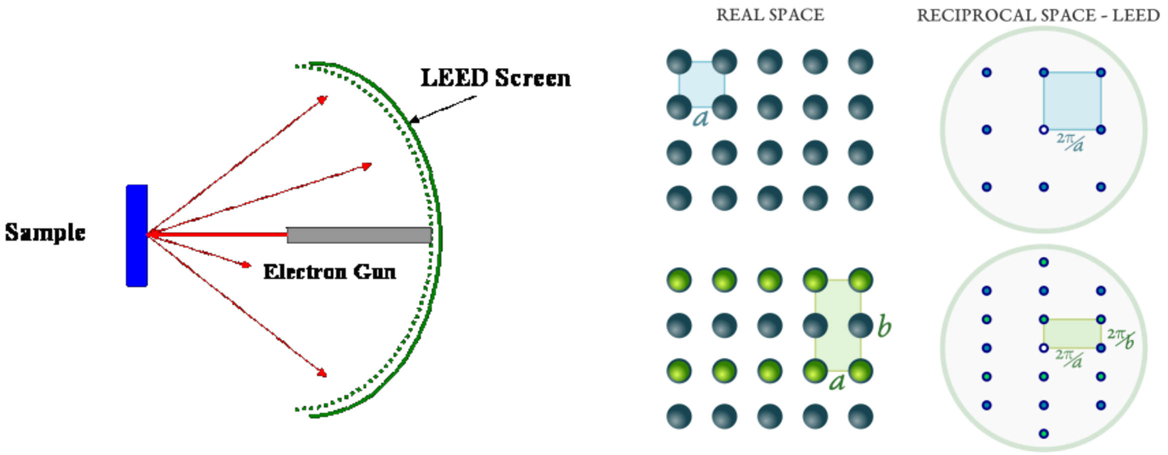

(a) (b)

Figure 3.2—LEED scheme. Experimental setup (a) and representation of the LEED diffraction pattern (reciprocal space) accordingly to the crystal structure (real space) (b). Adapted from Ponor (2020).[77]

The Leue condition for constructive interference imposes restrictions to wave vector, i.e., $\mathbf{k}_s - \mathbf{k}_i = \mathbf{K}_{hkl}$, where $\mathbf{k}_s$ and $\mathbf{k}_i$ are the scattered and incident wave vector, respectively. $\mathbf{K}_{hkl}$ represent the reciprocal lattice vector, $\mathbf{K}_{hkl} = h\,\mathbf{b}_1 + k\,\mathbf{b}_2 + l\,\mathbf{b}_3$. The position of each spot on the LEED pattern is determined by the atom arrangement (real space), so that the pattern reproduces the reciprocal space. If the atomic lattice constant at real space is a, the distance of each spot at LEED pattern is $2\pi/a$, as shown in figure 3.2b.

On vicinal surfaces, there are two kinds of periodicities: one related to the atomic arrangement of the flat terraces and the other one due to the array of periodic steps. Consequently the diffraction requires constructive interference with respect to both conditions. Therefore, the LEED pattern of stepped surface is a superposition of constructive interferences of both periodicities. In analogy with flat surfaces, here the distance between two spots on the LEED pattern is $2\pi/Na$, where N is the number of atoms at the terrace and a is the atomic distance. The other spot - due to step periodicity - has the Leue condition $\Delta k = 2\pi p/h$, where h is the distance between the steps.

3.2 STM - Scanning Tunneling Microscopy

The Scanning Tunneling Microscopy (STM) is an experimental method created by Gerd Binnig and Heinrich Rohrer (Nobel Prize 1986) based on the quantum tunneling effect between a sharp metallic wire tip and a conductor surface.[78] Typically, the tip is a wire of platinum (Pt), tungsten (W) or gold (Au). With STM it is possible to obtain the topological map of a conducting substrate.

Figure 3.3 shows a schematic of a STM apparatus. Between tip and sample, the vacuum acts as an energy barrier, which avoids electrons to be transmitted from one side to the other. However, bringing the tip closer to the substrate and applying an electrical potential difference V_z there is a non-zero probability of electronic tunneling (at Fermi level) from sample to tip. The resulting tunneling current is a function of the tip position, applied voltage and the local density of states (DOS) of the sample. The most commonly used method for STM imaging is done by maintaining the tunneling current constant, while scanning the tip over the sample and controlling the z-position. The xy scan is achieved by a piezoelectric motor that uses the piezoelectric effect. This effect in piezoceramics converts electrical field to mechanical strain. From the experimental point of view, the production of good STM images requires good vacuum, temperature control, as well as isolation from electrical interference and external mechanical oscillations or excitation, making this technique highly sensitive to external perturbations.

The electrons at the Fermi level with the sample positioned at a distance d from the tip, experience a strong energy barrier with the work function represented by Φ. Applying a bias voltage on the sample, its Fermi level is elevated. In this situation, by decreasing d, the wave functions of the tip and sample overlap themselves, allowing electronic tunneling from the

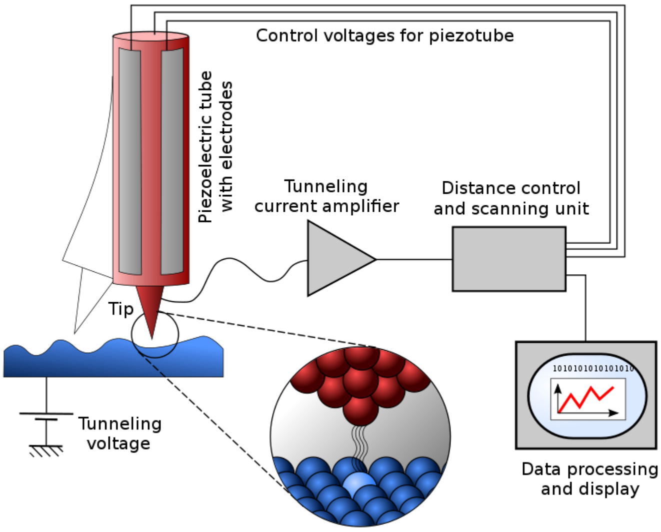

Figure 3.3—STM schematic. Tunneling of electrons from the sample to tip provides a 3D z-map, by controlling z at I_{tunnel}=constant. Reprinted from Schmid and Pietrzak (2005).[79]

occupied (sample) to unoccupied states (tip). With an appropriate V_z, a tunneling current I is established and can be represented as

$$I(d) \propto eV_z\ exp\left[-2d\frac{\sqrt{2m\Phi}}{\hbar}\right] \tag{3.2.1}$$

where e, m are the charge and mass of electron, respectively. Typically the work function Φ assumes values $\sim$ 4 eV for a metal, the tunneling current reduces by a factor ~10 with each increase of 1.0 Å in d, because I has a (negative) exponential dependence with d. For example, if the typical atomic diameter is $\sim$ 3.0 Å, the tunneling current changes by a factor $\sim$ 1000. Therefore, STM is considered a highly sensitive experimental method, capable of producing images with atomic resolution.

3.3 MBE - Molecular Beam Epitaxy

Molecular Beam Epitaxy (MBE) is a deposition technique usually employed in UHV environment, used to grow thin and ultrathin films with control of thickness, chemical composition and morphology. Based on epitaxial growth, MBE produces thin layers with higher quality and ultra-pure (free of impurities) when compared to *ex-situ* techniques.

In this work we have used a four pocket MBE evaporator from SPECS (model EBE-M) installed in the evaporator chamber (see figure 3.1). Its operation is sketched in figure 3.4. A short ultra-pure metal rod (electrically isolated from ground) is positioned near to a tungsten filament, usually 2 mm fall apart. The filament is heated by an electric current (3.6 A) causing electron thermionic emission. A high voltage (~1500 V) is applied to the wire (or rod) attracting the electrons, causing a localised heating at the top end of this rod and the evaporation of metal atoms.

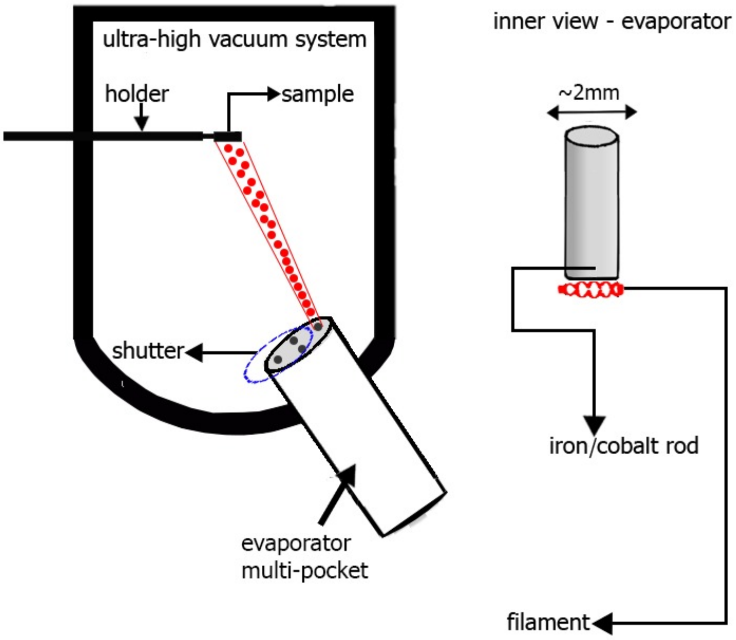

Figure 3.4—MBE scheme: a short rod (heated by an electron beam) ejects atoms towards the sample surface.

The atom-flux of the electron-beam evaporator can be monitored and controlled by a feedback electronic system. A current of ion-atoms is measured through an electrode in front of the evaporator (proportional to atom-flux) and the electron emission current is controlled in order to maintain a constant flux. A shutter can be eletro-mechanically opened and closed to establish evaporation time.

To ensure methodical growth it is necessary to calibrate the coverage as a function of the evaporation time, that is, to establish the evaporation rate τ (ML/s). For that, we have fixed the acceleration voltage at 1500 V and a flux of 3.0 nA. To calibrate the coverage rate τ we have evaporated iron and cobalt individually on a clean Ni(111) surface. Some STM results of a 360s of deposition of Fe and Co are shown in fig. 3.5. Calibration samples were produced with different deposition times (120s, 240s, 360s and 480s) at room temperature, and several STM images were recorded. The images (scanning area from 500 x 500 Å to 2000 x 2000 Å) were analysed using the WSxM software[80] to evaluate the coverage of each one. The average coverages and their uncertainties (1 standard deviation) are shown in fig. 3.6. For both cases, Fe/Ni111 and Co/Ni(111) there is a linear relationship between the coverage and the evaporation time. From the linear fits we calculated the deposition time of 01 monolayer (1 ML) of iron and cobalt, which are $T_{Fe} = (571 \pm 29)$s and $T_{Co} = (598 \pm 30)$s, respectively. In other words, the coverage ratio for iron is $\tau_{Fe} = (1.75 \pm 0.09) \times 10^{-3}$ ML/s and for cobalt $\tau_{Co} = (1.67 \pm 0.08) \times 10^{-3}$ ML/s. For more details see Appendix B.

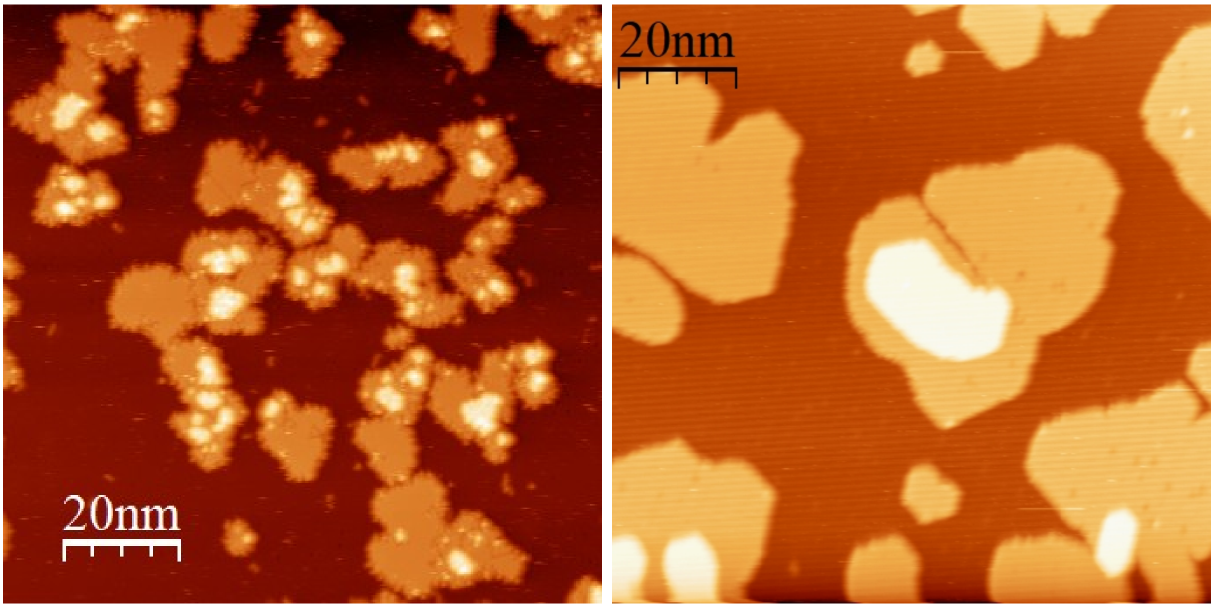

(a) Fe/Ni(111). (b) Co/Ni(111).

Figure 3.5—STM images of Fe/Ni(111) with coverages of $\mu_{Fe} = (62.9 \pm 2.2)$ % (left) and Co/Ni(111) with $\mu_{Co} = (53.9 \pm 2.4)$ % (right) after 360 seconds of deposition.

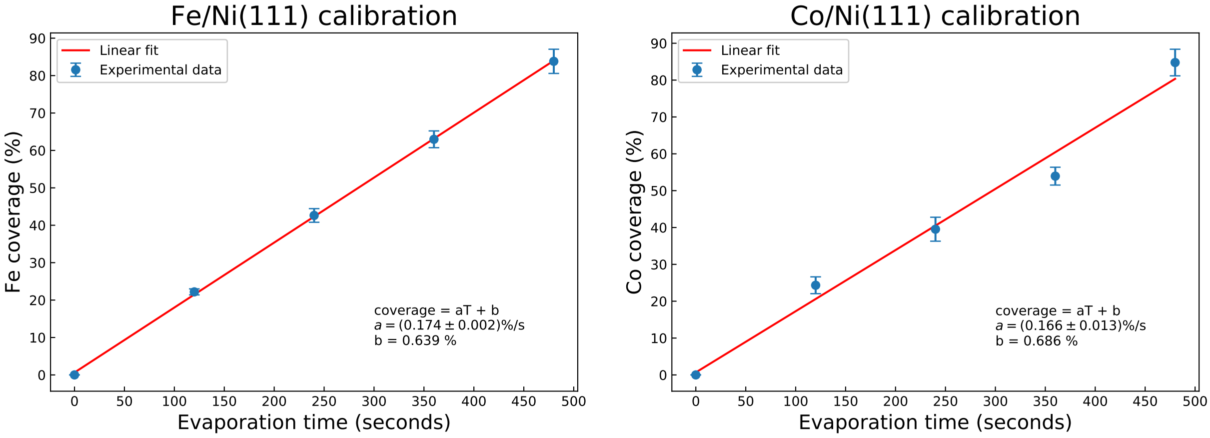

(a) Fe/Ni(111). (b) Co/Ni(111).

Figure 3.6—Fe (left) and Co (right) coverage versus evaporation time on Ni(111). Those results were used to establish the evaporation rates of Fe and Co.

3.4 MOKE - Magneto Optical Kerr Effect

As previously discussed (see section 2.3) by measuring the Magneto-Optical Kerr Effect one can infer about the surface magnetization of a sample by means of the observed changes on the polarization (rotation and ellipsity) of the reflected light beam. The experiment that uses the Kerr effect has three different configurations (see figure 3.7): i) Longitudinal (L-MOKE) when the magnetic field is applied at sample plane and parallel to the incidence plane ($\hat{y}$); ii) Transverse (T-MOKE) when **H** is applied on sample plane, however, perpendicular to magnetization direction ($\hat{x}$); iii) Polar (P-MOKE) when **H** is applied perpendicular to the sample plane ($\hat{z}$).

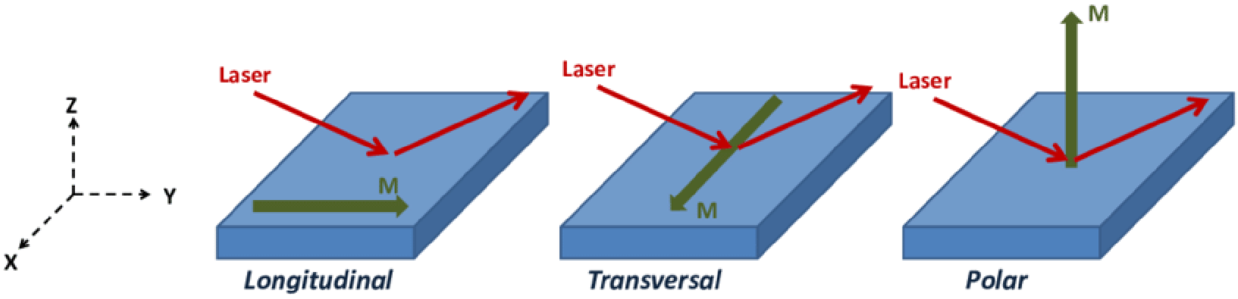

Figure 3.7—Three configurations of the MOKE experiment: from left to right, L-MOKE, T-MOKE, and P-MOKE. Reprinted from Merazzo (2012).[81]

The setup of the MOKE experiment is outlined in fig. 3.8 (polar configuration). Sequentially, the laser light is polarized, modulated by a photoelastic modulator (PEM), reflected by the sample, then passes through a polarizer (analyzer) and finally the intensity is detected by a photodiode. The laser is a He-Ne laser ($\lambda = 632.8$ nm), and the photoelastic modulater is a PEM-90 from Hinds, modulated at 50kHz. All optical components are located externally from vacuum, the laser light enters and comes out from the chamber through optical windows. The sample can be transferred *in-situ* to two positions of the arm of the Kerr magnetometer, allowing experiments in three configurations (polar, longitudinal and transversal) at a base pressure of 10^{-10}mbar. The homemade electromagnet is also mounted outside the vacuum chamber, has a water-cooling system, and reaches a magnetic field of 200 mT at the sample position. The electromagnet is rotatable around the MOKE-chamber, enabling an easy change from the polar ($\theta = 90^o$) to the longitudinal ($\theta = 0^o$) configurations. Another great feature is that the rotation of the magnet can be used to perform measurements with the applied field at any angle ϕ in the plane of the sample surface, from L-MOKE ($\phi = 0^o$) to T-MOKE ($\phi = 90^o$). This is particularly useful to investigate in-plane anisotropies of ultrathin films grown on the vicinal Ag(977), as will be shown latter.

As explained before (see section 2.3) the Kerr effect signal responds to any modification of the polarization of the reflected light, which is influenced by the magnetization of the sample.

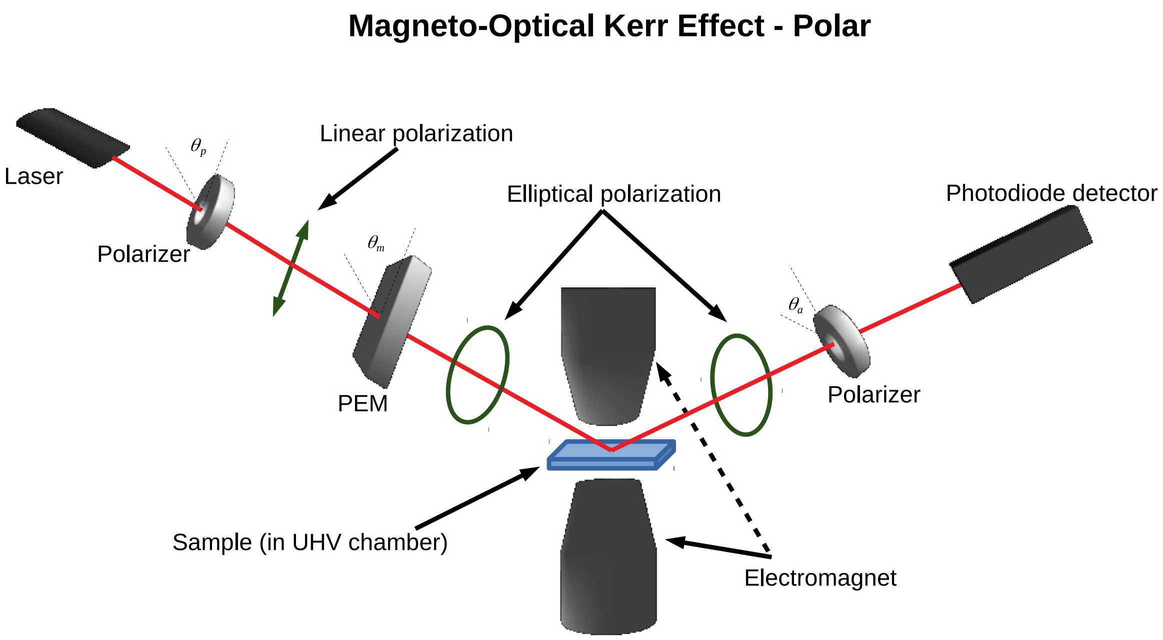

Figure 3.8—Polar MOKE experimental setup. Light from a He-Ne laser passes through a polarizer and a photoelastic modulator (PEM) becoming elliptically polarized. The light, after being reflected by the sample, goes through a polarizer and its intensity is measured by a photodiode detector as a function of applied magnetic field.

Because of the use of several optical elements, the measured (normalized) Kerr intensity can be expressed as[75]

$$I_q = \pi_q/\pi_{dc} = |\mathbf{A}.\mathbf{S}.\mathbf{M}.\mathbf{P}.\mathbf{E}_L|^2/\pi_{dc}, \tag{3.4.2}$$

where I_q, π_q, π_{dc} represent the final intensity, non-normalized (ac) intensity and the measured continuous (dc) intensity, respectively. Here, the subscript q can represent ω or 2ω, which are the demodulation frequencies of the lock-in. $\mathbf{E}_L$ is the Jones vector representing the polarized laser light, $\mathbf{P}$ is the polarizer's Jones matrix, $\mathbf{M}$ is the Photoelastic Modulator (PEM) matrix, $\mathbf{S}$ is the Fresnel reflection coefficients matrix, and $\mathbf{A}$ is the matrix of the polarizer/analyzer. $\mathbf{E}_L$ is represented by

$$\mathbf{E}_L = E_0 \begin{bmatrix} p \\ s \end{bmatrix} \tag{3.4.3}$$

p, s represent the normalized components of the electrical field vector of light, parallel and perpendicular to the plane of incidence, respectively. The Fresnel reflection matrix $\mathbf{S}$ containing complex reflection coefficients r_{ij} is written as

$$\mathbf{S} = \begin{pmatrix} r_{pp} & r_{ps} \\ r_{sp} & r_{ss} \end{pmatrix}, \tag{3.4.4}$$

and the other optical elements are represented by

$$\mathbf{A}(\theta_a) = \begin{pmatrix} cos^2\theta_a & cos\theta_a sen\theta_a \\ cos\theta_a sen\theta_a & sen^2\theta_a \end{pmatrix}, \quad \mathbf{P}(\theta_p) = \begin{pmatrix} cos^2\theta_p & cos\theta_p sen\theta_p \\ cos\theta_p sen\theta_p & sen^2\theta_p \end{pmatrix}, \tag{3.4.5}$$

$$\mathbf{M}(\theta_m) = e^{-i\xi/2} \begin{pmatrix} cos^2\theta_m + sen^2\theta_m e^{i\xi} & sen\theta_m cos\theta_m(1-e^{i\xi}) \\ sen\theta_m cos\theta_m(1-e^{i\xi}) & sen^2\theta_m + cos^2\theta_m e^{i\xi} \end{pmatrix}, \tag{3.4.6}$$

where θ_p, θ_m, θ_a are the rotation angles, with respect to the plane of incidence, of the polarizer, modulator and analyzer, respectively. ξ is the phase difference (or phase retardation) which is created by the PEM. Gomes (2009)[75] studied the influence of all these parameters and has shown that, for this experimental setup, the best signal-to-noise ratio is achieved by using the following parameters for the optical elements:

$$\mathbf{E}_L = \frac{E_0}{\sqrt{2}} \begin{bmatrix} 1 \\ 1 \end{bmatrix}, \;\; \theta_p = 45^\circ, \;\; \theta_m = 0^\circ \;\; and \;\; \theta_a = 0^\circ \;\; or \;\; 90^\circ. \tag{3.4.7}$$

Introducing these parameters in equation 3.4.2 and using the Bessel function roots J_1 and J_2, the intensities are

$$\pi_{dc} = E_0^2 |r_{pp}^0|^2, \tag{3.4.8}$$

$$\pi_{2\omega} = -4E_0^2 J_2 Re(r_{pp}^0 r_i^*), \tag{3.4.9}$$

$$\pi_{\omega} = 4E_0^2 J_1 Im(r_{pp}^0 r_{pp}^*). \tag{3.4.10}$$

where r_i assumes the value r_{ps} for $\theta_a = 0^\circ$ and r_{sp} for $\theta_a = 90^\circ$.

Gomes (2009)[75] developed a method to determine the normalized magnetization $m_{xyz} = M_{xyz}/M_s$ from the the measured Kerr signal intensities. This method, called Vector Magnetometry (based on magneto optical Kerr effect), uses the Fresnel coefficient r_{sp} and r_{ps} to determinate for instance m_y (in plane magnetization, parallel to the plane of incidence) and m_z (out of plane magnetization) - see fig. 3.7. Briefly, by this method, m_y and m_z are given by

$$m_y = \sqrt{2} n(1+\kappa^2) A'' \left[\frac{Y_2^2 + Y_1^2}{Y_1 \kappa - Y_2} \right] \;\; and, \tag{3.4.11}$$

$$m_z = \sqrt{2}n(1+\kappa^2)A'' \left[\frac{Z_2^2 + Z_1^2}{Z_1(y+\kappa x) - Z_2(x-\kappa y)} \right], \tag{3.4.12}$$

where n is the real part of thin film refractive index and κ is the extinction coefficient. $n\kappa$ is the absorption coefficient, so that the complex refractive index is $n_{film} = n(1-i\kappa)$. The functions Y_1, Y_2, Z_1 and Z_2 are related to experimental intensities ($I_{\omega,2\omega}^{0,90}$) as follows

$$Y_1 = -\frac{I_{2\omega}^{90}}{J_2} + \frac{I_{2\omega}^{0} r_{ss}^r}{J_2} - \frac{I_{\omega}^{0} r_{ss}^i}{J_1} \quad , \quad Y_2 = \frac{I_{\omega}^{90}}{J_1} + \frac{I_{2\omega}^{0} r_{ss}^i}{J_2} + \frac{I_{\omega}^{0} r_{ss}^r}{J_1}, \tag{3.4.13}$$

$$Z_1 = \frac{I_{2\omega}^{90}}{J_2} + \frac{I_{2\omega}^{0} r_{ss}^r}{J_2} - \frac{I_{\omega}^{0} r_{ss}^i}{J_1} \quad and \quad Z_2 = -\frac{I_{\omega}^{90}}{J_1} + \frac{I_{2\omega}^{0} r_{ss}^i}{J_2} + \frac{I_{\omega}^{0} r_{ss}^r}{J_1}, \tag{3.4.14}$$

with the intensities $I_{\omega,2\omega}^{0,90}$ representing the $\omega, 2\omega$ signals measured with the polarizer/analizer at $\theta_a = 0°, 90°$. J_1 and J_2 are roots of the Bessel functions. We have used a retardation angle of the photoelastic modulator, $\alpha = 137.8°$, which is known to nearly maximize both $J_1(\alpha)$ and $J_2(\alpha)$. That way, we also nearly maximize the first (ω) and second (2ω) harmonic terms.[75,82] In equations 3.4.13 and 3.4.14, $r_{ss}^{r,i}$ are the real and imaginary parts of the Fresnel coefficient r_{ss}, such that $r_{ss} = r_{ss}^r + ir_{ss}^i$. These coefficients can be calculated as

$$r_{ss}^r = \frac{1 - x^2 + y^2}{(1+x)^2 + y^2} \quad and \quad r_{ss}^i = -\frac{2y}{(1+x)^2 + y^2}, \tag{3.4.15}$$

where x, y are functions of the refractive index of the thin film,

$$x = \frac{1}{\sqrt{2}}\sqrt{\sqrt{a^2+b^2} + a} \quad and \quad y = \frac{1}{\sqrt{2}}\sqrt{\sqrt{a^2+b^2} - a}, \tag{3.4.16}$$

where $a = 2n^2(1-\kappa^2) - 1$ and $b = -4n^2\kappa$. m_x can also be calculated from measured intensities as

$$m_x = \frac{|r_{ss}|^4(|r_{ss}|^2 + 1)^2}{16 J_2 Re(r_{pp}^0 \Gamma)} (I_{2\omega}^{45} - I_{2w}^{-45}), \tag{3.4.17}$$

with Γ representing the function which depends of the complex magneto-optical constant Q,

$$\Gamma = \frac{2i\mu_1\mu_2 n_1 n_2 cos\,\theta_1 sin\,\theta_2\, Q}{\mu_1 n_2 cos\,\theta_1 + \mu_2 n_1 cos\,\theta_2}, \tag{3.4.18}$$

where θ_1, θ_2 are the incidence and refraction angles; μ_1, μ_2 the media magnetic permeability; and n_1, n_2 the media refractive indices.

Then, by doing measurements with the analyzer rotated by 45° it is possible to extract m_x. However, in this work, we decided to apply the Normalized Vector Magnetometry based on Kerr effect to determine only m_y and m_z, therefore the polarizer/analizer was positioned at 0° and 90° during all MOKE measurements, which simplifies and speeds up data collection. Meanwhile, because we have also performed experiments rotating the electromagnet (consequently the direction of the magnetic field) around the film plane (ϕ), we could by this method investigate the in-plane magnetic anisotropy. We have, for instance, explored the coercive field as a function of ϕ and determined the easiest in-plane axis. The STM and MOKE results are presented in the next chapter, with special attention in the discussion to the correlation of structural and magnetic properties of the investigated systems.

Chapter 4

Experimental results

As mentioned before (chapter 3) the investigation of structural and magnetic properties of ferromagnetic nanostructures (eventually self-assembled) on vicinal surface Ag(977) was carried out depositing iron (Fe) and cobalt (Co). We have prepared Fe and Co films in the range 0.5ML-5.0ML, and have investigated the influence of growth temperature (300K, 400K, 500K) on the morphology and on the magnetic behavior. Each preparation has started from a atomically clean Ag(977), which means before each preparation the sample has been subjected to a vigorous sputtering to remove the last film (several hours), and then to sputtering-annealing cycles to re-prepare the Ag(977) surface. STM imaging was frequently performed to assure the quality of the Ag(977) stepped surface. A LEED image taken at 70eV and a STM image (200Å×200Å) are shown in figure 4.1. The observed diffraction pattern of Ag(977) (fig. 4.1.a) is characteristic of a stepped surface, i.e due to both the atomic arrangement and the steps array (see section 3.1 for more details). Figure 4.1.b is the STM image of clean Ag(977) taken at 45° clockwise to the horizontal axis, where well ordered terraces are observed. The next two sections are dedicated to show the experimental results of theses samples.

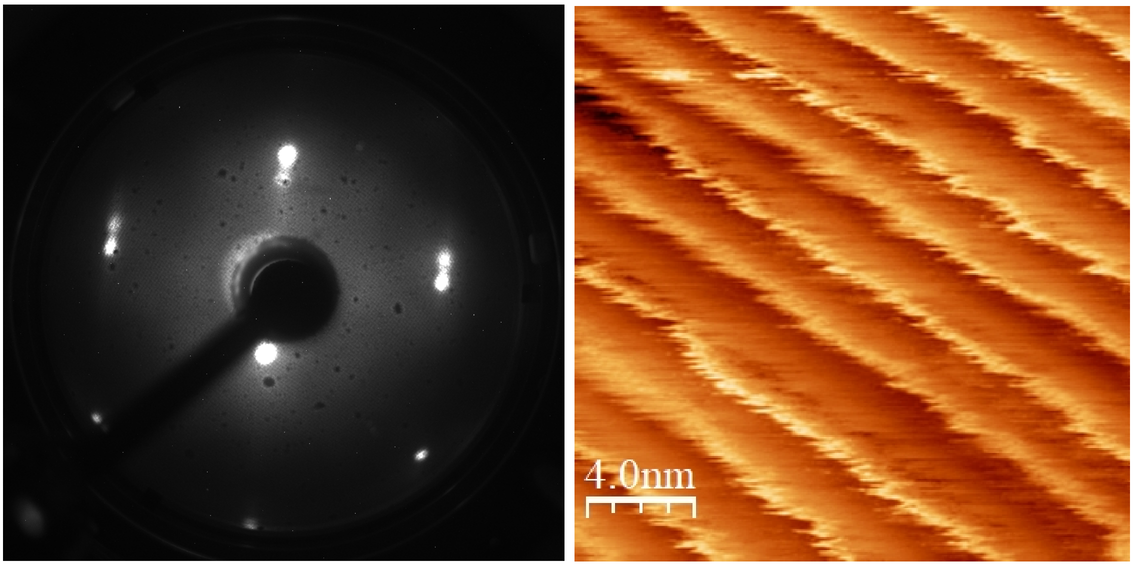

(a) (b)

Figure 4.1—LEED image at E_{cin}=70eV (a) and STM image (200Å×200Å) (b) of clean and ordered Ag(977).

4.1 Fe/Ag(977)

4.1.1 Growth morphology

The MBE growth of Fe was performed at an atom flux of $(1.75 \pm 0.09) \times 10^{-3}$ML/s and a base pressure of 10^{-9}mbar. Each sample started from a fresh prepared Ag(977) surface, and the crystal was kept at one of the selected temperatures: 300K, 400K or 500K. The STM images (1000Å×1000Å) of the Fe/Ag(977) samples are presented in figures 4.2-4.4. For 0.5ML (figure 4.2) the STM images show that at room temperature, the grain size is in the order of 3.1 nm, accordingly to the statistic analysis presented in Appendix C. However, by increasing the substrate temperature during the evaporation (T_s) the grain size decreases to 2.7 nm for $T_s = 400$K and to 2.3 nm for $T_s = 500$K. Besides that, we observe that the iron grains grow on top of each step edge as theoretically predicted (see chapter 2), and this behavior is clearly seen in figure 4.2.b.

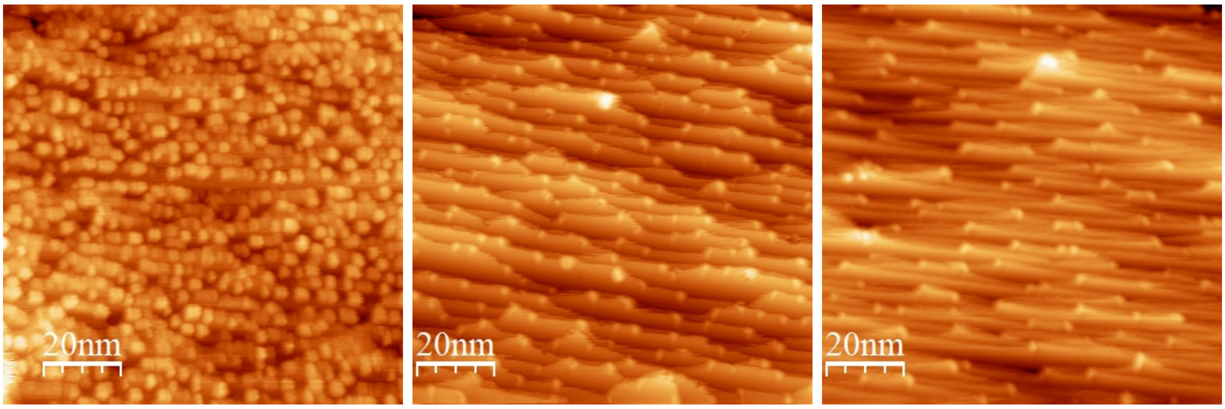

(a) 0.5ML, $T_s = 300$ K. (b) 0.5ML, $T_s = 400$ K. (c) 0.5ML, $T_s = 500$ K.

Figure 4.2—STM images of 0.5ML Fe/Ag(977) at substrate temperature $T_s = 300$ K (room temperature) (a), $T_s = 400$ K (b), and $T_s = 500$ K (c). The vicinal surface has its steps almost parallel to the horizontal axis, actually ca. $5^o - 10^o$ tilted clockwise. Step down is in the (positive) vertical direction

.

For a thickness of 1.0ML (see figures 4.3abc) at room temperature the average grain size is 5.4 nm, it decreases for $T_s = 400$K to 4.1 nm, and increases again to 6.0 nm for $T_s = 500$K. For thickness above 1.0ML at room temperature (see figures 4.3 and 4.4), we observe the formation of self-assembled nanostructures of agglutinated iron particles that resemble nanowires. These structures appear to fill the entire substrate, respecting a space between them. From the statistic analysis, which is presented in Appendix C, we notice that these nanostructures have different lengths (between 7.5 nm and 14.1 nm), their width size is in the range of 2.7 nm to 4.7 nm (see figs. C.1, C.2 and C.3), and they are aligned in the steps direction. The space between the nanowires is in the range (0.60 ± 0.04)nm at 2.0 ML, to (1.32 ± 0.02)nm at 5.0 ML, (see fig. C.5) and the height of each individual nanowire is in the range (3.5 ± 0.2)Å at 4.0 ML, to (8.6 ± 0.4)Å at 5.0 ML (see fig. C.6).

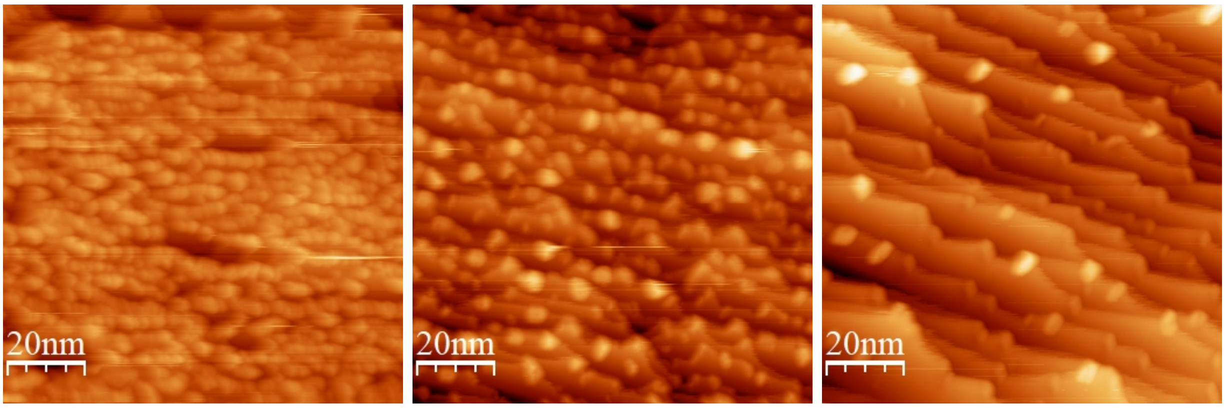

(a) 1.0ML, $T_s = 300$ K. (b) 1.0ML, $T_s = 400$ K. (c) 1.0ML, $T_s = 500$ K.

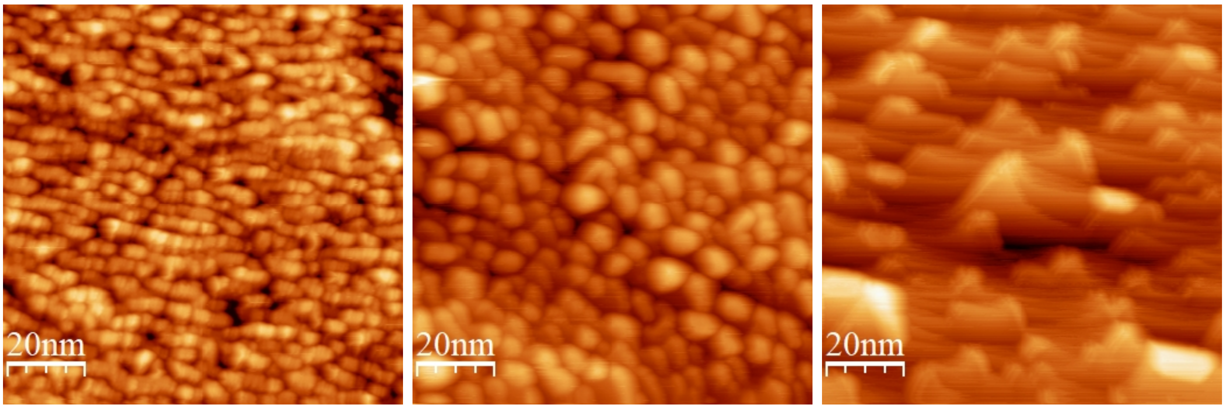

(d) 2.0ML, $T_s = 300$ K. (e) 2.0ML, $T_s = 400$ K. (f) 2.0ML, $T_s = 500$ K.

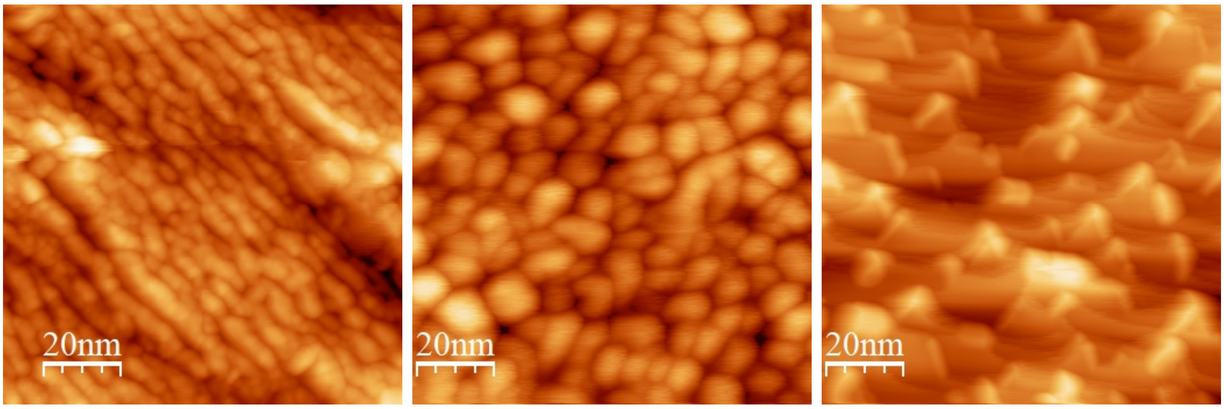

(g) 3.0ML, $T_s = 300$ K. (h) 3.0ML, $T_s = 400$ K. (i) 3.0ML, $T_s = 500$ K.

Figure 4.3—STM images (1000Å×1000Å) of 1.0ML, 2.0ML and 3.0ML Fe/Ag(977) grown at 300K, 400K and 500K. Image (g) was taken at 45° clockwise related to the horizontal axis.

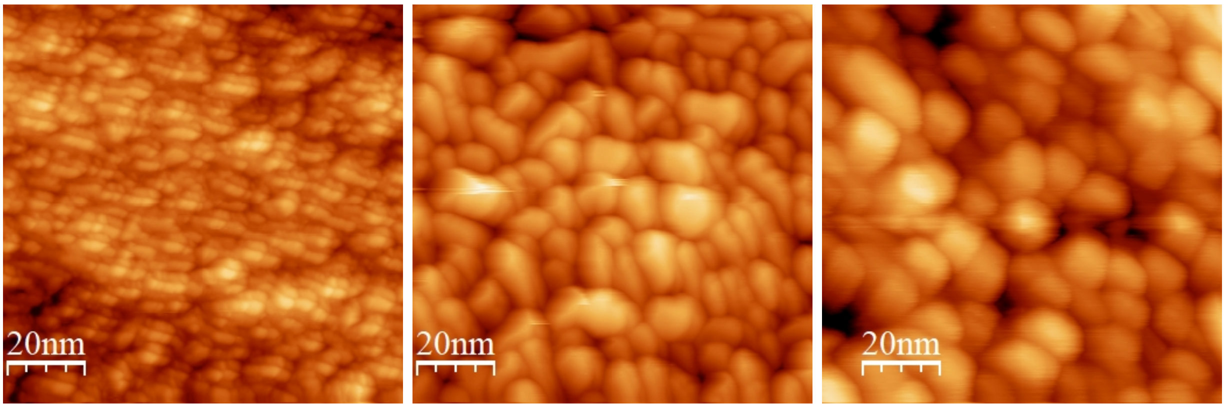

(a) 4.0ML, $T_s = 300$ K. (b) 4.0ML, $T_s = 400$ K. (c) 4.0ML, $T_s = 500$ K.

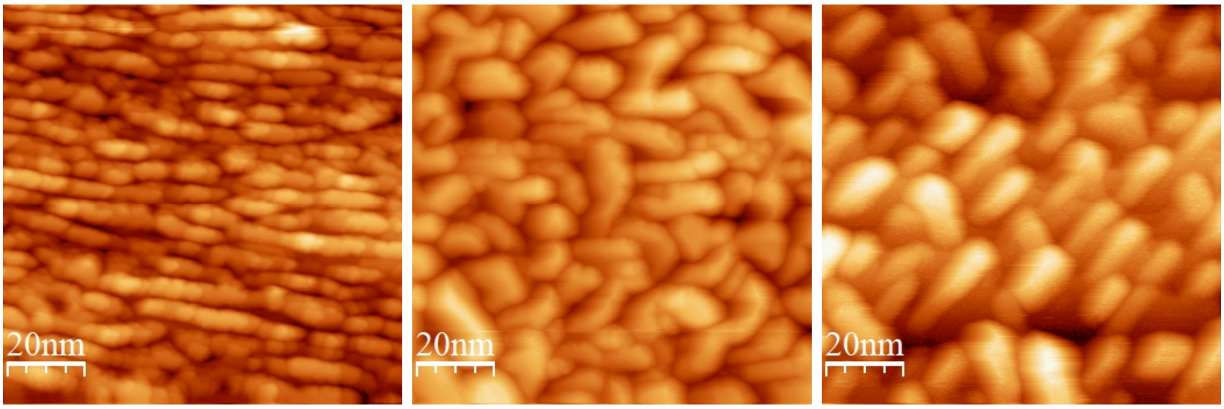

(d) 5.0ML, $T_s = 300$ K. (e) 5.0ML, $T_s = 400$ K. (f) 5.0ML, $T_s = 500$ K.

Figure 4.4—STM images (1000Å×1000Å) of 4.0ML and 5.0ML Fe/Ag(977).

The structural arrangement has been modified for all thickness investigated in this work, for growths at higher substrate temperatures (400K, 500K). At 400 K, it is observed predominantly circular shaped island growth (see figures 4.2 - 4.4). These structures increase almost linearly (see figure 4.5) with the iron thickness and they have average grain size diameters from 2.7 nm (0.5 ML) to 12.9 nm (5.0 ML), accordingly to the statistic analysis. Between 0.5 ML and 2.0 ML the iron nanoparticles align parallel to the step direction, however, for thickness above 2.0 ML no preferential direction is observed and the substrate is fully covered.

At 500 K, our STM results show that the growth process has two regimes: above and below 3.0 ML. Above 3.0ML, the growth does not show a preferred direction of alignment (see fig. 4.4cf) and the nanostructures have an average grain size of 12.9 nm (4.0 ML) and 16.9 nm (5.0 ML). For the lowest thickness (0.5 ML) the growth starts with smaller iron nanoparticles compared to the others temperatures. The average grain size for 0.5 ML at 500 K is 2.3 nm but at the same thickness, the grain size is 3.1 nm at 300K and 2.7 nm at 400K.

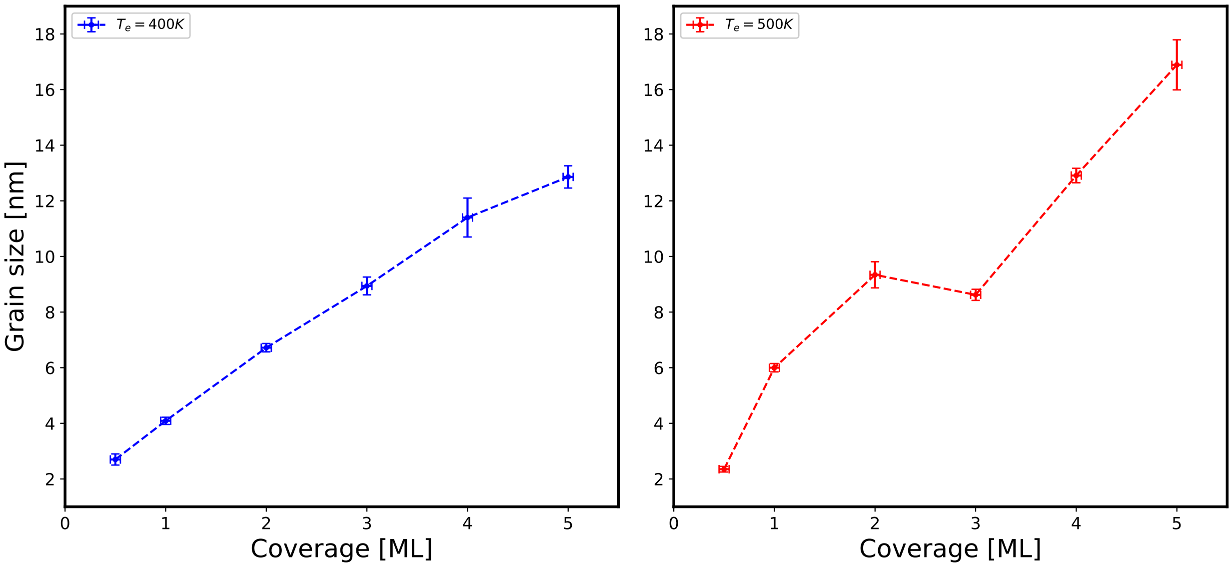

Figure 4.5—Grain size as a function of thickness for Fe/Ag(977) at T_s = 400 K (left) and 500 K (right). The grain size uncertainties were calculated as 1σ of the Gaussian fit and the uncertainty of the thickness, ± 0.05/ML. The dashed lines provide a guide for the eyes.

The growth at 500K induces the formation of triangular shaped structures from 0.5ML to 3.0 ML (see fig. 4.3cfi). Those structures at 500 K also present a linear behavior between grain size and thickness, as shown in figure 4.5 (right).

Most probably, what happens, is that for higher thickness and higher temperatures (400K and 500K), the growth kinetics of a thicker film is changed, it may not quite perceive the step topology of the vicinal surface because of the enhanced mobility of the atoms. On the other hand, even for our thicker film (5.0ML) grown at room temperature (see figure 4.4d) the nanostructures align nicely along the step edges, which is completely different from the morphologies seen at 400K and 500K (figs. 4.4ef).

4.1.2 Magnetic characterization

The magnetic characterization was performed using the magneto-optical Kerr effect. MOKE experiments were carried out using both polar and longitudinal configurations (see section 3.4 for more details). First, we have measured the magnetic signal of clean Ag(977) and its diamagnetic signal has been checked as shown in figure 4.6 (black curves).

The Kerr signals of our thinner samples (0.5, 1.0, 2.0 ML), measured in the longitudinal configuration, figure 4.6, appear to have the same diamagnetic signature of the clean Ag(977). Since they show no hysteresis loop, this may indicate that the thinner films are either superparamagnetic or that in-plane (longitudinal) is a hard axis. We'd like to call the attention for the STM images of these samples (figures 4.2 and 4.3) which exhibit grain sizes in the range from 2.3 nm (0.5 ML, $T_s = 500$ K) to 9.3 nm (2.0 ML, $T_s = 500$ K), which is indeed in the superparamagnetic size regime.

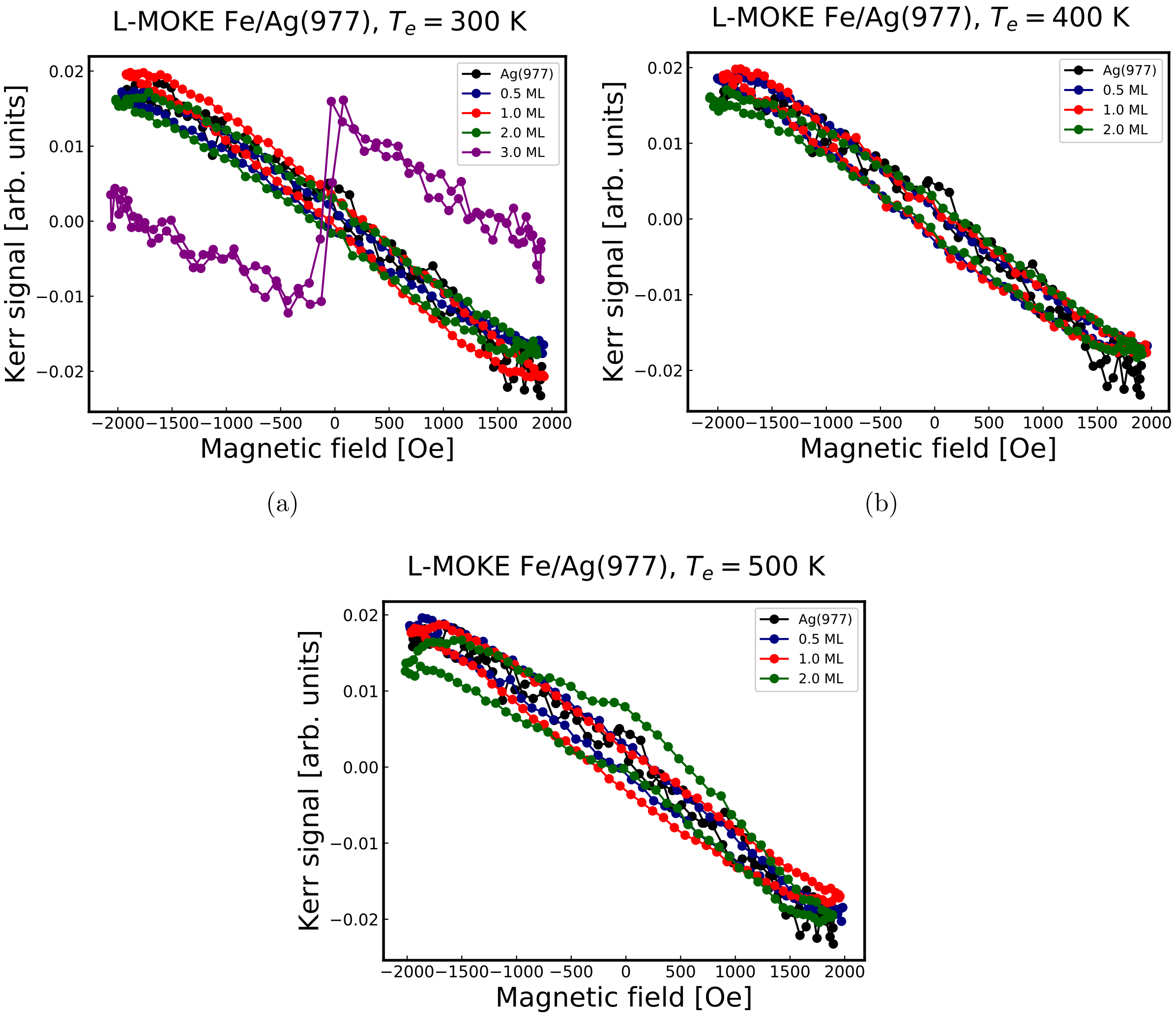

(a)

(b)

(c)

Figure 4.6—L-MOKE of 0.5 ML, 1.0 ML, 2.0 ML and 3.0 ML of Fe deposition on Ag(977) with the substrate at 300 K (a), 400 K (b) and 500 K (c).

At 3.0ML and $T_s = 300$K (see figure 4.6.a) the L-MOKE measurement has shown a clear signature of a ferromagnetic behavior of the film, in addition to the diamagnetism (negative slope) of the silver substrate. The coercive field is very low and its value was determined in a more detailed measurement (see fig. 4.8a).

In figure 4.7 the P-MOKE signals of the 2.0 ML - 5.0 ML films come indeed from the deposited iron, since their intensities (see their slopes) scale with thickness, and are much stronger than the diamagnetic signal from the silver substrate. For higher thickness, the curves instead of P-MOKE hysteresis loops, they present either a linear behavior or a Langevin type function, which indicates a hard axis of magnetization for the out-of-plane configuration.

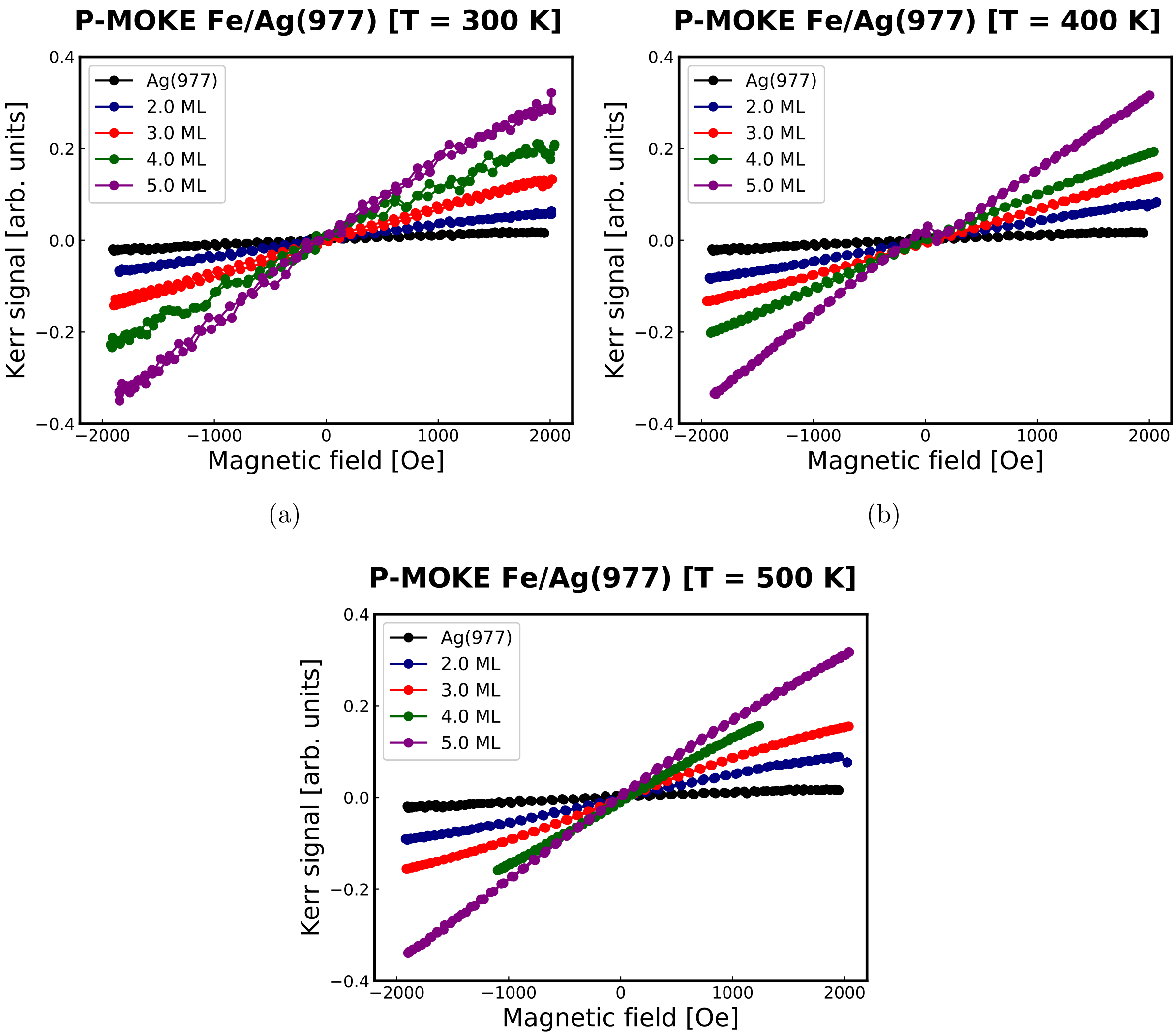

(a)

(b)

(c)

Figure 4.7—P-MOKE measurements for 2.0 ML - 5.0 ML of Fe/Ag(977) growtn at 300 K (a) 400 K (b) and 500 K (c).

The L-MOKE measurements, between 3.0 ML and 5.0 ML, present tilted hysteresis loops due to the addition diamagnetic and ferromagnetic signals. In order to separate the ferromagnetic signal from the diamagnetic contribution coming from the silver substrate, we have substracted a negative (diamagnetic) signal from the raw data. The negative slope to be subtracted must result in a ferromagnetic hysteresis with horizontal saturations at both positive and negative high fields. The final results can be seen in figures 4.8 and 4.9.

In figure 4.8 are shown the L-MOKE results for 3.0 ML, 4.0 ML and 5.0 ML of Fe deposited at room temperature. In the longitudinal configuration the magnetic field was applied in the step direction and all three samples exhibited hysteresis loops with well defined magnetic remanence and low coercive fields. Because of that, and the fact that the polar-MOKE results have shown a linear behavior, led us to the conclusion that the easy axis lies in plane of the surface. The coercive field increased from $H_c \sim 3.8$ Oe for 3.0 ML, to $H_c \sim 10.2$ Oe for 4.0 ML, and then abruptly to $H_c \sim 129.0$ Oe for 5.0ML. In fact the nanostructures (resembling nanowires) observed for 5.0ML-Fe/Ag(977), see figure 4.4d, are much bigger (and longer in the horizontal direction) as compared to the 3ML and 4ML thickness, which explains the larger coercive field. In other words, the energy needed to reverse the magnetization is greater for bigger domains, which increases the area of the hysteresis cycle.

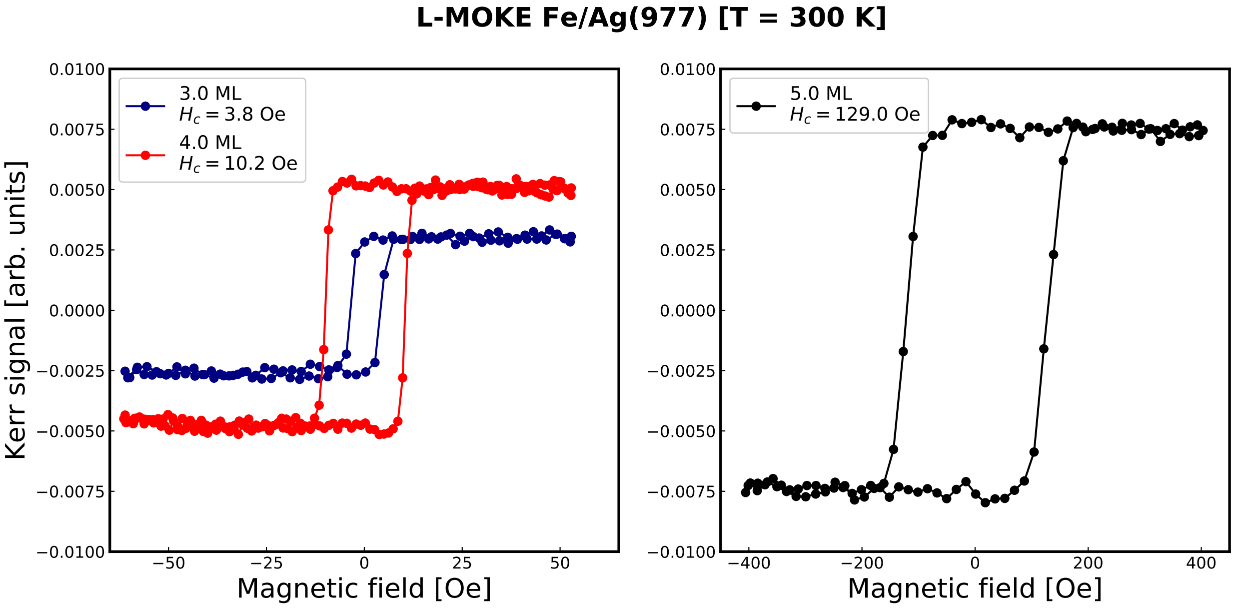

Figure 4.8—L-MOKE measurements of Fe/Ag(977) at 300 K for 2.0 ML and 3.0 ML (left side) and 5.0 ML (right side).

In figure 4.9 are shown the L-MOKE results (after substraction of the diamagnetic contribution from silver) for 3.0 ML, 4.0 ML and 5.0ML, at deposition temperatures of 400 K and 500 K. For 3.0 ML at 400 K, the curves present an anomalous ferromagnetic behavior and, therefore, no coercive field could be measured. For 4.0 ML and 5.0 ML, the L-MOKE signals also present complex hysteresis loops. Despite of that, we could measure the coercive fields: for 4.0 ML, $H_c \sim 21.4$ Oe and for 5.0 ML, $H_c \sim 43.2$ Oe. However, for 4.0ML at 500 K, we have observed a closed loop, without coercive field. And for 3.0 ML and 5.0ML, at 500K, we measured $H_c \sim 76.9$ Oe and $H_c \sim 22.9$ Oe, respectively.

In order to better explore the in-plane ferromagnetic properties, we have performed MOKE measurements rotating the electromagnet around the sample plane. The results are shown in

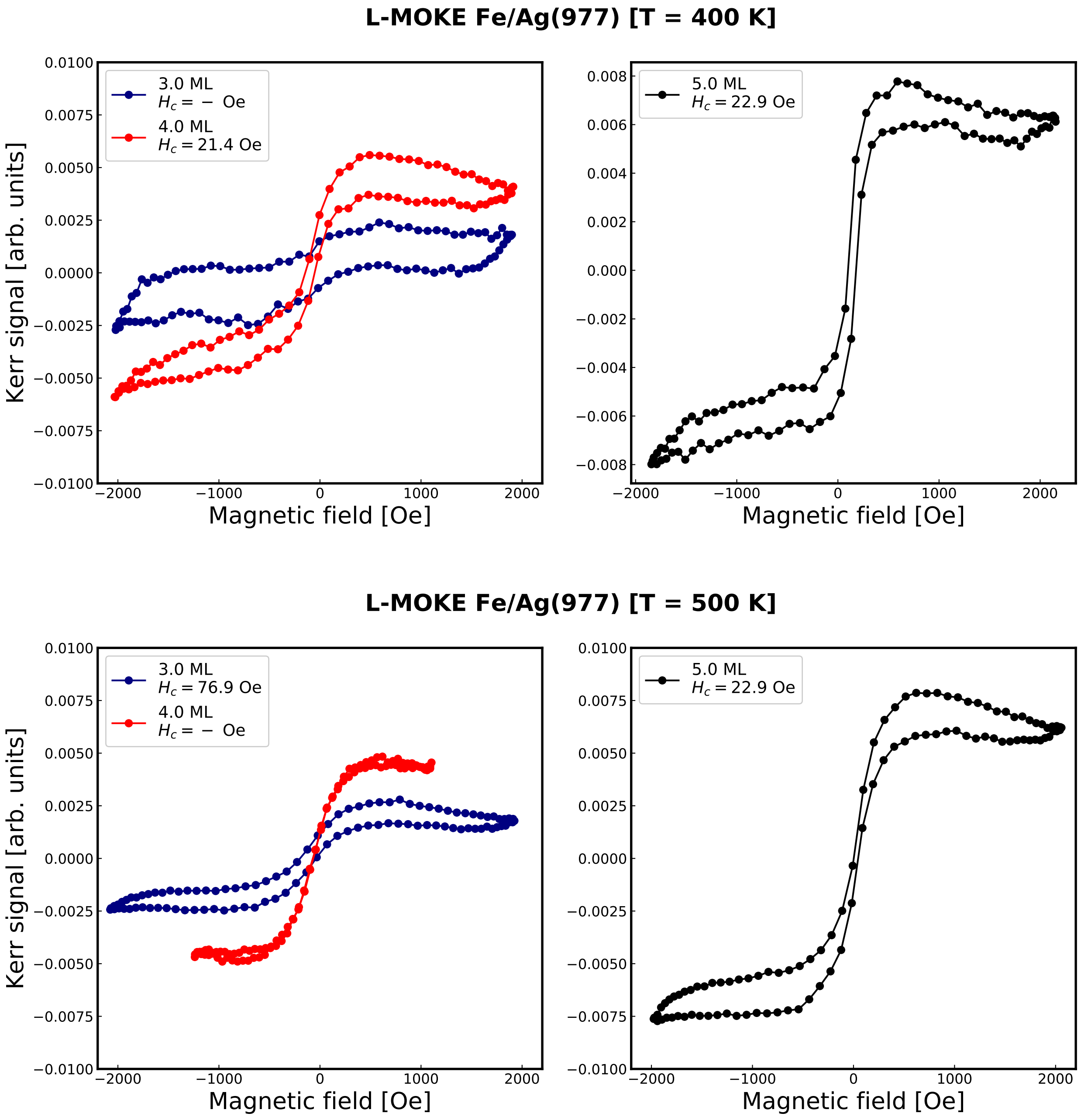

Figure 4.9—L-MOKE for 3.0 ML, 4.0 ML and 5.0ML of Fe grown on Ag(977) at 400 K (upper panel) and 500 K (lower panel).

figures 4.10, 4.11 and 4.12, for T_e = 300 K, 400 K, and 500 K, respectively. For films grown at room temperature, these measurements shows hysteresis loops for all azimuthal angles and the coercive field increases from $\phi = 0^o$ to 90°, which indicates an easy axis along the step edges ($\phi = 0^o$) and a 'harder' axis at 90^o. In figure 4.10, we present these measurements for Fe/Ag(977) grown at room temperature. For 3.0 ML, by changing the magnetic field direction (rotating ϕ), we observed an increase of the coercive field from 3.8 Oe to 11.8 Oe, for $\phi = 0°$ and $\phi = 90°$ respectively. For 4.0 ML, H_c varies from 10.2 Oe ($\phi = 0°$) to 104.7 Oe ($\phi = 90°$). And for 5.0 ML, the MOKE measurements show coercive fields in range of 129.0 Oe ($\phi = 0°$) to 621.8 Oe ($\phi = 90°$). See that H_c^{5ML} is 52.7 times greater than H_c^{3ML}, both at $\phi = 90°$, while the ratio H_c^{5ML}/H_c^{4ML}=5.9. These ratios indicate that at 5.0 ML the iron nanostructures must be much longer and wider, as compared to 3.0 ML and 4.0 ML, which is corroborated by the evolution of the sizes of the "nanowires" as a function of coverage observed in the STM images (figs. 4.3 and 4.4).

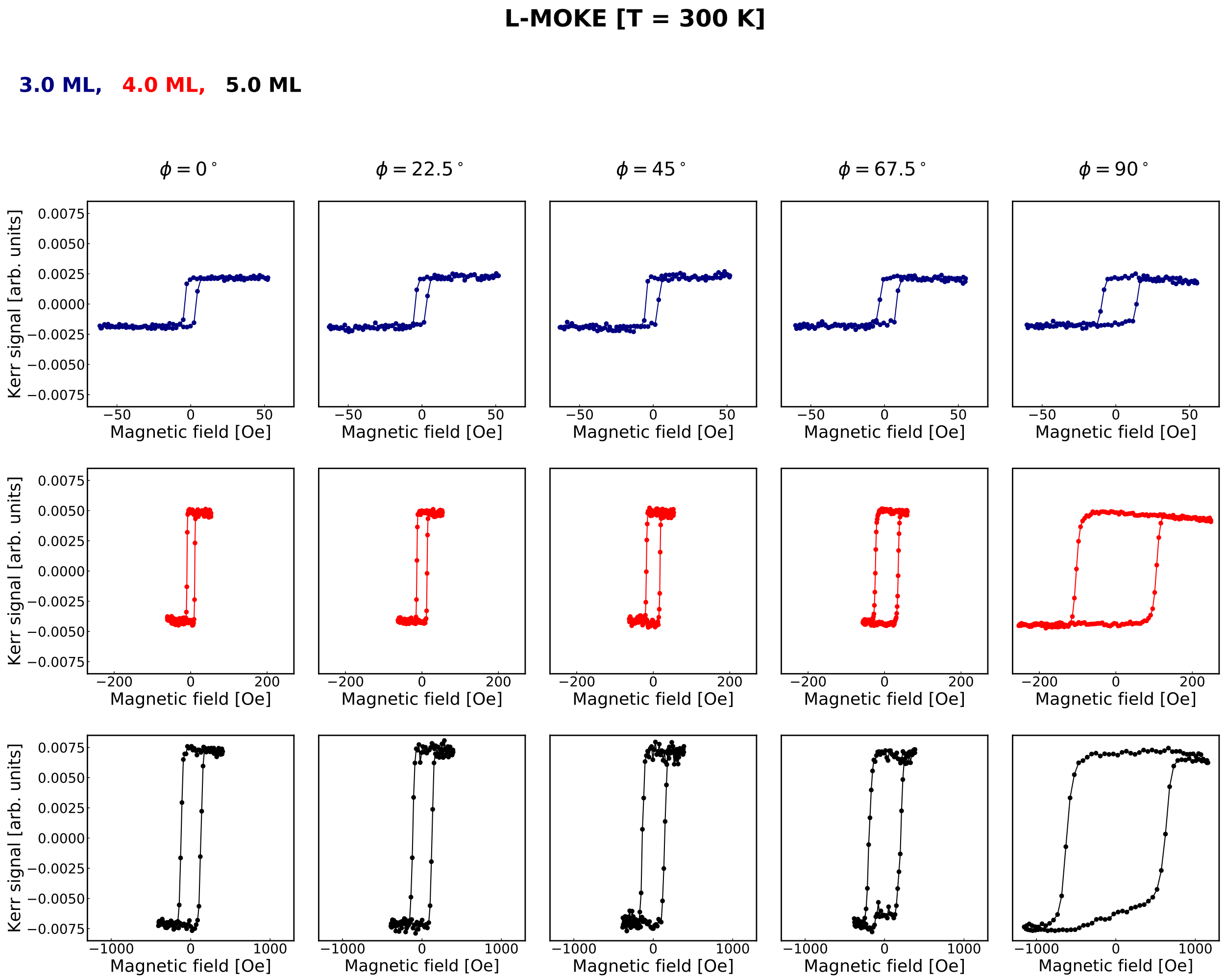

Figure 4.10—MOKE results as a function of the in-plane angle ($\phi = 0^o - 90^o$) of the applied magnetic field, for 3.0 ML (blue), 4.0 ML (red) and 5.0 ML (black) of Fe deposited on Ag(977) at 300K. Online colors.

For the deposition at 400 K of 3.0 ML Fe (see figure 4.11) the MOKE histeresis at $\phi = 0°$ looks anomolous as already mentioned, and by rotating ϕ the ferromagnetic signal was quenched for $\phi \geq 45°$. For 4.0 ML, the unusual shape of the MOKE curves may indicate superparamagnetic behavior, with dispersion on the sizes of the iron grains at the substrate surface. At 90^o the MOKE signal has changed its sign, from positive to negative, for $\phi \geq 67.5^o$. We don't have any good explanation for this effect at the moment, perhaps a change in the refractive index at this thickness and substrate temperature, which impacts the sign of the Kerr signal. 5.0 ML appears to have similar behavior, but changes earlier the sign of the MOKE curve, already at $\phi = 45^o$.

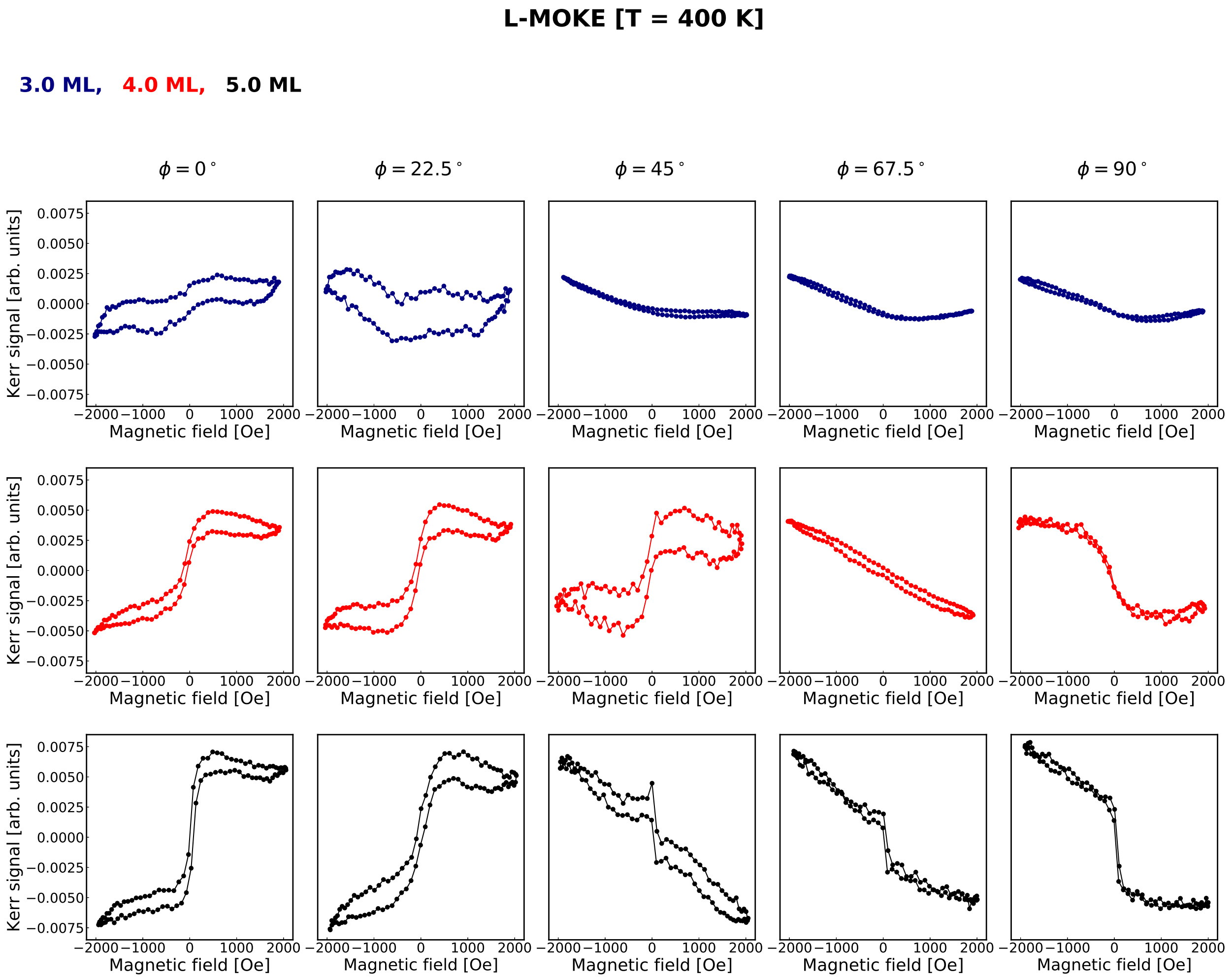

Figure 4.11—MOKE results as a function of the in-plane angle ($\phi = 0^o - 90^o$) of the applied magnetic field, for 3.0 ML (blue), 4.0 ML (red) and 5.0 ML (black) of Fe deposited on Ag(977) at 400K. Online colors

At T_s = 500 K (fig. 4.12), the 3.0 ML sample shows a coercive field H_c=76.9 Oe at $\phi = 0°$. Similarly to the previous temperature (400K) the ferromagnetic signal diminishes as the angle approaches 90^o. For 4.0 ML, there is no coercive field up to 45^o, and is only about 46.1 Oe at $\phi = 90^o$, supposedly a "harder" axis as compared to 0^o. The overall MOKE curves observed at this thickness and temperature indicates for a sample presenting superparamagnetism, or small ferromagnetic nanostructures e.g., the curve shown at $\phi = 0^o$ is typical of a superparamagnetic sample, and because of size dispersion at $\phi = 90^o$ some grains exhibit their "harder" axis. For 5.0 ML, the sample shows an easy axis at $\phi = 0°$ ($H_c \sim$ 22.9 Oe) and a "harder" axis at $\phi = 90°$ ($H_c \sim$ 41.2 Oe).

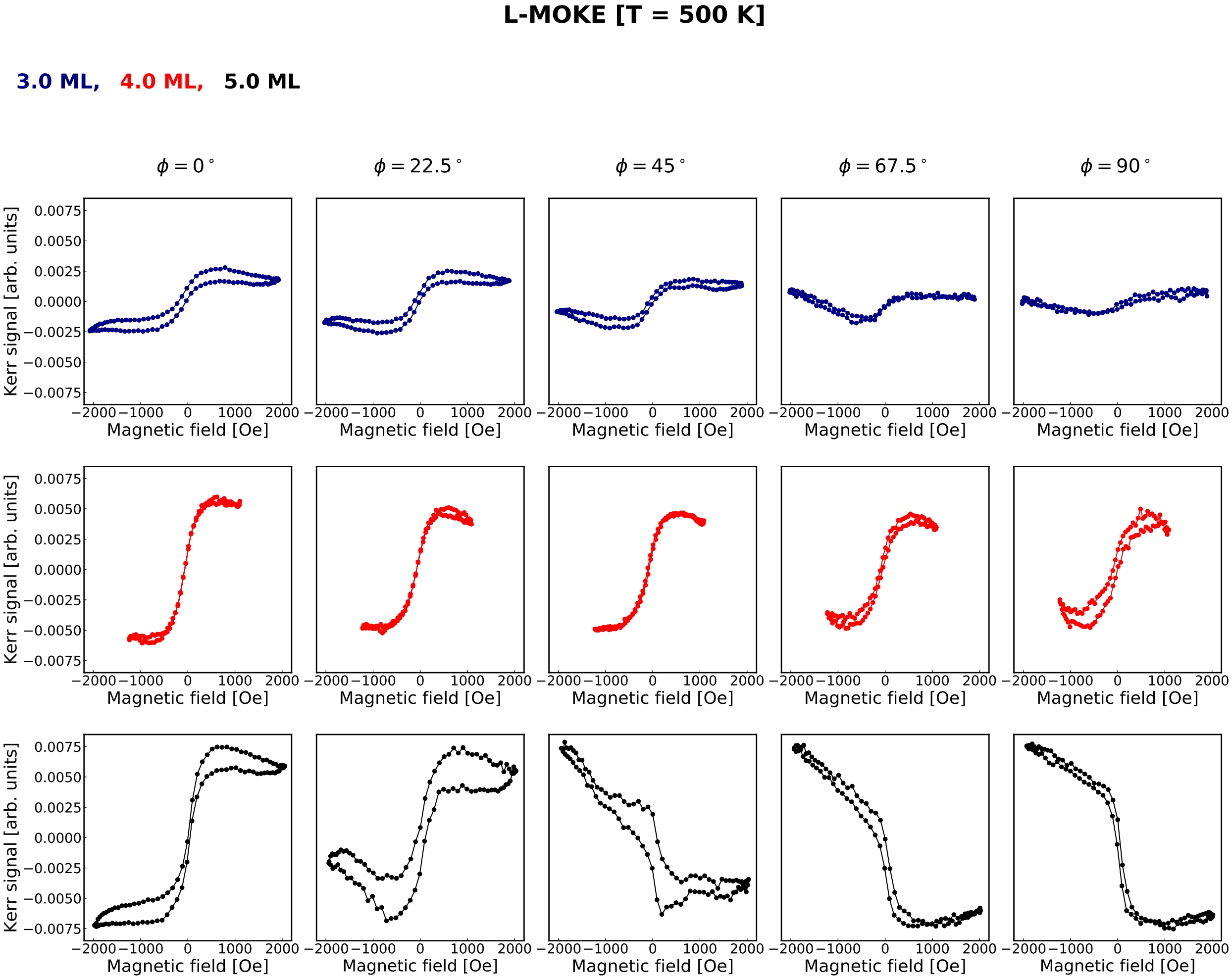

Figure 4.12—MOKE results as a function of the in-plane angle ($\phi = 0^o - 90^o$) of the applied magnetic field, for 3.0 ML (blue), 4.0 ML (red) and 5.0 ML (black) of Fe deposited on Ag(977) at 500K. Online colors

4.2 Co/Ag(977)

4.2.1 Growth morphology

Similarly to the Fe/Ag(977) system, the samples of Co/Ag(977) were grown at 300K, 400K and 500K and investigated using STM and MOKE, both measured *in-situ* and at room temperature. The STM images are shown in figures 4.13, 4.14 and 4.15.

For 0.5 ML (fig. 4.13) the grain size ranges from 3.9 nm (400 K) to 9.5 nm (500 K) and at room temperature, 5.9 nm (see Appendix C, figure C.7). For growth at 400K (see fig.4.13.b) the cobalt grains grow on top of the step edges as occurred for Fe and appear to be self-assembled and with a low size dispersion, of about 3.86±0.07 nm.

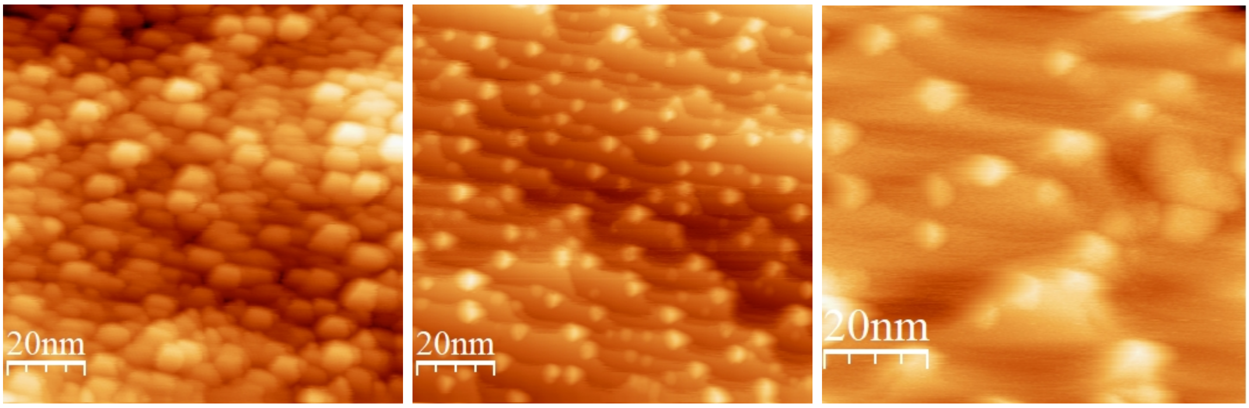

(a) 0.5 ML, $T_s = 300$ K. (b) 0.5 ML, $T_s = 400$ K. (c) 0.5 ML, $T_s = 500$ K.

Figure 4.13—STM images of 0.5 ML of Co grown on Ag(977) at different substrate temperatures (T_s).

Here, differently from the iron system, we have not observed from the STM images a very clear evidence of self-assembled Co-nanostructures, resembling nanowires or even elongated nanostructures, for thickness above 0.5 ML, at any temperature. In fact, for 2.0 ML (see fig. 4.14abc), we observe the formation of grains, whose average sizes increase with the growth temperature: starts with 6.6 nm (RT), then 8.3 nm at 400 K and reaches 9.2 nm at 500 K. At 400K the STM image shows that the nanostructures have a low size dispersion and exhibit some preferential alignment. For 3.0 ML, figure 4.14def, the average grain sizes are 10.3 nm (RT), 15.6 nm (400 K) and 17.2 nm (500 K). For the 4.0 ML thickness (figure 4.14ghi) the cobalt grain sizes are 10.3 nm (RT), 16.8 nm (400 K) and 18.2 nm (500 K). At higher temperature (500 K), both 3.0 ML and 4.0 ML samples present some triangular structures and others shapeless, which can be related to the mismatch between the cobalt (HCP) and the substrate (FCC) structures. Moreover, for 4.0 ML at 300 K (figure 4.14g) we observed the formation of connected structures without a defined shape.

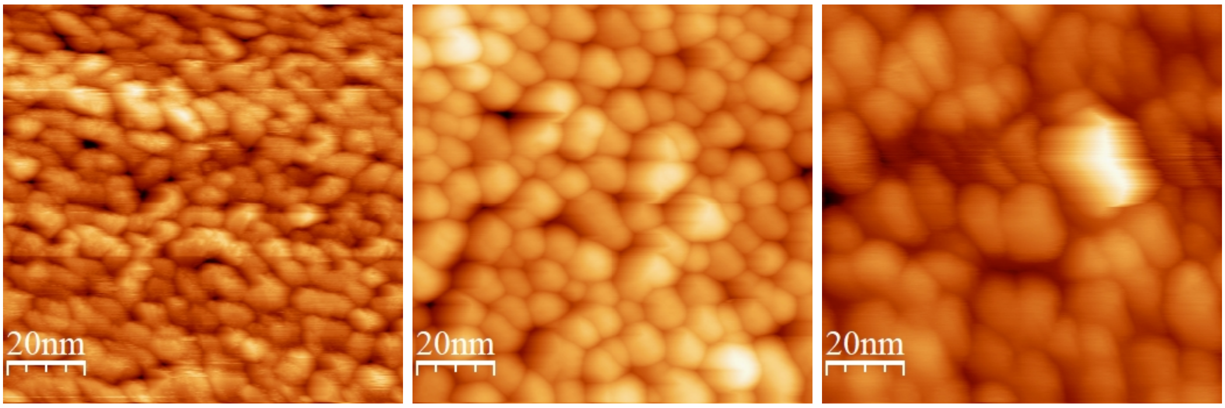

(a) 2.0 ML, $T_s = 300$ K. (b) 2.0 ML, $T_s = 400$ K. (c) 2.0 ML, $T_s = 500$ K.

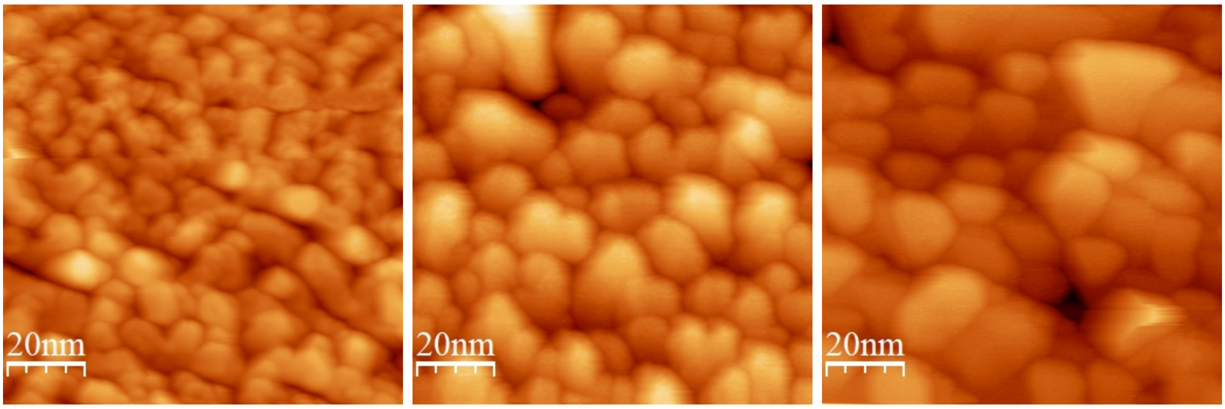

(d) 3.0ML, $T_s = 300$ K. (e) 3.0ML, $T_s = 400$ K. (f) 3.0ML, $T_s = 500$ K.

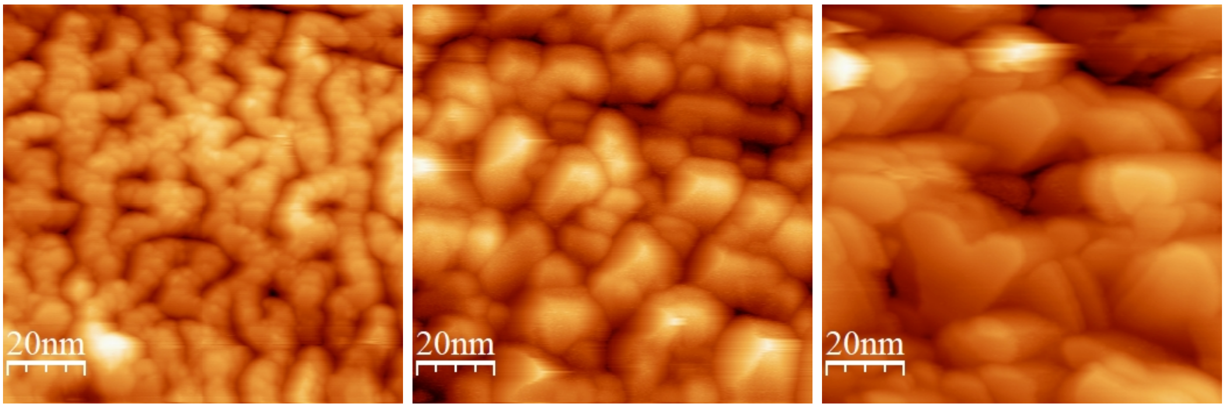

(g) 4.0ML, $T_s = 300$ K. (h) 4.0ML, $T_s = 400$ K. (i) 4.0ML, $T_s = 500$ K.

Figure 4.14—STM images for 2.0 ML, 3.0 ML and 4.0 ML of Co deposited on Ag(977) at different substrate temperatures (T_s= 300K, 400K, 500K).

For 5.0 ML of cobalt deposition, as shown in figure 4.15, the observed average grain sizes are 11.1 nm (300 K), 15.0 nm (400 K) and 27.1 nm (500 K). At 300K the growth seems to be more granular. At 400 K the growth appears to be of the Volmer-Weber type (island growth mode) with larger and interconnected islands. Moreover, at 500 K, we observed the formation of both triangular and hexagonal structures (figure 4.15c). As seen for 3.0 ML and 4.0ML (also at 500K), the triangular nanostructures should be related to stacking fault (FCC) (defect during the thin film growth on the substrate surface) growth of cobalt on Ag(111), while the hexagonal ones due to HCP symmetry commonly observed for the growth of Co islands.

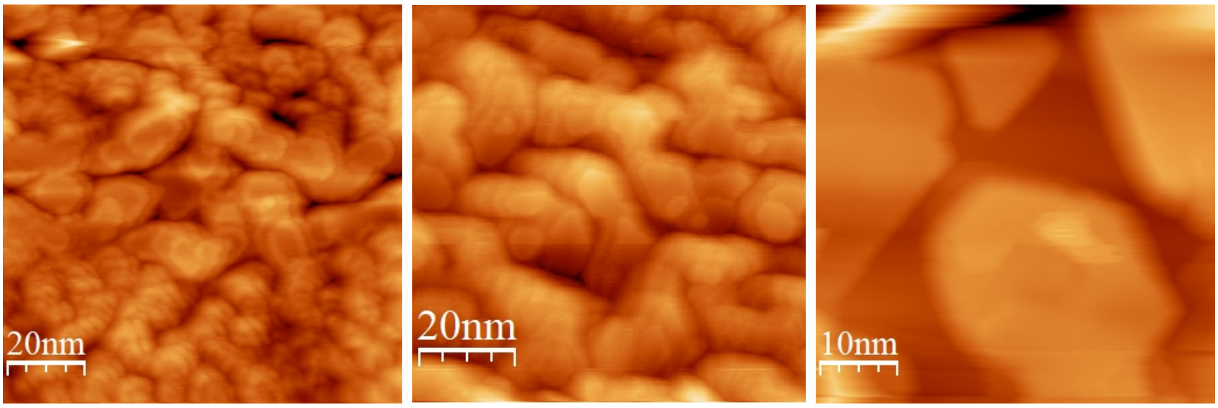

(a) 5.0ML, $T_s = 300$ K. (b) 5.0ML, $T_s = 400$ K. (c) 5.0ML, $T_s = 500$ K.

Figure 4.15—STM image of 5.0 ML of Co grown on Ag(977) at different substrate temperatures (T_s).

4.2.2 Magnetic characterization

The magnetic properties of Co/Ag(977) samples were also investigated by *in-situ* magneto-optical Kerr effect at room temperature. The MOKE measurements of 0.5 ML of Co on Ag(977) prepared at 300K, 400K and 500K did not show any ferromagnetic signal at both longitudinal (not shown) and polar (see fig. 4.16) configurations. In addition to the absence of magnetic remanence or coercive field, for all thicknesses It is not seen any indication of saturation of the Kerr signal in the P-MOKE experiments with an applied field up to 2000Oe. That, all together, indicates that when the field is applied normal to the surface plane we see a hard-axis of magnetization.

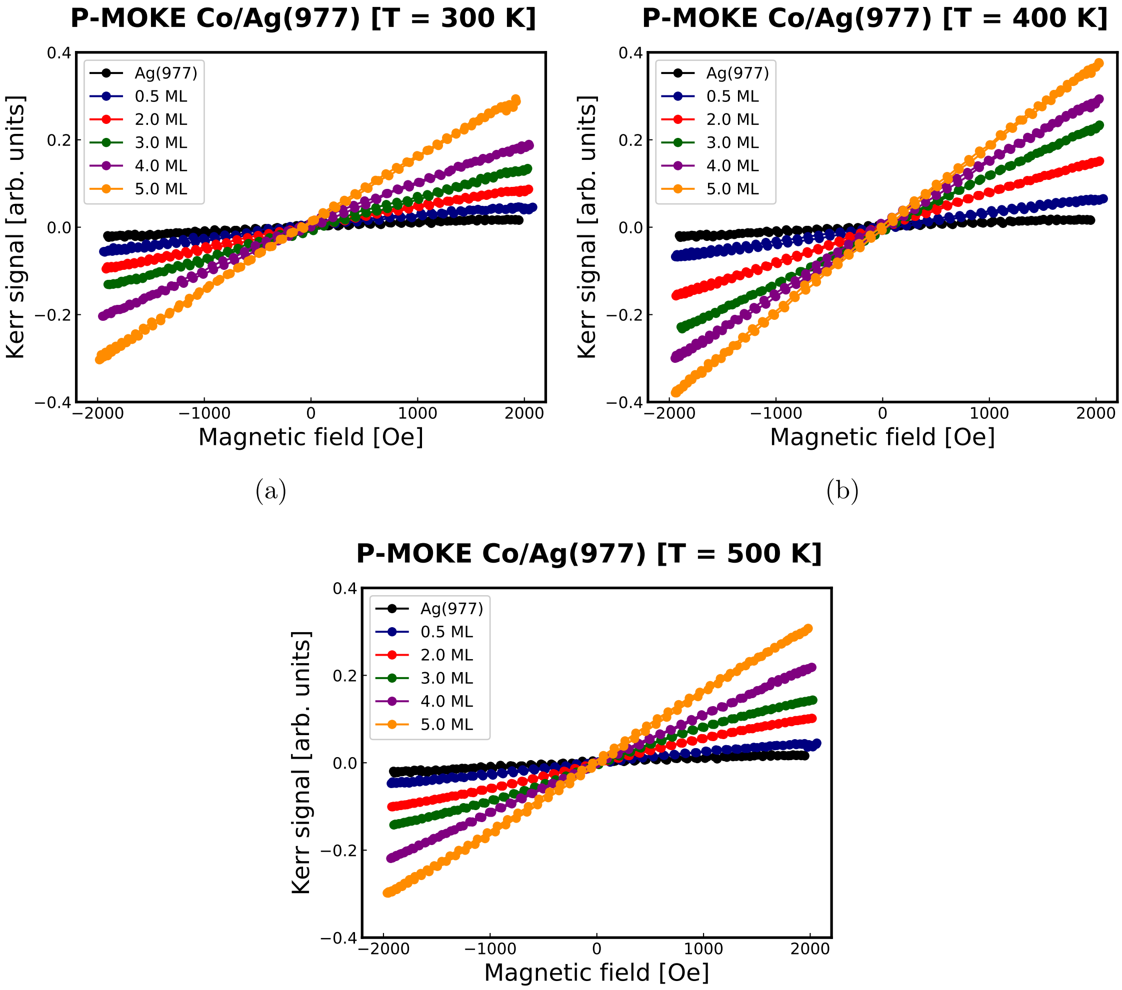

(a) (b)

(c)

Figure 4.16—Polar-MOKE results for Co/Ag(977) samples at 300 K (a), 400 K (b) and 500 K (c).

L-MOKE results for the samples with thickness in the range 2.0 ML - 5.0 ML are shown in figure 4.17. All of them show ferromagnetic character when prepared at room temperature (fig. 4.17a), and exhibit low coercive fields, indicating that the easy axis is in plane. Differently from the Fe-films, we see, already at 2.0 ML, a nice square hysteresis loop for the sample prepared at 300K. At 2.0 ML the coercive field is only $H_c = 64.6$ Oe and this value increases with thickness, up to $H_c = 240.1$ Oe (5.0 ML). For samples prepared at 400K and 500K we observe a superparamagnetic character at lower thickness (2.0 and 3.0 ML) and a more ferromagnetic one at 4.0 and 5.0 ML as shown in figures 4.17bc. At those higher preparation temperatures, the strengths of the coercive field are importantly affected, for instance at 400 K, $H_c = 6$ Oe at 3ML, $H_c = 192$ Oe at 5ML, and at 500 K, $H_c = 16$ Oe at 3ML, $H_c = 315$ Oe at 5ML.

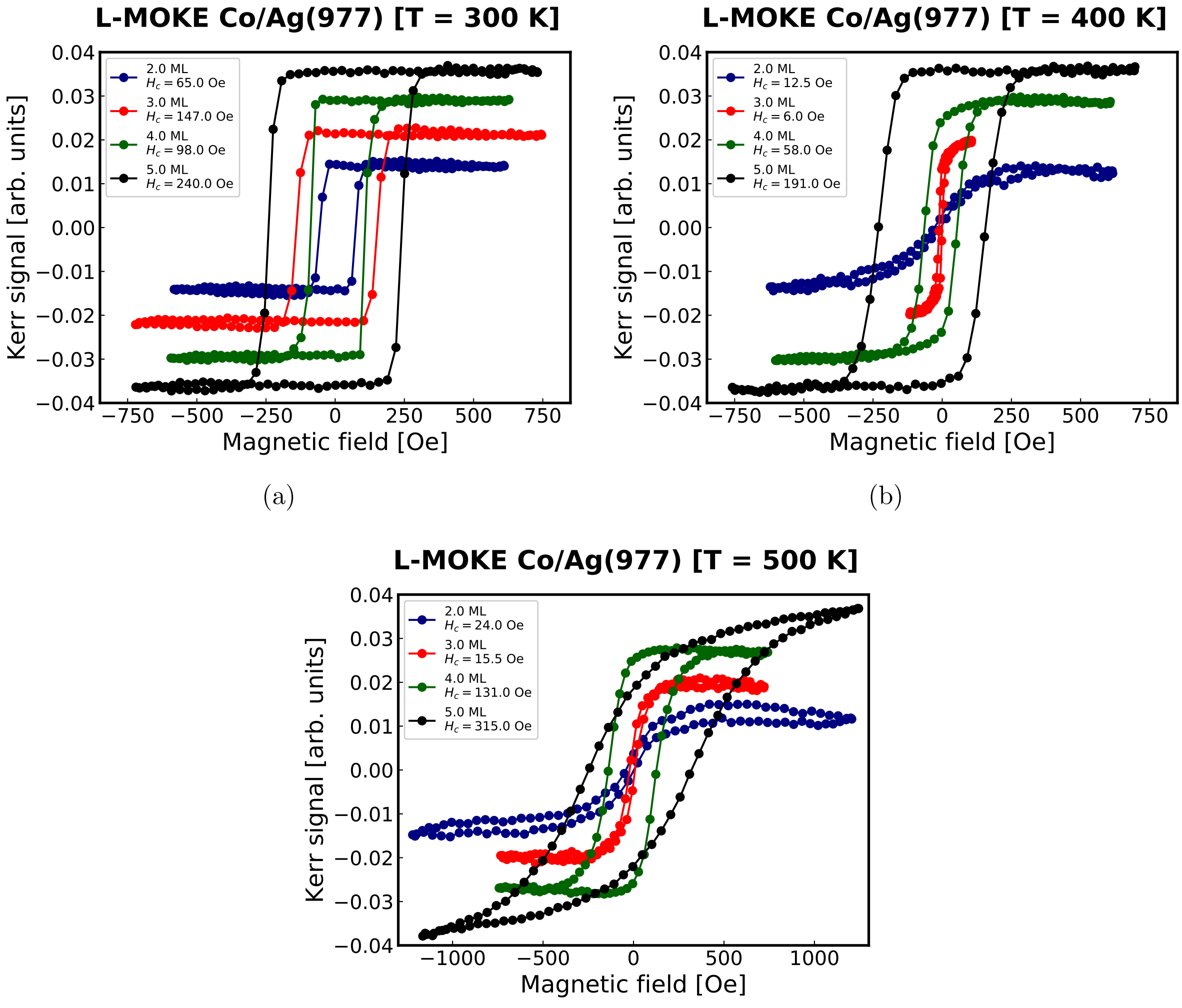

(a) (b)

(c)

Figure 4.17—L-MOKE results for Co/Ag(977) at 300 K (a), 400 K (b) and 500 K (c).

We have performed MOKE measurements rotating the applied field around the sample plane ($0° \leq \phi \leq 90°$) from L-MOKE ($\phi = 0^o$) to T-MOKE ($\phi = 90^o$) configurations. At $\phi = 0^o$ the magnetic field is being applied along the step edges direction, while at $\phi = 90^o$ perpendicular to them. The results of those measurements for samples prepared at 300K, 400K and 500K are shown in figure 4.18. The evolution of the coercive field (H_c) of the samples prepared at room temperature show the most appealing results. For 2.0 ML thickness the coercive field does not vary significantly. For 3.0 ML and 4.0 ML, H_c exhibit lower values at $\phi = 0^o$ and the highest values at $\phi = 90^o$, indicating an easy axis along the step edges and a 'harder' axis perpendicular to them. At 5.0 ML again the value of H_c does not change much, suggesting that the anisotropy is being lost at higher thickness.

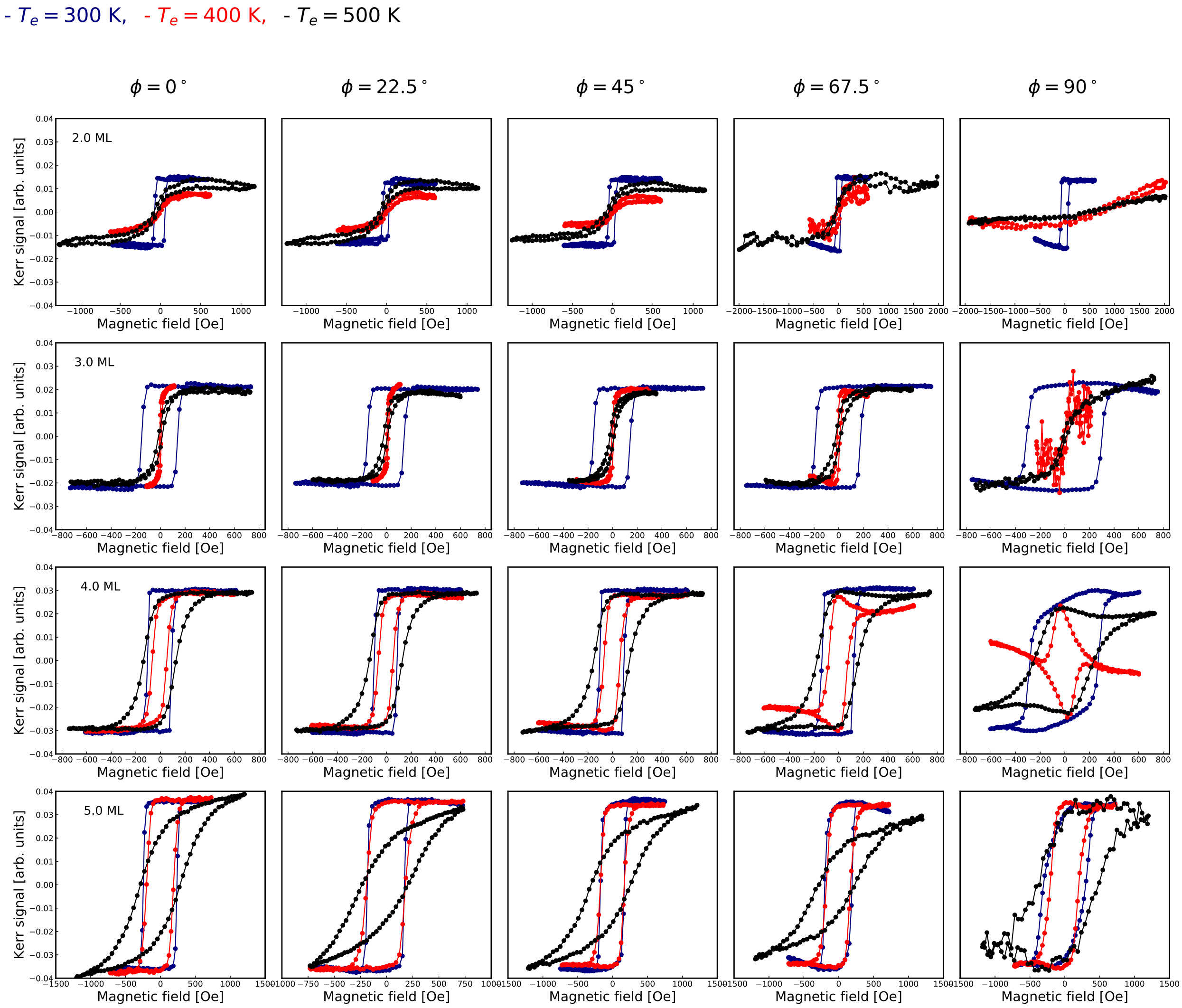

Figure 4.18—MOKE results for 2.0, 3.0, 4.0, 5.0 ML of Co on Ag(977), ϕ is the in-plane angle of the applied field ($\phi = 0^o$ corresponds to the step edge direction). Samples prepared at 300 K (blue lines), 400 K (red lines) and 500 K (black lines). Online colors.

Chapter 5

Discussion and analysis

This chapter is dedicated to examine and highlight the experimental main results and furthermore to propose physical explanations to them. The set of Fe/Ag(977) samples comprises the deposition of 0.5 ML and 1.0 ML to 5.0 ML, at 300K, 400 K and 500 K. We have prepared Co/Ag(977) samples, with thicknesses of 0.5ML, 2.0ML-5.0ML, at the same temperatures. Those samples were investigated by STM and MOKE and the most important results and the correlation between their structural and magnetic properties will be here discussed.

We have made a statistical analysis of grain size for the various preparations. We took several STM images (circa 50 images) of each evaporation and then measured their individual grain size by using the WSxM software.[80] We built histograms and then Gaussian functions were fitted according to the data. The average grain size (or simply grain size) is considered as the Gaussian peak position and the uncertainty as 1σ (68% of Gaussian area). The results are shown in figure 5.1 for Fe and Co films as a function of substrate temperature (T_s). According to our statistical analysis, for Fe/Ag(977), the grain size is in the range of (2.4 ± 0.2) nm for 0.5 ML, 500 K to (16.9 ± 2.0) nm for 5.0 ML, 500 K. For Co/Ag977, the grain size is in the range of (3.9 ± 0.4) nm for 0.5 ML, 400 K to (27.1 ± 2.7) nm for 5.0 ML, 500 K. Although the Fe and Co grain sizes are similar, it will be shown that their morphologies

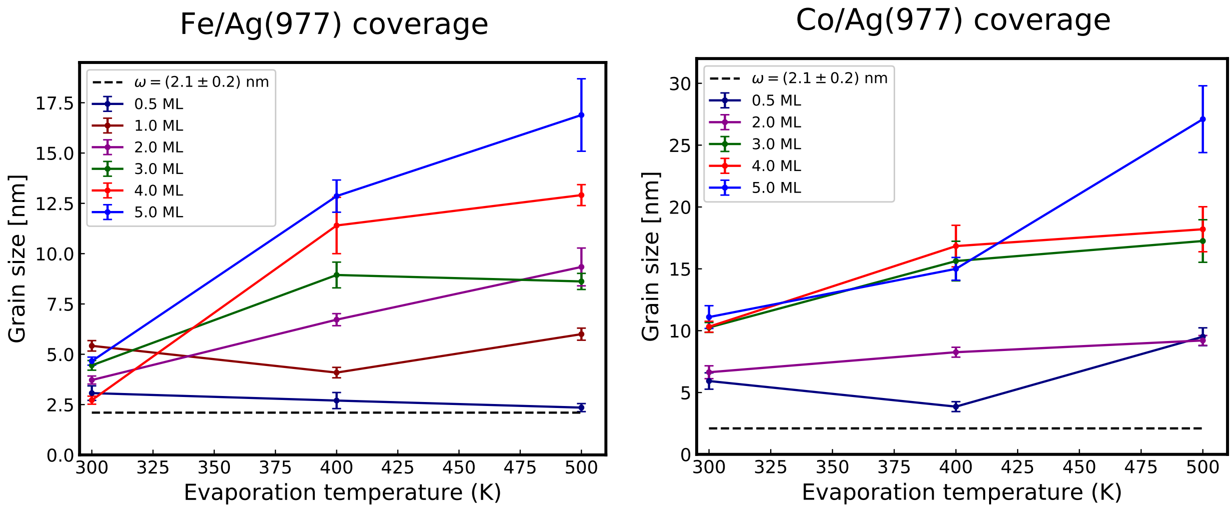

Figure 5.1—Grain size of Fe/Ag(977) (left) and Co/Ag(977) (right) as a function of evaporation temperature. The dashed line (black) represents the terrace width: $\omega = (2.1 \pm 0.2)$ nm (see section 2.1).

and assembly are quite distinct, with great impact on the magnetic properties.

For Fe/Ag(977), the STM images indicate two growth regimes: the formation of circular or elongated nanostructures and the growth of triangular platelets . For thickness above 1.0 ML, at room temperature, the STM images show the formation of structures that resemble nanowires, aligned parallel to the step edge direction as shown in detail in figure 5.2. According to our statistical analysis these self-assembled nanostructures are formed by chains and have length from (7.5 ± 0.7) nm for 4.0 ML to (14.1 ± 1.0) nm for 5.0 ML and width between (2.7 ± 0.1) nm for 4.0 ML and (4.7 ± 0.2) nm for 5.0 ML. Interestingly the nanostructure's widths for 4.0 ML and 5.0 ML correspond approximately to the width of one and two steps of Ag(977), respectively. However, since the lengths also grew proportionally, the aspect ratios (lengh/width) appear to be very similar, they are 2.8 and 3.0 for 4.0 ML and 5.0 ML, respectively.

Due to their shape, self-organization and size (both length and width), we can say that by depositing Fe at RT on the vicinal surface Ag(977) between 2.0 ML and 5.0 ML, self-assembled elongated nanostructures grow aligned along the steps. The explanation for the self-organization growth process may be attributed to the mobility of atoms and energy considerations of the stepped surface as detailed in section 2.2. At room temperature, a deposited adatom on a terrace has enough mobility to walk throughout the surface by diffusion. Once reaching the top step edge, however it will not have enough energy to overcome the Erlich-Schwöbel barrier. Several adatoms will then reach the edge step and agglutinate themselves, forming those elongated nanostructures.

The formation of self-assembled metallic nanowires on vicinal surfaces has already been reported by several authors. The growth of nanostructures that resemble wires has been observed on silver (Ag), nickel (Ni), copper (Cu), cobalt (Co), on vicinal surface Pt(997) and Au(111).[83–87] Gambardella et al. (2000)[84] studying the growth of self-assembled Co nanoparticles on Pt(977) at thickness below 3.0 ML, noticed that below 250 K, a rough growth takes place and between 250 K and 300K, a periodic array of nanowires is formed. The first observation of the formation of Fe nanowires on a vicinal surface was reported by Elmers et al. (1994)[88] by imaging them with STM on vicinal W(110) substrate at submonolayer regime. Jung et al. (1995),[89] Shen et al. (2003),[90] ViolBarbosa et al. (2009)[91] and others noticed the presence of one-dimensional structures of copper (Cu) and iron (Fe) on vicinal surfaces Mo(110), W(110) and Cu(332). Cheng et al. (2005)[92] studied the self-organization of Fe/Pt(997) with thickness under 4.0ML and at RT. In the submonolayer regime, they observed narrow nanostripes decorating the stepped surface. However, increasing the iron thickness (greater than 0.15 ML) the nanostructures were transformed into wider chains, maintaining the aspect ratio. Several previous studies of Fe epitaxially grown on Ag (either flat or vicinal) substrate pointed to a layer-by-layer growth at RT, without a remarkable ordering of the thin film. A common point among these reports is that the growth starts with the steps being decorated, then to a layer-by-layer mode, and then the growth gradually yields Fe islands at thickness greater than 4.0 - 5.0ML.[30,36,93] In the present work, however,

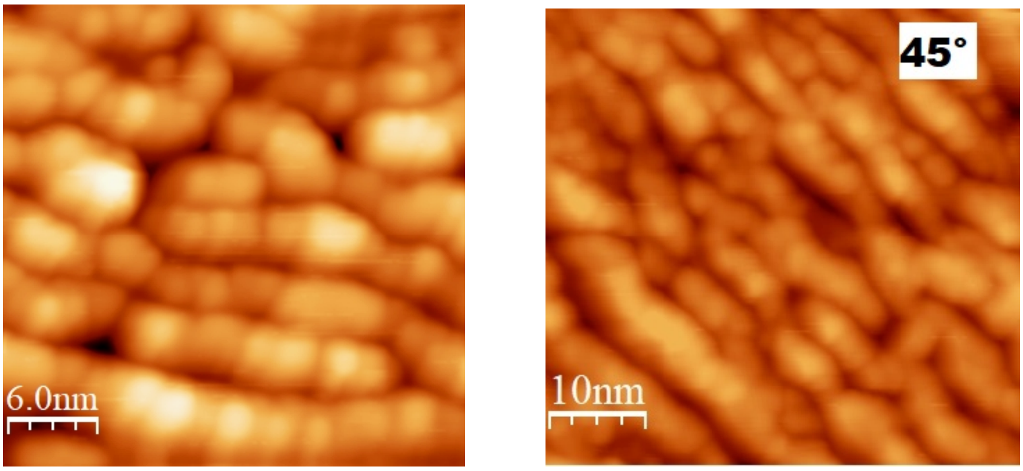

(a) 2.0ML. (b) 3.0ML.

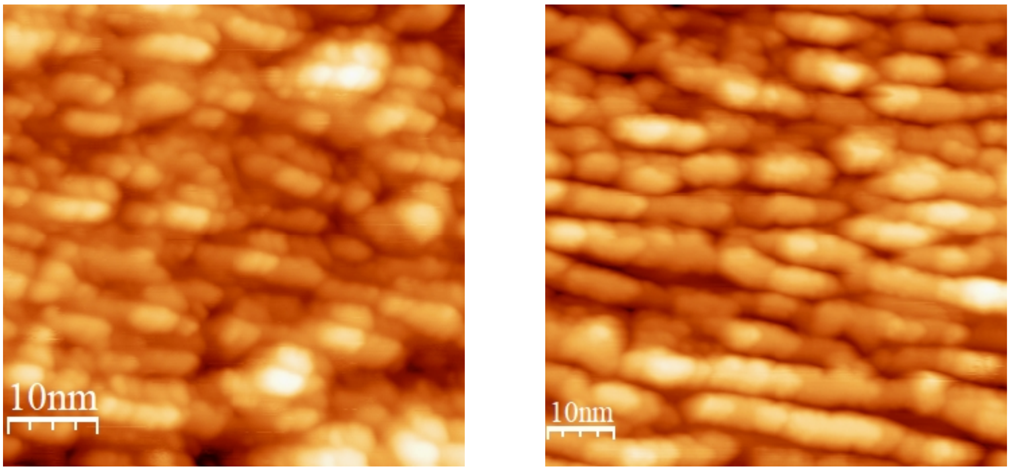

(c) 4.0ML. (d) 5.0ML.

Figure 5.2—Detailed STM Images of structures that resembles nanowires at room temperature (RT).

we see elongated Fe nanostructures, resembling nanowires, at least up to 5.0 ML of thickness at room temperature.

The other kind of growth observed for Fe/Ag(977) was the formation of triangular platelets on the top of steps, between 1.0 ML and 3.0 ML, at $T_e = 500$ K (see figure 4.3cfi). At 1.0 ML we observed the coexistence of nanodots and serrated edges. For thickness of 2.0 ML and 3.0 ML, the STM images show triangular platelets with average size of 9.3 nm (2.0 ML) and 8.6 nm (3.0 ML) randomly spread throughout the substrate. This behavior was noticed before in others investigations on the growth of Fe and Co on vicinal and flat surfaces.[29, 94–96] In figure 5.3, we compare STM images of triangular platelets of two other studies with this work.

Rohart et al. (2008)[94] studied the Fe/Au(788) system in the range of 45 K to 430 K, observed the formation of triangular shaped structures and concluded that a Fe-Au superficial

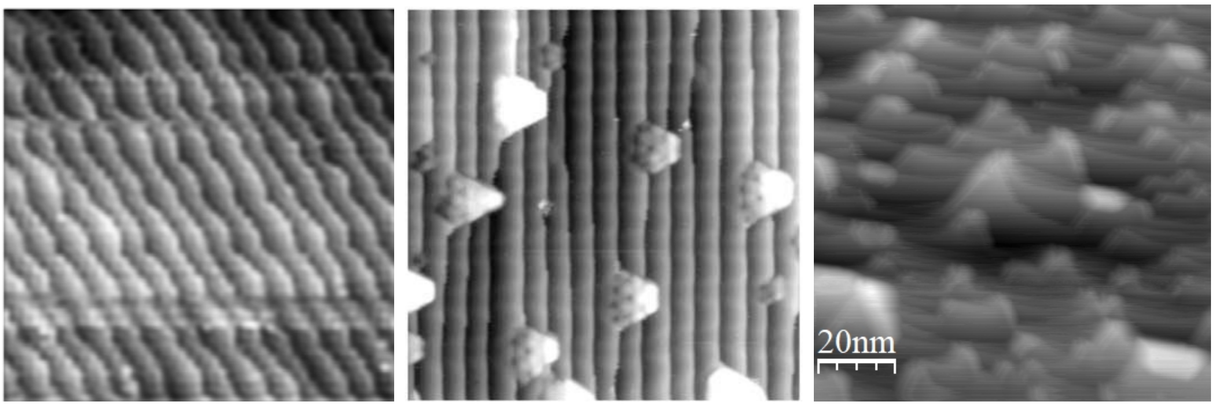

(a) Fe/Au(788) at 430 K and 0.3 ML. Rohart et al. (2008).[94]
(b) Co/Au(788) at 480 K and 0.4 ML. Baudot et al. (2003).[97]
(c) Fe/Ag(977) at 500 K and 2.0 ML. This work.

Figure 5.3—Comparison between growth mode of ferromagnetic nanostructures on vicinal surfaces at higher temperature. (a) Evaporation of Fe/Au(788) at 430 K with structures that resemble triangular platelets. (b) Co/Au(788) at 480 K and (c) Fe/Ag(977) at 500 K.

alloy was formed due to the high step densities. Baudot et al. (2003)[97] reported Co triangular platelets on Au(788) and explained their presence as due to the coalescence of nanoparticles at the surface. Li et al. (2000)[98] demonstrated in a experimental and theoretical study, the formation of one monolayer-thick islands ('quantum platelets') of finite dimensions, which are parallel aligned to the stepped substrate. Others similar cases have been observed and the explanations converge to a hybridization of ferromagnetic atoms with the vicinal surface due to a high mobility of the atoms at higher temperature. The formation of a surface alloy between the thin film and the substrate depends both on the miscibility of the elements and of course, on the growth temperature.

For Co/Ag(977), self-assembled nanowires have not been detected at any evaporation temperature. However, at 500K and between 3-5ML we have observed the formation of triangular shaped structures. Differently from the triangular platelets observed for the iron growth, where those structures are restricted to the lower thickness, in the case of Co these structures keep growing up to 5ML (see figures 4.14 and 4.15). In other words, the growth appears to be of the 'island type' instead of 'layer-by-layer', i.e., the cobalt particles prefer to grown on top of a structure previously formed, rather coalescing with the surface, increasing the height of the islands instead of their size. For the thickest film (5.0 ML, 500 K) we observe the growth of both triangular and hexagonal islands, as shown in figure 4.15c. The triangular ones most probably are due to the occurrence of fcc stacking faults, rather than the intrinsic hcp stacking of Co. The 13% mismatch of the Co lattice as compared to the Ag(111) substrate may also stimulate island formation.[99] The effect of surface alloying is beyond the scope of this work, but its occurrence cannot be ruled out. From our statistical analysis we have established that the triangular islands have a thickness in the order of 2.4 ML, reinforcing the hypothesis of stacking faults - they are more likely to occur at low thickness imitating the substrate. The hexagonal structures are thicker, with an average height of 4.9 ML. This behavior has already been observed for thin Co-film at high temperature.[100,101] In figure 5.4 it is compared the structures we have observed in this work with others studies. Wasniowska et al. (2008)[101] investigated Co/Pd(111) and observed similar structures during epitaxial growth and related their format to the Schwöbel Barrier.

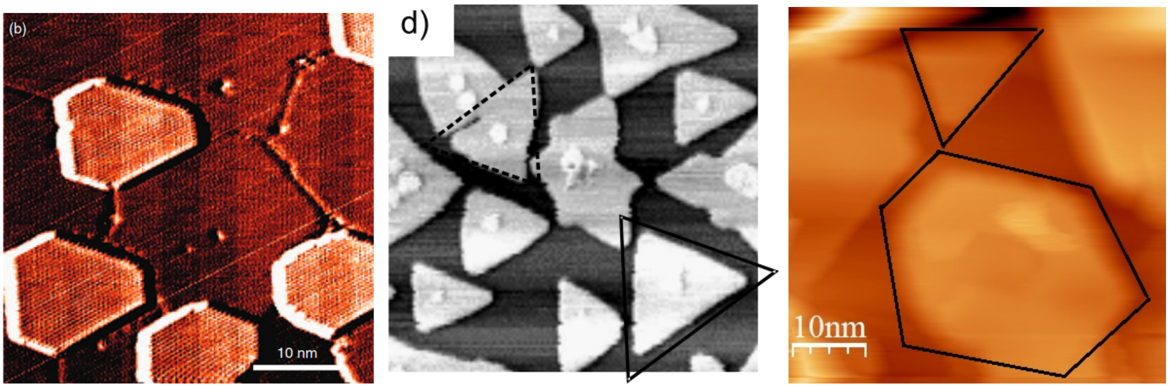

(a) 0.35 ML Co/AgGe. (b) 0.6 ML Co/Pd(111). (c) 5.0 ML, Co/Ag(977).

Figure 5.4—Comparison between the structures obtained in other studies and in this work. (a) shows the hexagonal packing of Co on AgGe with thickness of 0.35 ML at 800 K. Extracted from Lin et al. (2010);[100] (b) shows the study of 0.6 ML of Co/Pd(111) at 500 K. Extracted from Wasniowska et al. (2008)[101] and (c) image obtained in this work.

From here on, we will discuss the most relevant magnetic results of Fe and Co on Ag(977) and correlate them with the structural analysis done before. In our experiments, no ferromagnetic signature was seen at thickness below 3.0 ML for Fe/Ag(977), and below 2.0 ML for Co/Ag(977), in both longitudinal and polar configurations.

At room temperature the 3.0 to 5.0 ML Fe/Ag(977) samples show nice square loops in the L-MOKE configuration and by rotating the external field in the substrate's plane ($0° \leq \phi \leq 90°$) we observe a strong dependence of the coercive field (H_c) with respect to ϕ - see fig. 4.10. From those results we have determined H_c as a function of ϕ as shown in figure 5.5 in polar representation. As observed in the STM images, the Fe deposition up to 5ML, produces elongated nanostructures aligned along the steps, whose axes almost coincide with the horizontal direction ($\phi = 0^o$). For the three samples (3.0, 4.0, 5.0 ML) we see an easy axis and a hard axis for $\phi = 0^o$ and $\phi = 90^o$, respectively. This is a clear evidence of uniaxial anisotropy determined by those elongated nanostructures. Another very interesting point, is that the coercive field increases substantially, as the thickness increases. At the easy axis ($\phi = 0^o$), H_c is only 3.8 Oe for the 3.0 ML sample, increases to 10.2 Oe for 4.0ML, and to 129.0 Oe for 5.0 ML. At the hard axis ($\phi = 90^o$) the values are 11.8 Oe, 104.7 Oe, and 621.8 Oe for 3.0 ML, 4.0 ML, and 5.0 ML, respectively. The coercive fields are known to to be strongly dependent on the size and shape of nanomagnets. Here, the increase in the coercive field may be related to the increase in the volume of the magnetic nanostructures, and also being influenced by dipolar interactions between them.

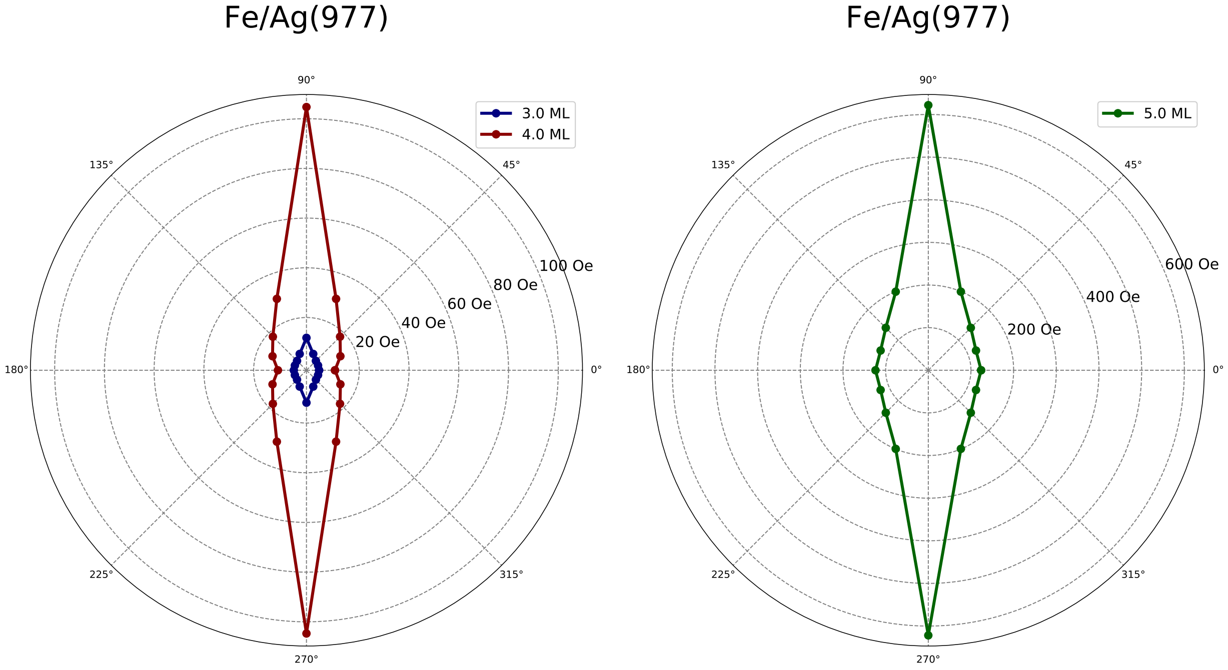

Figure 5.5—Polar representation of the coercive field H_c as a function of ϕ for 3.0 ML, 4.0 ML and 5.0ML of Fe on Ag(977) at 300K.

For the Co/Ag(977) samples we have obtained L-MOKE ferromagnetic hysteresis for all evaporation temperatures (300K, 400K, 500K) from 2.0 ML to 5.0 ML of Co deposition as shown in figure 4.17. From the angular dependent MOKE results (figure 4.18) the coercive field (H_c) as a function of ϕ has been represented in figure 5.6. Here again the increase of H_c with thickness is expected, because the addition of magnetic material increases the volume of the magnetic domains.

However, in the case of Fe/Ag(977) we have observed a very large increase of H_c at the higher thickness, while for Co/Ag(977) it is not so abrupt. A possible explanation is that at 5.0 ML of Fe an additional magnetic anisotropy term raised caused by the mechanical strain between the film and the surface (magnetoelastic anisotropy) increasing, therefore, the coercive field. Gumarov (2019),[102] Li (2020)[40] and others observed increase of the coercive field in the system composed by iron thin films at room temperature and related it with the rise of the magnetoelastic anisotropy. Nevertheless, further studies will be necessary to establish the magnetisation dynamics of this behavior, including intermediate and higher thickness.

A common point in both systems, Fe/Ag(977) and Co/Ag(977), is that the coercive field increases with increasing ϕ from 0^o to 90^o, which means the magnetic anisotropy is of uniaxial

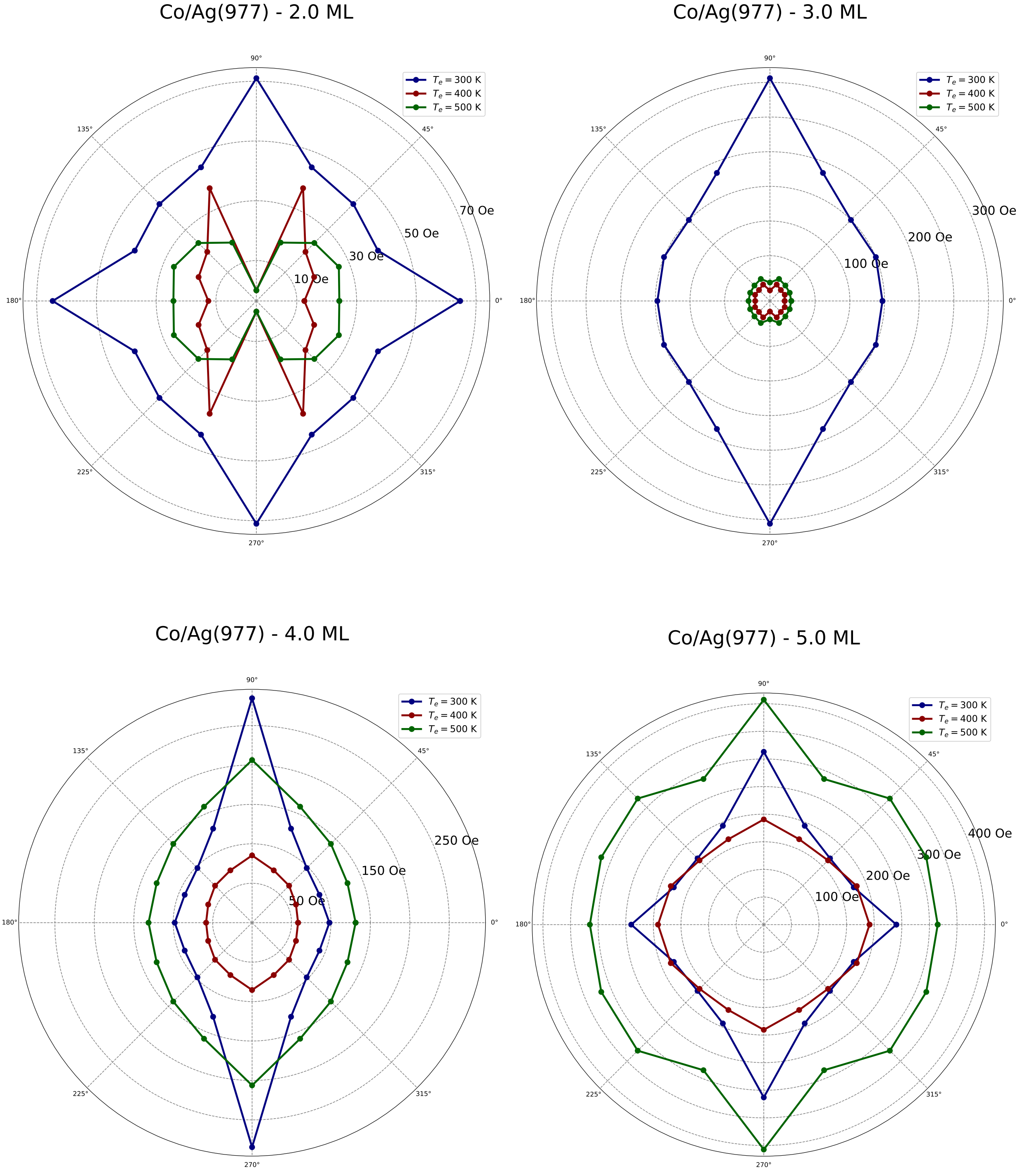

Figure 5.6—Polar representation of the coercive field H_c as a function of ϕ for 2.0 ML, 3.0 ML, 4.0 ML and 5.0ML of Co on Ag(977) at 300K, 400K, 500K.

character. So let's take the case of a magnetic particle with uniaxial anisotropy, which has only one easy axis, as shown in figure 5.7. The energy of this system without any external magnetic field can be represented by $E = K_u V\, sin^2\, \phi$, where K_u is the anisotropic constant and ϕ is an angle from the easy axis of the material. When an external magnetic field H is applied at an angle α (related to easy axis), the energy of the system will be given by $E = E_{anisotropic} + E_{magnetostatic}$, i.e., $E = K_u\, sin^2\, (\phi) + M_s H\, cos\, (\alpha - \phi)$,[103] where M_s is the saturation magnetization. In case the anisotropic energy is the strongest term, then in this situation, the minimum of energy is achieved when $\phi = \pm n\pi$ $(\partial E/\partial\phi = 0)$ and the coercive field will be given by $H_c = 2K_u/M_s$ $(\partial^2 E/\partial\phi^2 = 0$, at $\phi = 0°)$. Therefore, by increasing the applied field angle α (with respect to the easy axis), the anisotropic energy gets larger and it will be more difficult to switch the magnetization of the system, raising the coercive field, as experimentally verified.

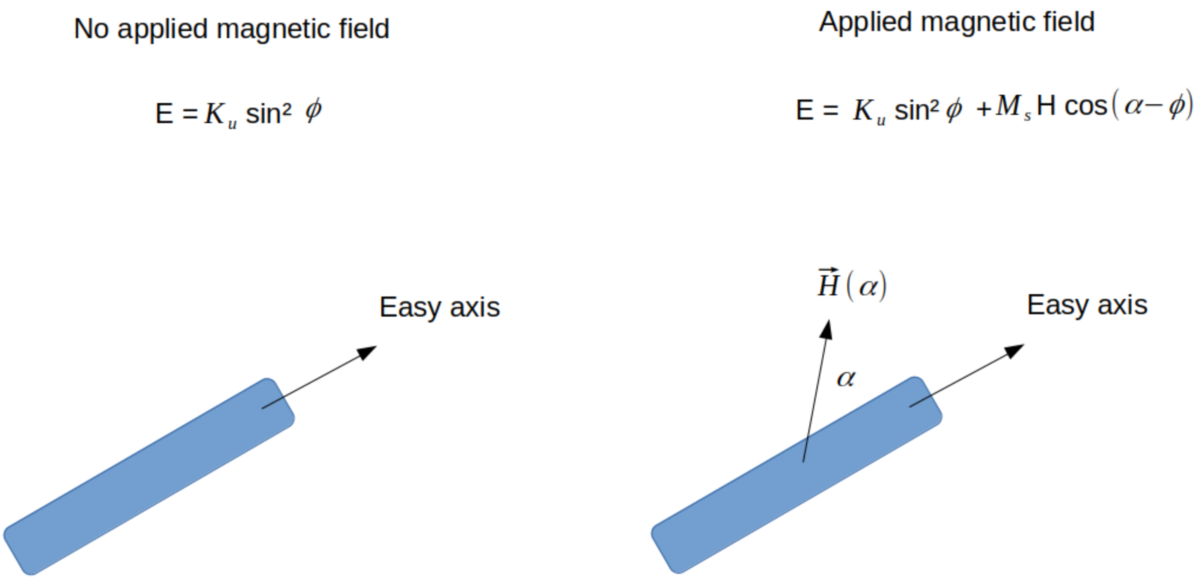

Figure 5.7—Left side: Energy of a particle with uniaxial anisotropy, $E(\phi) = K_u sin^2\phi$, where the easy axis direction is the angle $\phi = 0°$; Right side: By applying a magnetic field $\vec{H}(\alpha)$ the magnetostatic energy term, $M_s H cos\, (\alpha - \phi)$, is added.

As shown by the MOKE measurements it has been observed that for both systems the easy axis lies along the step edges $(\phi = 0°)$, being set by the growth morphology on top of the stepped Ag(977) surface. When a magnetic field is applied in plane, but perpendicularly to the steps a 'harder' axis is observed, since the coercive field increases. Here, the meaning of 'harder axis' is related to the increasing of the external magnetic field needed to reach the saturation magnetization M_s (definition) and an expressive increase of the coercive field H_c, which is due to the anisotropic features of those structures.

Moreover, it is possible to go beyond and establish the contribution of each normalized in-plane (m_x, m_y) and out-plane (m_z) magnetization from the set of L-MOKE and P-MOKE measurements. According to our setup configuration, see figure 3.7, $\hat{y}$ is along the step edges (easy axis), $\hat{x}$ is in plane and perpendicular to the steps and $\hat{z}$ is perpendicular to the surface plane. Therefore, by using the measured intensities, $I^{0,90}_{\omega,2\omega}(H)$, and applying them to the Kerr magnetometry method (see section 3.4), we have determined the contributions m_y and m_z for cobalt samples. The results for 2.0 ML and 5.0 ML are shown in figure 5.8, and the complete analysis in Appendix D. First, those results show clearly - again - that the easy axis is in the $\hat{y}$ direction. Second, we see that the hard axis ($\hat{z}$) becomes even harder as the film gets thicker (the anisotropy increases with thickness), from 3.0 to 5.0 ML we see that the slope of m_z decreases. And third, we observe that the Kerr intensity (I/I_0) scales nicely with the thickness of the film, as expected.

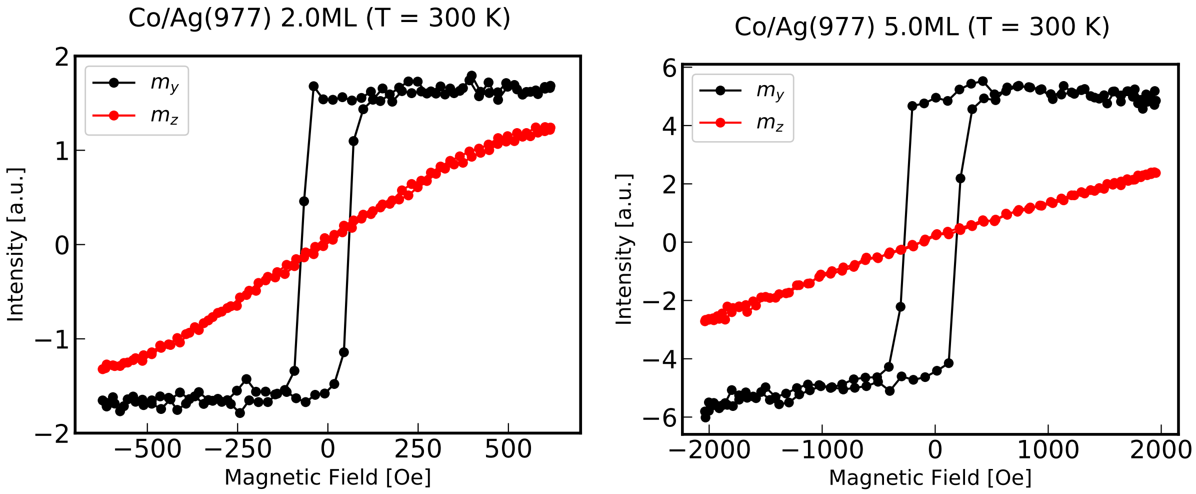

Figure 5.8—m_y and m_z contributions for 2.0 ML and 5.0 ML of Co on Ag(977).

Chapter 6

Conclusions

In this work we studied the structural and magnetic properties of Fe and Co ferromagnetic ultra-thin films grown on stepped surface Ag(977), and investigated the influence of the temperature during deposition and of the coverage. We have prepared samples in the range from 0.5 ML to 5.0 ML and at three evaporation temperatures (300K, 400 K, 500 K) in ultra-high vacuum environment. By means of *in-situ* experimental techniques, namely STM and MOKE, we have pursued to understand the correlation between growth morphology and the magnetic response of the two systems, Fe/Ag(977) and Co/Ag(977). The main results of the present work can be summarized as follows:

- For Fe/Ag(977) at thickness of 0.5 ML and 1.0 ML, the STM images show that the iron nanostructures are self-assembled along the step edges of the vicinal surface, with an average grain size ranging from 2.3 nm (0.5 ML, 500 K) to 6.0 nm (1.0 ML, 500 K). Between 2.0 ML and 5.0 ML, at room temperature, the STM images show the formation of self-assembled chains that resemble nanowires, which are aligned with the step direction. These ‘nanowires’ have different lengths, varying from 7.5 nm (4.0 ML) to 14.1 nm (5.0 ML) and widths from 2.7 nm (4.0 ML) to 4.7 nm (5.0 ML). At 500 K, between 1.0 ML and 3.0 ML, the surface shows triangular platelets, which may indicate alloy formation from atom intermixing of the film and substrate;

- The STM images of Co/Ag(977) did not show elongated nanostructures, differently from the iron system. Meanwhile, at 500 K and between 3.0 ML and 4.0 ML throughout the surface are observed triangular structures, which are attributed to FCC stacking fault of Co (rather than HCP). At 5.0 ML the STM images show both triangular and hexagonal structures (due to top of view of the hexagonal packing of cobalt - HCP);

- For Fe/Ag(977) the MOKE results show hysteresis loops between 3.0 ML and 5.0 ML, at room temperature. The coercive field goes from $H_c^{3.0ML} = 3.8$ Oe to $H_c^{5.0ML} = 121.0$ Oe. Between 4.0 ML and 5.0 ML, the coercive field suffers a large increase (about 11 times) which can be related to longer and wider nanostructures, which increase the anisotropic energy. At higher preparation temperatures, the MOKE measurements show distorted curves which we attribute to several contributions: ferromagnetism of thin film, diamagnetism of substrate and superparamagnetism of small particles. For all Fe/Ag(977) samples the easy axis remains in-plane and the hard axis out-plane;

- For Co/Ag(977) at all temperatures we have observed a ferromagnetic signal (stronger than the diamagnetism of the substrate) at thickness between 2.0 ML and 5.0 ML.

> Using Kerr magnetometry the m_y and m_z components were determined from a complete set of measurements, and the results have shown that the easy axis remains in-plane, whereas the hard axis stays out-plane, for all Co/Ag(977) samples.

With the results and analysis presented in this work, we hope to have contributed to get a better understanding about the structural and magnetic properties of ultra-thin Fe and Co deposited on Ag(977). However, some questions raised during the analysis remain without a clear response. For instance, which is the influence of Fe-Ag and Co-Ag alloying, which may modify the magnetocrystalline anisotropy as well as the stacking faults, for samples prepared at higher temperatures (400K, 500K). Moreover, it would be very interesting to investigate higher thickness and the effect on the anisotropy on the coercive field and on its angular dependence.

Appendix A

Magnetization and Brillouin function

As previously described, the magnetization $\mathbf{M}$ is a purely quantum mechanics effect. The interaction between the external magnetic field $\mathbf{H}$ and the atomic spin momentum can be described by the magnetic hamiltonian of a ferromagnetic system (see section 2.3)

$$\mathcal{H}_{magnetic} = \frac{g_J \mu_B}{\hbar} \sum_i [\mathbf{B}_{mf} + \mathbf{H}] \cdot \mathbf{S}_i = \frac{g_J \mu_B}{\hbar} \sum_i \mathbf{B}_T \cdot \mathbf{S}_i, \tag{A.0.1}$$

where $\mathbf{B}_{mf}$, $\mathbf{H}$ are the molecular and external fields, $\mathbf{S}$ is the spin angular moment and $\vec{\mu}_i = \mu_B \sqrt{J(J+1)} = \mu_B \mathbf{S}_i / \hbar$, where $J = L + S$. The expectation value of energy considering this hamiltonian (equation A.0.1) is

$$E_J = g_J m_J \mu_B B_T, \tag{A.0.2}$$

and m_J can assume values $m_J = -J, -J+1, ..., J-1, J$. The magnetization M can be represented as

$$M = \frac{N}{V} \langle m_J \rangle = n g_J \mu_B \langle m_J \rangle, \tag{A.0.3}$$

where N is the total number of atoms in a volume V. At saturation magnetization M_S, we have $\langle m_J \rangle = J$ and $M_s = n g_J \mu_B J$. As the magnetization is a thermodynamic variable, at thermal equilibrium the average magnetization by site, m_J, can be calculated from the canonical representation. Being $\epsilon = g_J m_J \mu_B B_T$, the partition function is

$$Z = \sum exp(\epsilon / k_B T) = \sum_{m_J = -J}^{J} exp(m_J g_J \mu_B B_T / k_B T) = \sum_{m_J = -J}^{J} e^{x m_J}, \tag{A.0.4}$$

where $x = g_J \mu_B B_T / k_B T$. Expanding the partition function,

$$Z = \sum_{m_J = -J}^{J} e^{x m_J} = e^{-Jx} \left(1 + e^{x} + e^{2x} + ... + e^{(2J-1)x} + e^{2Jx}\right), \tag{A.0.5}$$

setting $b = e^{-Jx}$ and $t = e^{x}$,

$$Z = b(1 + t + t^2 + ... + t^2 J) = b + bt + bt^2 + ... + bt^{(2J+1)-1} = \sum_{p=1}^{2J+1} bt^{p-1}, \tag{A.0.6}$$

rescuing the sum of geometrical series $\sum_{k=0}^{n} ar^k = a\left(\frac{1-r^{n+1}}{1-r}\right)$,

$$Z = b\frac{1-t^{2J+1}}{1-t}, \tag{A.0.7}$$

$$Z = e^{-Jx}\frac{1-e^{(2J+1)x}}{1-e^x} = \frac{\frac{1}{2}\left(e^{(2J+1)x/2} - e^{-(2J+1)x/2}\right)}{\frac{1}{2}\left(e^{x/2} - e^{-x/2}\right)}, \tag{A.0.8}$$

and using the trigonometric function, $sinh\; x = \frac{1}{2}(e^x - e^{-x})$,

$$Z = \frac{sinh\;((2J+1)x/2)}{sinh\;(x/2)}, \tag{A.0.9}$$

we calculate $\langle m_J \rangle$ as

$$\langle m_J \rangle = \frac{\sum m_J e^{xm_J}}{\sum e^{xm_J}} = \frac{1}{Z}\frac{\partial Z}{\partial x}. \tag{A.0.10}$$

Therefore, the magnetization M is

$$M = ng_J\mu_B \langle m_J \rangle = \frac{ng_J\mu_B}{Z}\frac{\partial Z}{\partial x}, \tag{A.0.11}$$

so

$$\frac{M}{M_s} = \frac{1}{JZ}\frac{\partial Z}{\partial x} = \frac{1}{Z}\frac{\partial Z}{\partial y}, \tag{A.0.12}$$

after some manipulation,

$$\frac{M}{M_s} = \frac{2J+1}{2J}coth\;\left[\frac{2J+1}{2J}y\right] - \frac{1}{2J}coth\;\left[\frac{y}{2J}\right], \tag{A.0.13}$$

the equation on the right side is called Brillouin function and defined as

$$B_J(y) \doteq \frac{2J+1}{2J}coth\;\left[\frac{2J+1}{2J}y\right] - \frac{1}{2J}coth\;\left[\frac{y}{2J}\right], \tag{A.0.14}$$

so that

$$\frac{M}{M_s} = B_J(y). \tag{A.0.15}$$

In figure A.1 are shown Brillouin functions for different values of the total angular moment, J. Let's do some analysis on the limits. First, for $J = \infty$, $B_\infty(y)$ can be written as a Taylor series,

$$coth\; x = \frac{1}{x} + \frac{1}{3}x + ..., \qquad x << 1, \tag{A.0.16}$$

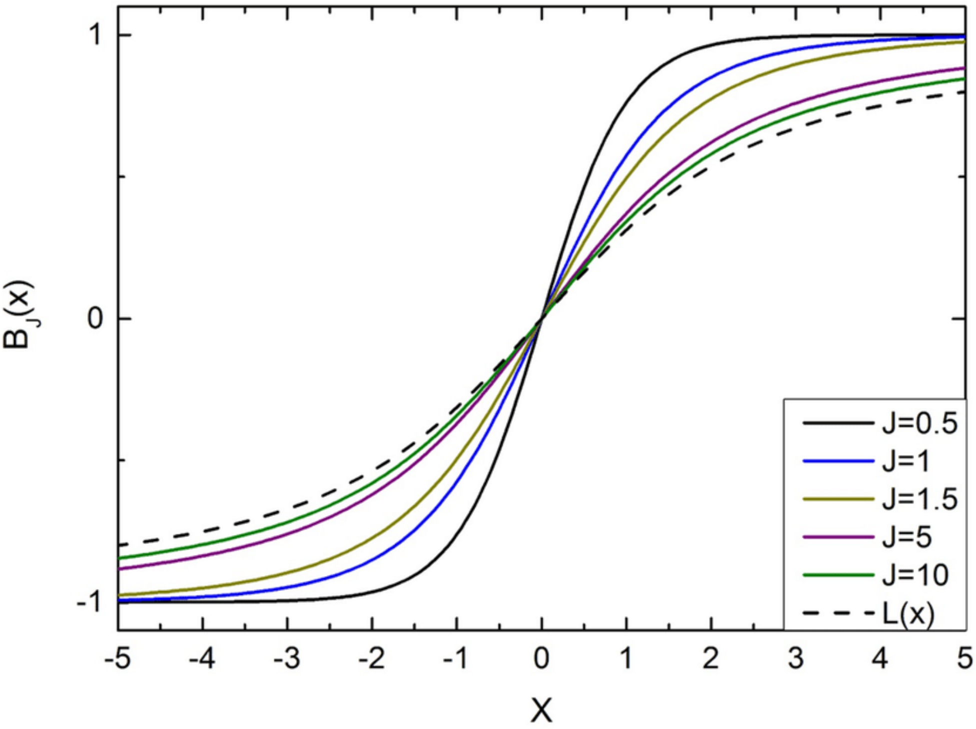

Figure A.1—Brillouin functions B_J as function of J.

$$B_J(y) = \frac{2J+1}{2J} coth \left[\frac{2J+1}{2J} y\right] - \frac{1}{2J}\left(\frac{2J}{y} + \frac{1}{3}\frac{y}{2J} + ...\right) \tag{A.0.17}$$

$$B_\infty(y) = coth\, y - \frac{1}{y} = L(y), \tag{A.0.18}$$

where $L(y)$ is named the Langevin function, representing the classical description of the system, as is shown as dashed line in figure A.1.

Appendix B

MBE calibration

This chapter is dedicated to describe the calibration procedure of the MBE growth (or evaporation) rate of Fe and Co. This information was necessary to ensure the deposition thickness of each sample prepared in this work. The epitaxial growth process has several adjustable parameters either due to the evaporator used here (SPECS, EBE-M model) or inherent of the measurement process itself: voltage, atomic flux, substrate temperature and deposition time. Our strategy was to fix all physical parameters, except one, which was varied - the evaporation time. We have set the voltage (1500 V), the atomic flux current (I_F = 3.0 nA) and the substrate temperature (T_s = 300 K). We used a clean crystal of Ni(111) as substrate, because it has a flat surface, and have prepared several samples at different deposition times, namely T = 120s, 240s, 360s and 480s, both for Fe and Co. For each sample, we took several STM images with sizes of 2000Åx2000Å, 1000Åx1000Å and 500Åx500Å . Figure B.1 shows selected images of Fe and Co on Ni(111) for different deposition times.

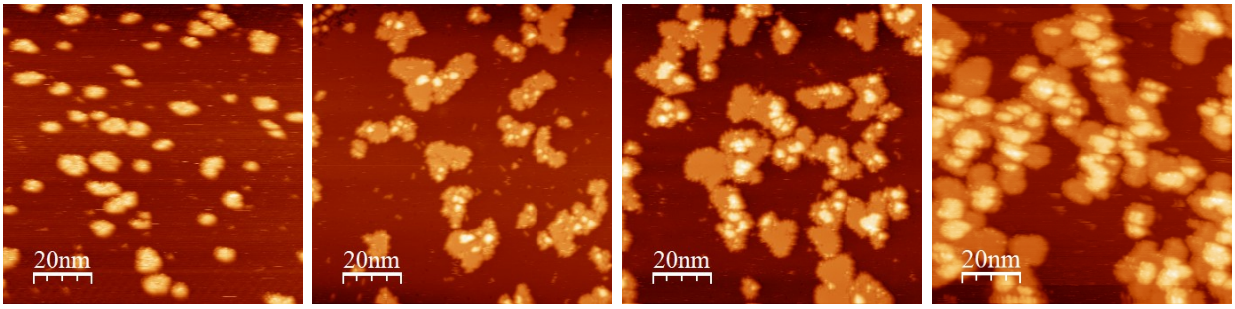

(a) 120s, Fe/Ni(111) (b) 240s, Fe/Ni(111) (c) 360s, Fe/Ni(111) (d) 480s, Fe/Ni(111)

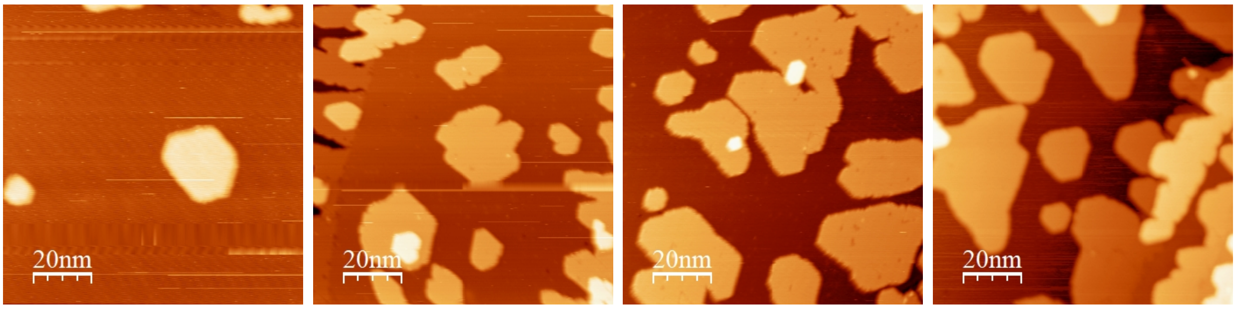

(e) 120s, Co/Ni(111) (f) 240s, Co/Ni(111) (g) 360s, Co/Ni(111) (h) 480s, Co/Ni(111)

Figure B.1—Selected STM images for evaporation times 120s, 240s, 360s, and 480, used for MBE calibration: Fe/Ni(111), (a)-(d), and Co/Ni(111), (e)-(h).

Using the WSxM software,[80] we measured the coverage (%) of each STM image, for all prepared samples. To ensure the correct coverage evaluation we have made a background correction. Then we have obtained a z profile representing the height of those structures grown on flat surface, as is shown in the figure B.2. With the z profile we could then observe the formation of each atomic layer, as is shown on the left side of figure B.2. There is a first layer at ~ 3.0 Å, and the second layer at ~ 6.0 Å. This information was then used to estimate the coverage. We programmed the software (using the option *"flooding"*) to localize all the hills of each STM images and we have (manually) excluded the background contribution, as shown in figure B.3.

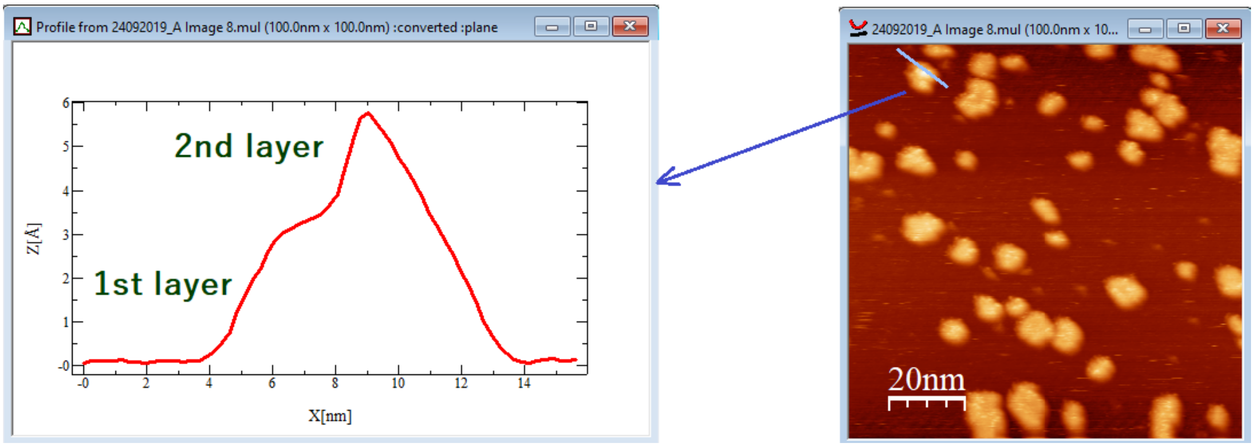

Figure B.2—Profile (left) of a nanostructure observed on a STM image (right) of a sample produced by evaporating 120s of Fe on Ni(111). For evaporation parameters see text.

For each evaporation, we built histograms representing the compendium of the measured total area for each image. Then, we have fit Gaussian curves and estimated the mean coverage and its standard deviation. The graphs representing the (Fe, Co) coverage versus evaporation time (120s, 240s, 360s and 480s) are shown in figure 3.6. Both present linear behavior, for Fe, $Coverage = (0.174\%/s)\,t$ and for Co, $Coverage = (0.166\%/s)\,t$, where t represents the evaporation time. Therefore, we concluded that a complete layer (1.0 ML) of Fe is formed at $T_{Fe} = (571 \pm 29)s$, representing $\tau_{Fe} = (1.75 \pm 0.09) \times 10^{-3}$ ML/s and for Co, $T_{Co} = (598 \pm 30)$s, with $\tau_{Co} = (1.67 \pm 0.08) \times 10^{-3}$ ML/s.

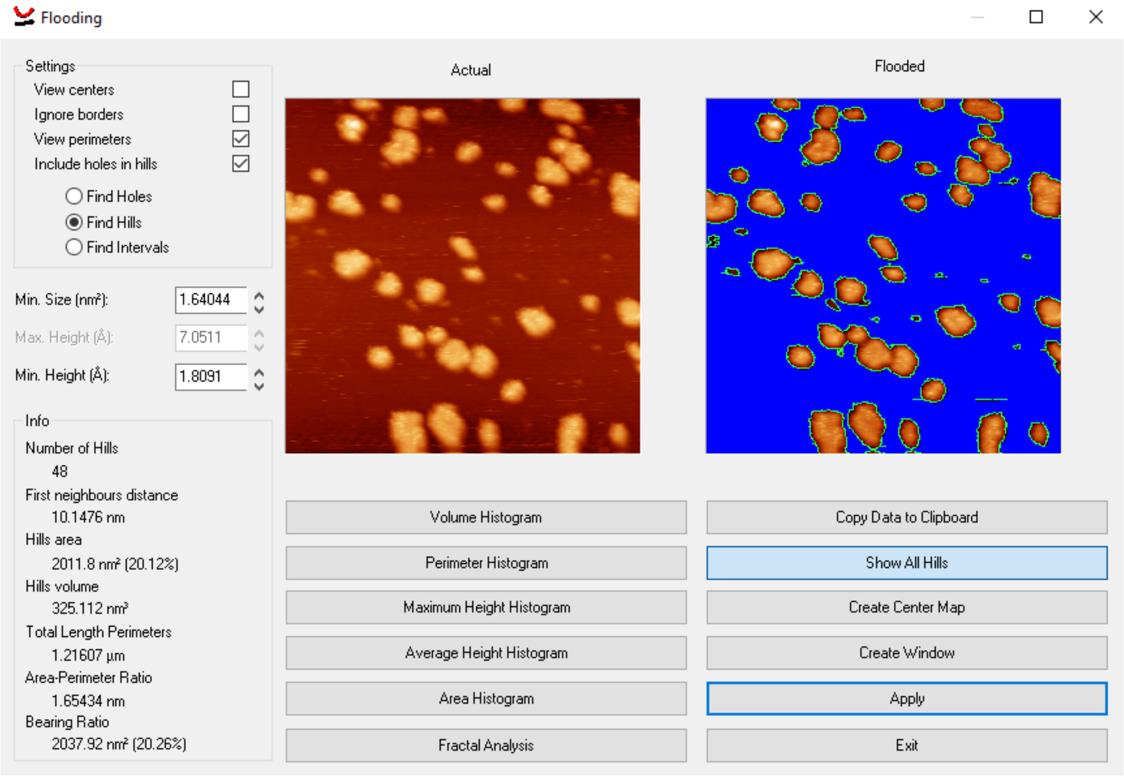

Settings
View centers ☐
Ignore borders ☐
View perimeters ☑
Include holes in hills ☑
○ Find Holes
● Find Hills
○ Find Intervals

Min. Size (nm²): 1.64044
Max. Height (Å): 7.0511
Min. Height (Å): 1.8091

Info
Number of Hills
48
First neighbours distance
10.1476 nm
Hills area
2011.8 nm² (20.12%)
Hills volume
325.112 nm³
Total Length Perimeters
1.21607 µm
Area-Perimeter Ratio
1.65434 nm
Bearing Ratio
2037.92 nm² (20.26%)

(a)

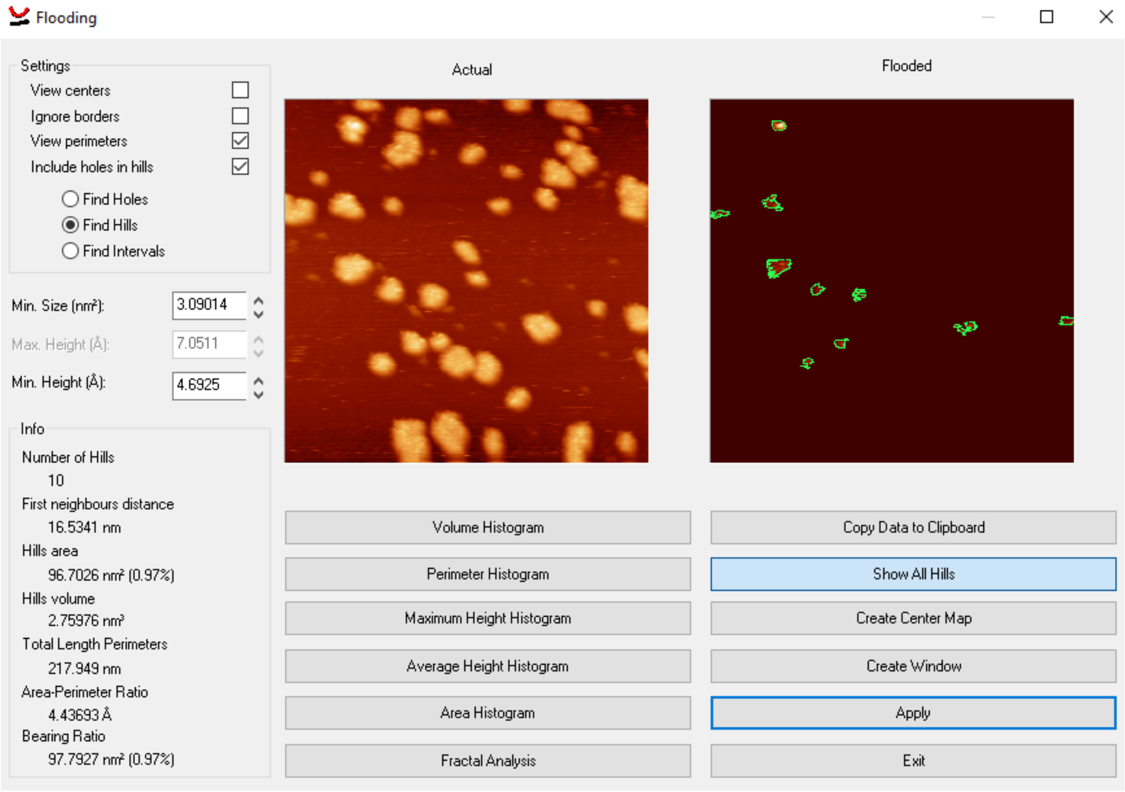

Settings
View centers ☐
Ignore borders ☐
View perimeters ☑
Include holes in hills ☑
○ Find Holes
● Find Hills
○ Find Intervals

Min. Size (nm²): 3.09014
Max. Height (Å): 7.0511
Min. Height (Å): 4.6925

Info
Number of Hills
10
First neighbours distance
16.5341 nm
Hills area
96.7026 nm² (0.97%)
Hills volume
2.75976 nm³
Total Length Perimeters
217.949 nm
Area-Perimeter Ratio
4.43693 Å
Bearing Ratio
97.7927 nm² (0.97%)

(b)

Figure B.3—Method to estimate the coverage at STM images for MBE calibration.

Appendix C

Graphics - Grain size statistic analysis

This appendix is dedicated to present the statistic analysis of the grain size based on STM images of both Fe/Ag(977) and Co/Ag(977) systems. For each deposition at specific thickness and temperature, several STM images were recorded. Using the WSxM software,[80] we have measured the size of each grain (or structure) of the images and built histograms with the data, as shown in figs. C.1, C.2 for Fe/Ag(977) and fig. C.7 for Co/Ag(977). The shape of the histograms is interpreted as the normal (Gaussian) distribution density of the structures' sizes. To establish the average size, we fitted Gaussian functions to those distributions such as

$$g(x) = \frac{1}{\sigma\sqrt{2\pi}} exp\left[-\frac{1}{2}\left(\frac{x-\bar{x}}{\sigma}\right)^2\right], \tag{C.0.1}$$

where σ is the standard deviation and $\bar{x}$ is the average value of x. Therefore, for each deposition, the grain size was took as the peak position ($\bar{x}$) and the uncertainty was considered as $\pm 1\sigma$, which corresponds to about 68.3% of the Gaussian area.

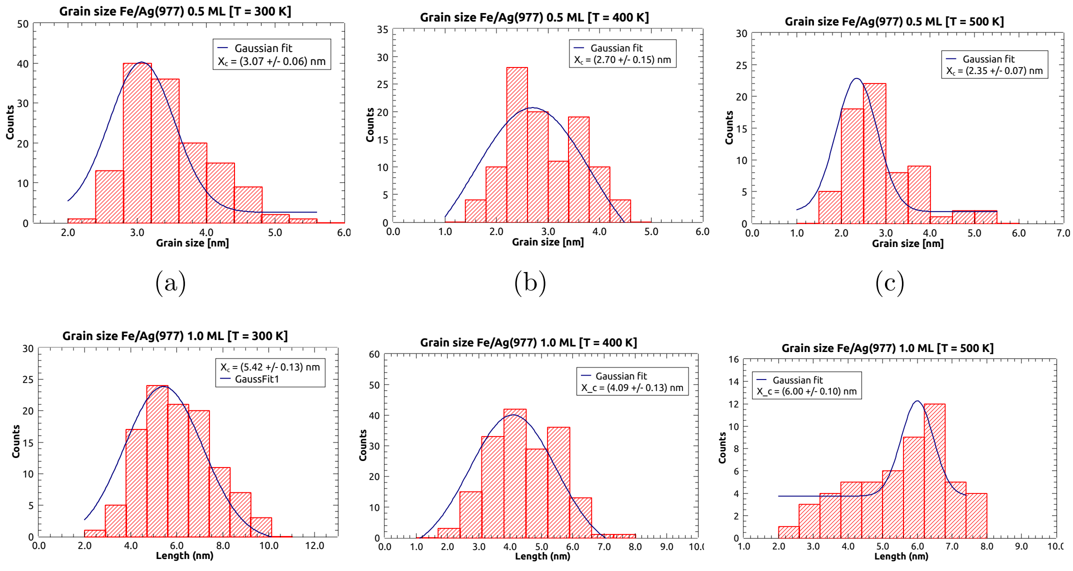

(a) (b) (c)

(d) (e) (f)

Figure C.1—Fe/Ag(977) grain size statistic analysis for thickness 0.5 ML and 1.0 ML at 300K, 400K, 500K.

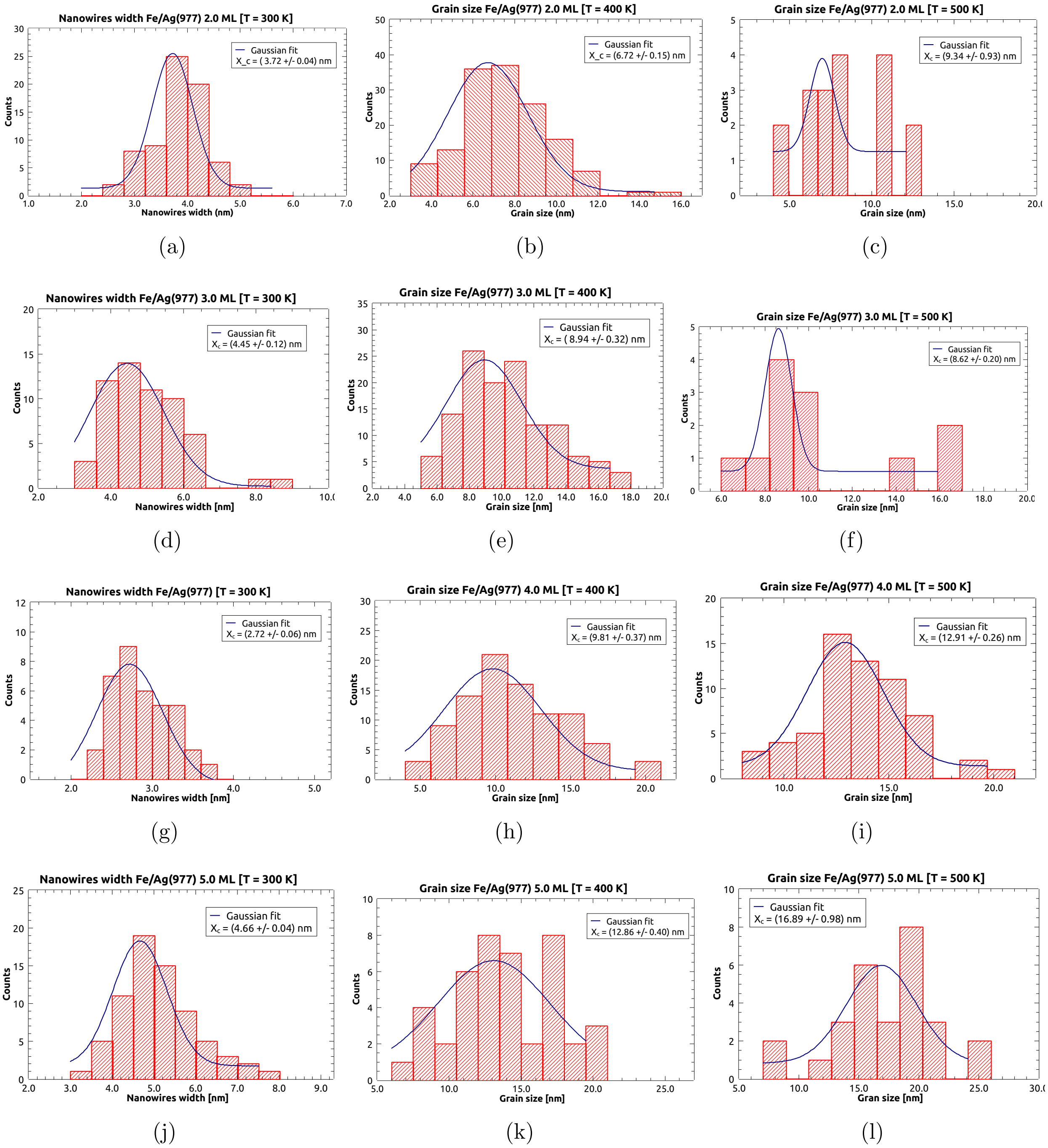

(a) (b) (c)

(d) (e) (f)

(g) (h) (i)

(j) (k) (l)

Figure C.2—Fe/Ag(977) grain size statistic analysis for thickness 2.0, 3.0, 4.0 and 5.0 ML (T_s = 300K, 400K, 500K).

For evaporation between 2.0 ML and 5.0 ML at room temperature, we measured the length of each of the nanostructures that resemble nanowires. In figure C.3, we present the statistic distributions of these structures, in figures C.5 and C.6 the space between them and their height, respectively. In figure C.4 we present the linear profile of a STM image of nanowires for 2.0 ML Fe/Ag(977).

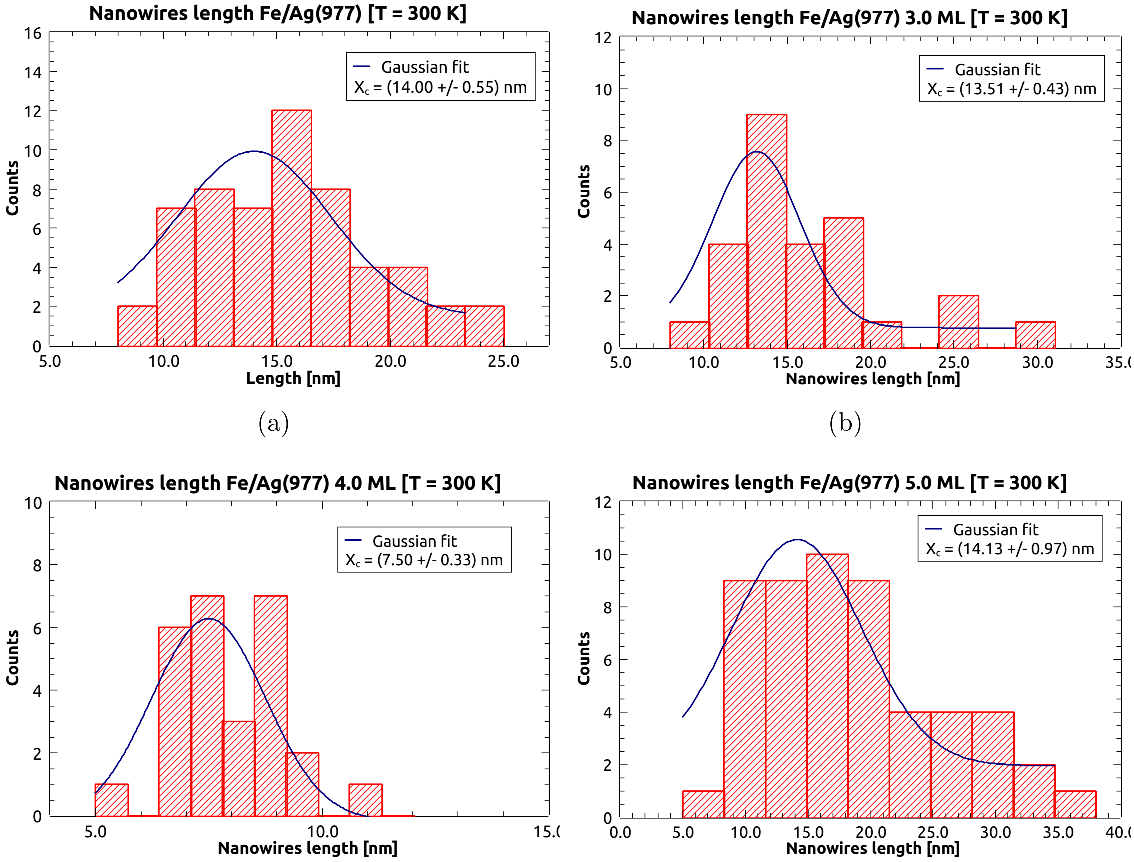

(a)

(b)

(c)

(d)

Figure C.3—Elongated structures length.

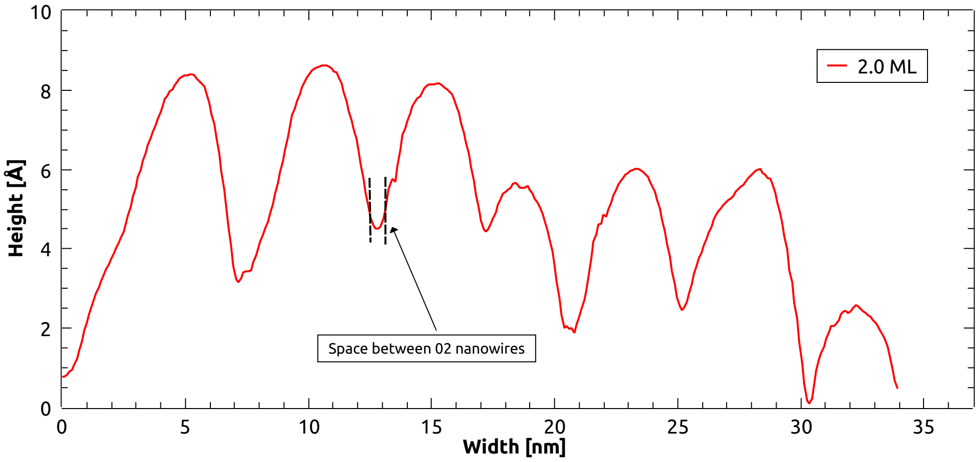

Figure C.4—Linear profile of elongated structures.

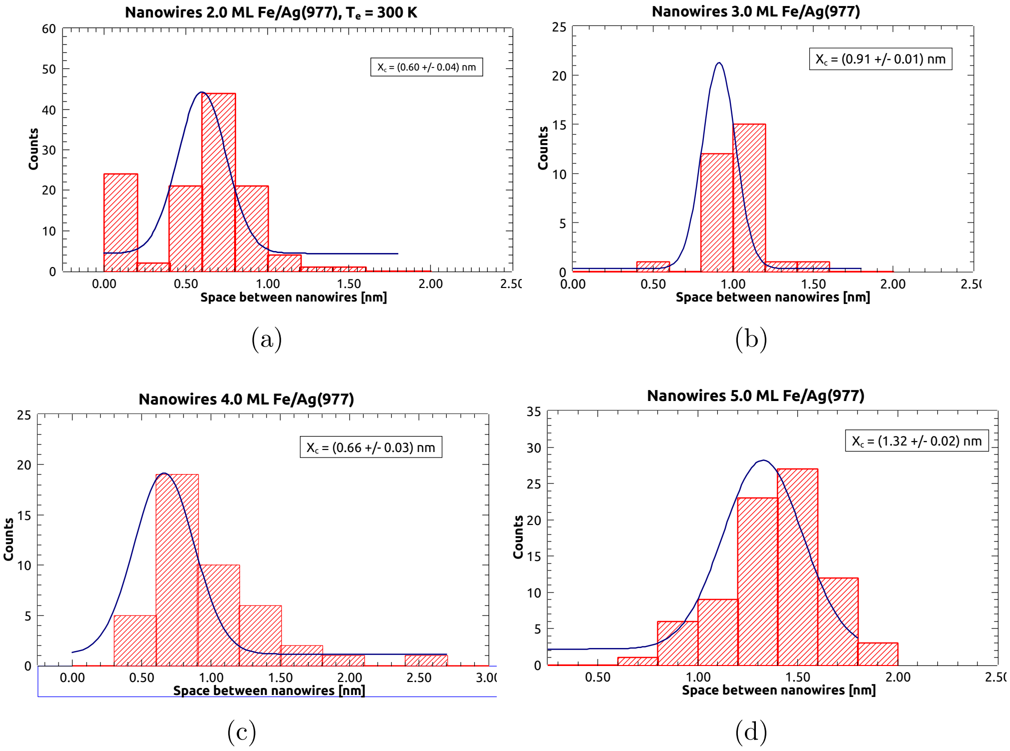

(a) (b)

(c) (d)

Figure C.5—Space between elongated structures.

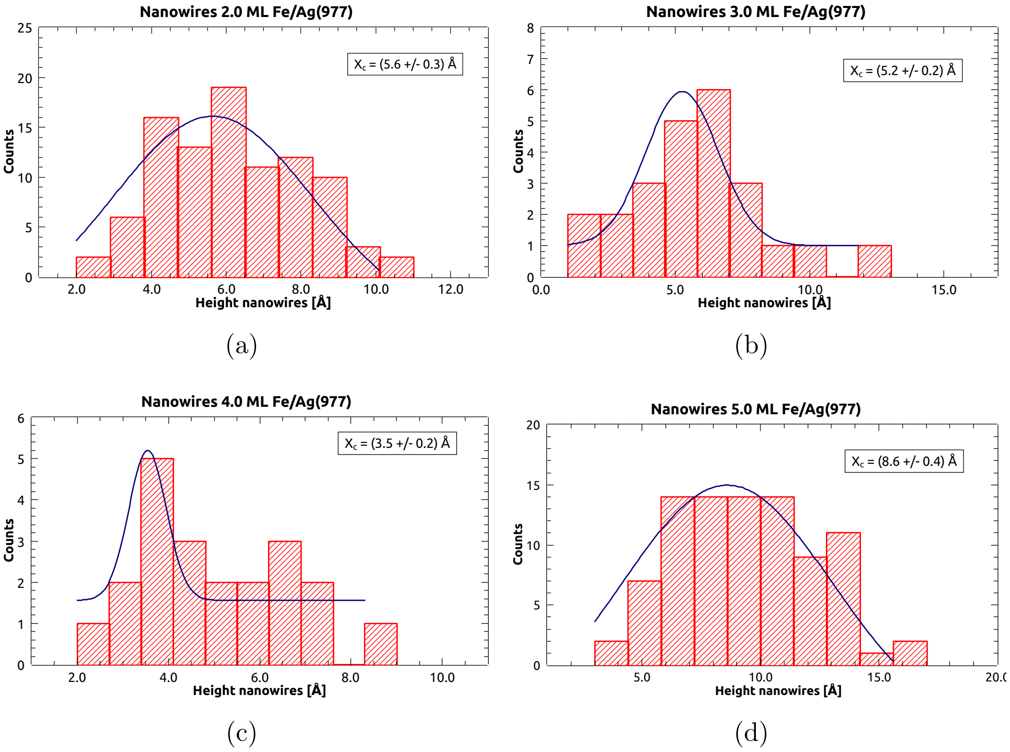

(a) (b)

(c) (d)

Figure C.6—Height elongated structures.

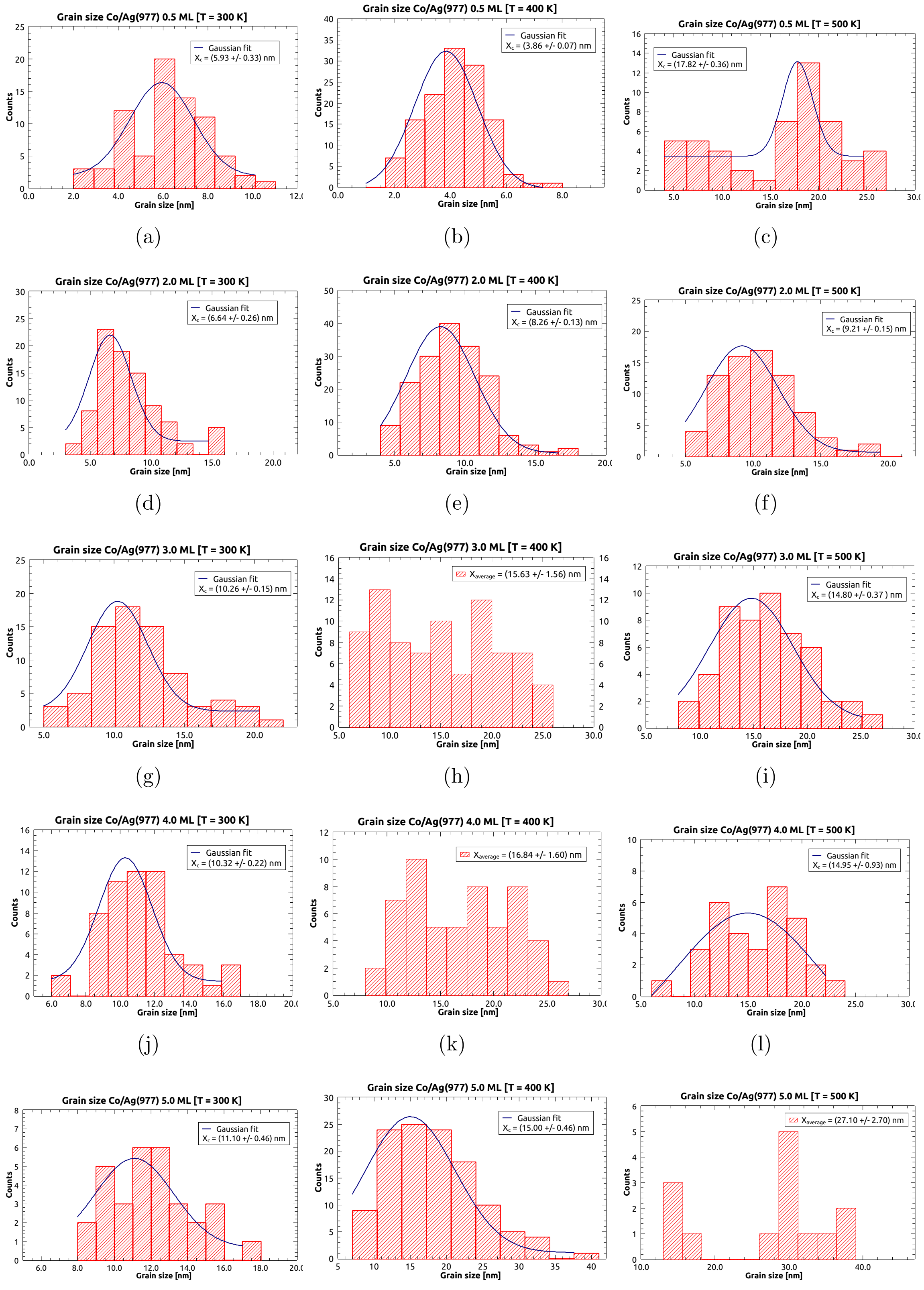

(a) (b) (c)

(d) (e) (f)

(g) (h) (i)

(j) (k) (l)

(m) (n) (o)

Figure C.7—Co/Ag(977) grain size statistic analysis for thickness between 0.5 ML and 5.0 ML.

Appendix D

Graphics - Normalized Kerr magnetometry

This appendix is dedicated to present the Kerr magnetometry results (see chapter 5). The magnetization direction is given by $\mathbf{M}/M_s = m_x\hat{i} + m_y\hat{j} + m_z\hat{z}$. The m_y, m_z are the magnetization components in-plane and out-plane, respectively.

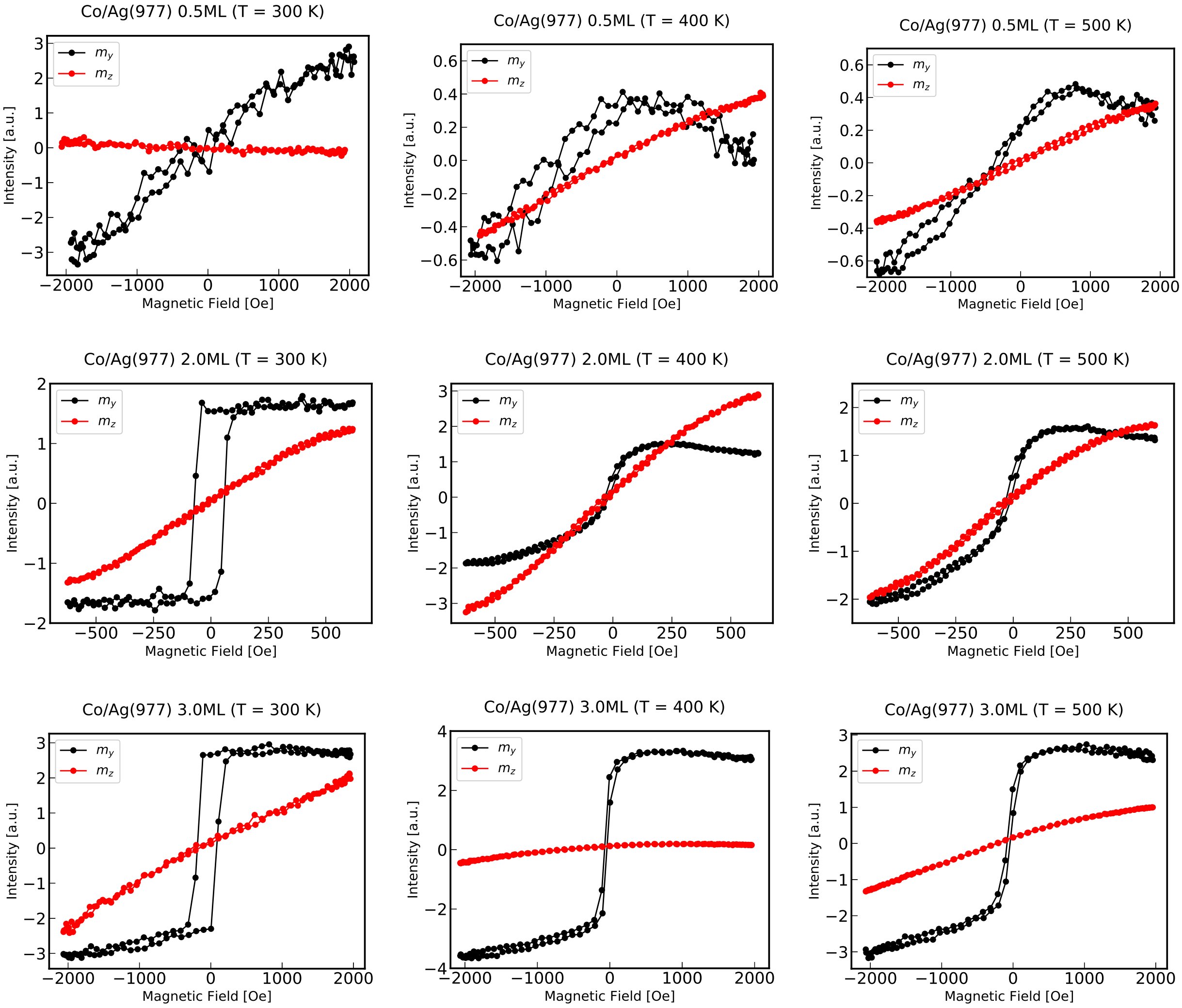
Co/Ag(977) 0.5ML (T = 300 K)

Co/Ag(977) 0.5ML (T = 400 K)

Co/Ag(977) 0.5ML (T = 500 K)

Co/Ag(977) 2.0ML (T = 300 K)

Co/Ag(977) 2.0ML (T = 400 K)

Co/Ag(977) 2.0ML (T = 500 K)

Co/Ag(977) 3.0ML (T = 300 K)

Co/Ag(977) 3.0ML (T = 400 K)

Co/Ag(977) 3.0ML (T = 500 K)

Figure D.1—m_y and m_z as a function of the applied magnetic field as determined by Kerr magnetometry for 0.5 ML, 2.0 ML and 3.0 ML on Co/Ag(977) at 300K, 400K and 500K.

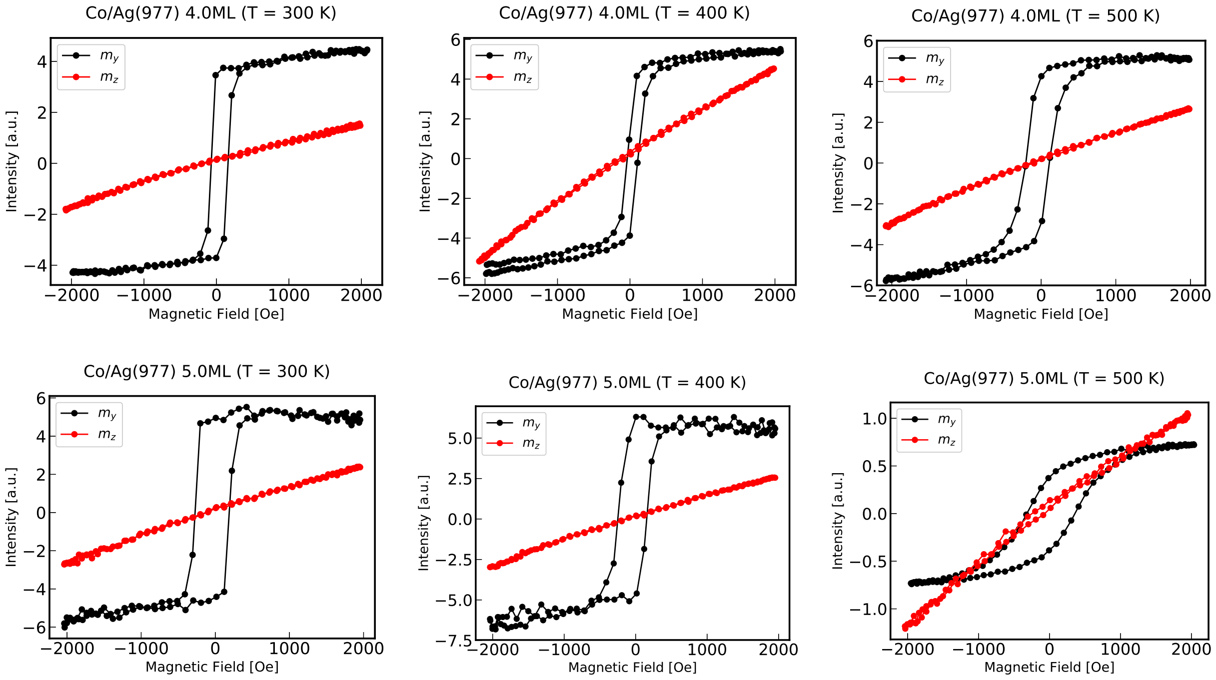

Figure D.2—m_y and m_z as a function of the applied magnetic field as determined by Kerr magnetometry for 4.0 and 5.0 ML on Co/Ag(977) at 300K, 400K and 500K.

Bibliography

[1] I. Ennen, D. Kappe, T. Rempel, C. Glenske, and A. Hütten, "*Giant magnetoresistance: Basic concepts, microstructure, magnetic interations and applications*", Sensors Review, **16**, no. 904, 1-24, (2016).

[2] X.-B. Chen, N. T. M. Hien, K. Han, J.-Y. Nam, N. T. Huyen, S.-I. Shin, X. Wang, S. W. Cheong, D. Lee, T. W. Noh, N. H. Sung, B. K. Cho, and I.-S. Yang, "*Study of spin-ordering and spin-reorientation transitions in hexagonal manganites through Raman spectroscopy*", Nature - Scientific Reports, **5**, no. 13366, 1-8, (2015).

[3] U. Staub, L. Rettig, E. M. Bothschafter, Y. W. Windsor, M. Ramakrishnan, S. R. Avula-Venkata, J. Dreiser, C. Piamonteze, V. Scagnoli, S.Mukherjee, C. Niedermayer, M. Medarde, and E. Pomjakushina, "*The spin-reorientation transition in* TmFeO*3*", Physical Review B, **96**, no. 174408, 1-11, (2017).

[4] A. Mukhtar, X. C. K. Wu, and L. Gu, "*Magnetic nanowires in biomedical applications*", Nanotechnology, **31**, no. 433001, 1-40, (2020).

[5] M. A. Moradiya, A. Ladani, J. Ladani, C. Raiyani, and J. Markna, "*New Way to Treat Cancer: Magnetic Nanoparticle based Hyperthermia*", Journal of Chemical Science and Engineering, **2**, no. 1, 58-60, (2019).

[6] K. Simeonidis, M. Morales, M. Marciello, M. Angelakeris, P. de la Presa, A. Lazaro-Carrillo, A. Tabero, A. Villanueva, O. Chubykalo-Fesenko, and D. Serantes, "*In-situ particles reorientation during magnetic hyperthermia application: Shape matters twice*", Nature: Scientific reports, **6**, no. 38382, 1-11, (2016).

[7] J. Jose, R. Kumar, S. Harilal, G. Mathew, D. Parambi, A. Prabhu, M.Uddin, L. Aleya, H. Kim, and B. Mathew, "*Magnetic nanoparticles for hyperthermia in cancer treatment:an emerging tool*", Nanotechnology, Nanopollution, Nanotoxicology and Nanomedicine, **27**, 19214–19225, (2020).

[8] P. Malik, S. Pandya, and V. Katyal, "*Synthesis and application of magnetic nanomaterials for memory storage devices*", International Journal of Advance Research, **27**, 1-28, (2013).

[9] R. Lebrun, S. Tsunegi, P. Bortolotti, H. Kubota, A. S. Jenkins, M. Romera, K. Yakushiji, A. Fukushima, J. Grollier, S. Yuasa, and V. Cros, "*Mutual synchronization of spin torque nano-oscillators through a long-range and tunable electrical coupling scheme*", Nature Communications, **8**, no. 15825, 1-7, (2017).

[10] A. Jenkins, R. Lebrun, E. Grimaldi, S. Tsunegi, P. Bortolotti, H. Kubota, K. Yakushiji, A. Fukushima, G. de Loubens, O. Klein, S. Yuasa, and V. Cros, "*Spin-torque resonant*

expulsion of the vortex core for an efficient radiofrequency detection scheme", Nature Nanotechnology, **11**, 360-364, (2016).

[11] V. Kalyani and V. Agrawal, "*Spintronics- A Vision for Future in Electronics and Computers*", Journal of Management Engineering and Information Technology, **2**, 30-36, (2015).

[12] Y. Henry, K. Ounadjela, L. Piraus, S. Dubois, J. George, and J. Duvail, "*Magnetic anisotropy and domain patterns in electrodeposited cobalt nanowires*", European Physical Journal, **20**, 35-44, (2001).

[13] J. Sánchez-Barriga, M. Lucas, F. Radu, E. Martin, M. Multigner, P. Marin, A. Hernando, and G. Rivero, "*Interplay between the magnetic anisotropy contributions of cobalt nanowires*", Physical Review B, **80**, no. 184424, 1-8, (2009).

[14] P. Landeros, S. Allende, J. Escrig, E. Salcedo, D. Altbir, and E. Vogel, "*Reversal modes in magnetic nanotubes*", Applied Physics Letters, **90**, 102501–102503, (2007).

[15] R. A. Marbrow and R. M. Lambert, "*Adsorption-desorption properties, coadsorption and surface chemistry of chlorine and oxygen on* A*g(331)*", Surface Science, **71**, 107-120, (1978).

[16] A. Riemann, B. N.Satterwhite, and B. E. Owens, "*Metallic thin film growth on vicinal* C*u substrates*", Surface Science, **604**, 2157-2162, (2010).

[17] M. Elsen, J. H. Gao, V. Repain, C. Chacon, Y. Girard, J. Lagoute, G. Rodary, J. Ferré, and S. Rousset, "*Discontinuous vs. continuous spin reorientation transition of magnetic films on vicinal surfaces*", Europhysics Letters, **88**, no. 27006, 1-6, (2009).

[18] A. Bellec, Y. Garreau, J. Creuze, A. Vlad, F. Picca, M. Sauvage-Simkin, and A. Coati, "*textscAg on a* N*i vicinal surface: Coupling Stranski-Krastanov and "magic" heteroepitaxial growth*", Physical Review B, **96**, no. 085414, 1-6, (2017).

[19] M. Shipilin, J. Gustafson, C. Zhang, L. R. Merte, and E. Lundgren, "*Step dynamics and oxide formation during* CO *oxidation over a vicinal* P*d surface*", Physical Chemistry Chemical Physics, **18**, 20312-20320, (2016).

[20] R. L. Park and H. E. Farnsworth, "*The structures of clean nickel crystal surfaces*", Surface Science, **2**, 527-533, (1964).

[21] R. L. Schwoebel and E. J. Shipsey, "*Step motion on crystal surfaces*", Journal of Applied Physics, **37**, no. 10, 3682-3686, (1966).

[22] W. P. Ellis and R. L. Schwoebel, "LEED *from surface steps on* U0*2 single crystals* ", Surface Science, **11**, 82-98, (1968).

[23] B. Lang, R. W. Joyner, and G. A. Somorjai, "*Low Energy Electron Diffraction Studies of High Index Crystal Surfaces of Platinum*", Surface Science, **30**, 440-453, (1972).

[24] C. Barreteau, F. Raouafi, M. C. Desjonquères, and D. Spanjaard, "*Modelling of transition and noble metal vicinal surfaces: energetics, vibrations and stability*", Journal of Physics: Condensed Matter, no. **15**, S3171-S3196, (2003).

[25] T. S. Rahman, A. Kara, and S. Durukanoglu, "*Structural relaxations, vibrational dynamics and thermodynamics of vicinal surfaces*", Journal of Physics: Condensed Matter, **15**, S3197-S3226, (2003).

[26] N. Néel, T. Maroutian, L. Douillard, and H. Ernst, "*Spontaneous structural pattern formation at the nanometre scale in kinetically restricted homoepitaxy on vicinal surface*", Journal of Physics: Condensed Matter, **15**, S3227-S3240, (2003).

[27] J. Shen, R. Skomski, M. Klaua, H. Jenniches, S. Manoharan, and J. Kirschner, "*Magnetism in one dimension:* Fe *on* Cu*(111)* ", Physical Review B, **56**, no. 5, 2340-2343, (1997).

[28] D. Zhao, F. Liu, D. L. Huber, and M. G. Lagally, "*Step-induced magnetic-hysteresis anisotropy in ferromagnetic thin films*", Journal of Applied Physics, **91**, no. 5, 3150-3153, (2002).

[29] D. Repetto, T. Y. Lee, S. Rusponi, J. Honolka, K. Kuhnke, V. Sessi, U. Starke, H. Brune, P. Gambardella, C. Carbone, A. Enders, and K. Kern, "*Structure and magnetism of atomically thin* Fe *layers on flat and vicinal* Pt *surfaces*", Physical Review B, **74**, no. 054408, 1-8, (2006).

[30] J. Araya-Pochet, C. A. Ballentine, and J. L. Erskine, "*Thickness and temperature - dependent spin anisotropy of ultrathin epitaxial* Fe *films on* Ag*(100)*", Physical Review B, **38**, no. 11, 7846-7849, (1988).

[31] F. Broeder, W. Hoving, and P. Bloemen, "*Magnetic anisotropy of multilayers* ", Journal of Magnetism and Magnetic Materials, **93**, 562-570, (1991).

[32] G. Lugert, G. Bayreuther, S. Lehner, G. Gruber, and P. Bruno, "*Magnetic order and structure of ultrathin films and multilayers* ", Material Reserach Symporium, **232**, 97-105, (1991).

[33] M. Maccio, M. Pini, P. Politi, and A. Rettori, "*Spin-Wave magnetization of* Fe*(110)/*Ag*(111) superlattices: Quasi-two-dimensional versus three-dimensional temperature dependence and anisotropy effects* ", Physical Review B, **46**, no. 13, 8276-8281, (1992).

[34] A. Begley, D. Tian, F. Jona, and P. Marcus, "*Study of ultrathin* Fe *films on* Pd*(111),* Ag*(111) and* Al*(111)* ", Surface Science, **280**, 289-297, (1993).

[35] A. Berger and R. Erickson, "*Magnetic phase diagram of ultrathin* Fe/Ag*(100) films near of the reorientation phase transition*", Journal of Magnetism and Magnetic Materials, **165**, 70-73, (1997).

[36] M. Canepa, P. Cantini, O. Ricciardi, S. Terreni, and L. Mattera, "*Temperature effects on morphology and composition of ultrathin heteroepitaxial films:* Fe *on* Ag*(100)*", Surface Science, **429**, 34-45, (1999).

[37] A. Hahlin, C. Andersson, J. Dunn, O. Karis, and D. Arvanitis, "*Structure and magnetism on in situ ultrathin epitaxial films:* XMCD *and* EXAFS *on* Fe/Ag*(100)*", Surface Science, **532**, 76-81, (2003).

[38] A. Hahlin, C. Andersson, J. Dunn, O. Karis, and D. Arvanitis, "*Structure and magnetism of ultrathin epitaxial* Fe *on* Ag*(100)*", Physical Review B, **73**, 1-8, (2006).

[39] K. Doi, E. Minamitani, S. Yamamoto, R. Arafune, Y. Yoshida, S. Watanabe, and Y. Hasegawa, "*Electronic and magnetic effects of a stacking fault in cobalt nanoscale islands on the* Ag*(111) surface*", Physical Review B, **92**, no. 064421, 1-8, (2015).

[40] X. Li, B. Alkadour, W. Chuang, D. Marko, D. Schmool, J. Wu, P. K. Manna, K. Lin, and J. van Lierop, "*Temperature evolution of the magnetic properties of* Ag/Fe *nanodot arrays*", Applied Surface Science, **513**, no. 145578, 1-5, (2020).

[41] T. Wagner, D. R. Fritz, R. Zimmerleiter, and P. Zeppenfeld, "*On the microscopic structure of a nominal* Ag*(441) surface*", Surface Science, **661**, 77-82, (2017).

[42] T. Wagner, D. R. Fritz, Z. Rudolfová, and P. Zeppenfeld, "*Role of step edges on the structure formation of* α*-6*T *on* Ag*(441)*", Surface Science, **667**, 17-24, (2018).

[43] D. Liu and P. A. Thiel, "*Oxygen and sulfur adsorption on vicinal surfaces of copper and silver: Preferred adsorption sites*", The Journal of Chemical Physics, **148**, no. 124706, 1-13, (2018).

[44] B. Cirera, Y. Zhang, J. Bjork, S. Klyatskaya, Z. Chen, M. Ruben, J. V. Barth, and F. Klappenberger, "*Synthesis of Extended Graphdiyne Wires by Vicinal Surface Templating*", Nano Letters, **14**, 1891-1897, (2014).

[45] s. Schmitt, A. Schoell, and E. Umbach, "*Multitude of* PTCDA *Superstructures on* Ag*(111) and Vicinal Surfaces*", Journal of Physical Chemistry C, **121**, 9860-9868, (2017).

[46] F. Pollinger, S. Schmitt, D. Sander, Z. Tian, J. Kirschner, P. Vrdoljak, C. Stadler, F. Maier, H. Marchetto, T. Schmidt, A. Schoell, and E. Umbach, "*Nanoscale patterning, macroscopic reconstruction, and enhanced surface stress by organic adsorption on vicinal surfaces*", New Journal of Physics, **19**, no. 013019, 1-8, (2017).

[47] J. E. Ortega, G. Vasseur, I. Piquero-Zulaica, S. Matencio, M. Valbuena, J. E. Rault, F. Schiller, M. Corso, A. Mugarza, and J. Lobo-Checa, "*Structure and electronic states of vicinal* A*g(111) surfaces with densely kinked steps*", New Journal of Physics, **20**, no. 073010, 1-8, (2018).

[48] D. Mayer and B. Mellish, "Bcc structure. https://en.wikipedia.org/wiki/file:cubic-body-centered.svg."

[49] D. Mayer and B. Mellish, "Fcc structure. https://en.wikipedia.org/wiki/file:cubic-face-centered.svg."

[50] Boris, "Hcp structure. https://commons.wikimedia.org/wiki/file:hexagonal_latticefront.svg."

[51] N. W. Ashcroft and N. D. Mermin, Física do Estado Sólido. Cengage - Learning, (2011).

[52] R. Lizárraga, F. Pan, L. Bergqvist, E. Holmström, Z. Gercsi, and L. Vitos, "*First Principles Theory of the hcp-fcc Phase Transition in Cobalt*", Scientific Reports, **7**, no. 3778, 1-8, (2017).

[53] J. W. M. Frenken and P. Stoltze, "*Are vicinal metal surfaces stable?*", Physical Review Letters, **82**, no. 17, 3500-3503, (1999).

[54] P. Hecquet, "*Stability of vicinal surfaces and role of the surface stress*", Surface Science, **604**, 834–852, (2010).

[55] E. Hahn, A. Fricke, H. Roder, and K. Kern, "*Structure and complete chemical passivation of* P*t(997)*", Surface Science, **297**, 19-26, (1993).

[56] H. Garbouja, M. Saida, F.Picaudb, and Ch.Ramseyer, "*Temperature effects on the growth of the Co adsorbates on* P*t vicinal surface*", Physics Procedia, **2**, 865-872, (2009).

[57] E. Ayietaa, J.Carvella, R. Chenga, and Y. Losovyj, "*Angle resolved photoemission study of surface states on the* P*t(997) vicinal surface*", Physics Letters A, **374**, 3080-3083, (2010).

[58] H. Ibach, Physics of Surfaces and Interfaces. Springer, (2006).

[59] N. Néel, T. Maroutian, L. Douillard, and H.-J. Ernst, "*Spontaneous structural pattern formation at the nanometre scale in kinetically restricted homoepitaxy on vicinal surfaces*", Journal of Physics: Condensed Matter, **15**, S3227–S3240, (2003).

[60] S. Rousset, B. Croset, Y. Girard, G. Prévot, V. Repain, and S. Rohart, "*Self-organized epitaxial growth on spontaneously nano-patterned templates*", C. R. Physique, **6**, 33-46, (2005).

[61] L. Ives, Magnetic mineralogy and fabrics of small-scale glacial flutes, Múlajökull and Breidamerkurjökull. Master dissertation, Iowa State University, (2016).

[62] C. Liu and S. D. Bader, "*Magnetism and growth of ultrathin Co films grown epitaxially on Ru(001)*", Journal of Magnetism and Magnetic Materials, **119**, 81-86, (1993).

[63] S. Bhagwat, R. Thamankar, and F. Schumann, "*Evidence for superparamagnetism in ultrathin Fe and* Fe_xMn_{1-x} *films on Cu(100)*", Journal of Magnetism and Magnetic Materials, **290**, 216-218, (2005).

[64] A. Arora, Optical and electric field control of magnetism. PhD dissertation, Universität Potsdam and Helmholtz Zentrum Berlin, (2018).

[65] M. Getzlaff, Fundamentals of magnetism. Springer, (2008).

[66] E. Hecht, Optics. 5th edition: Pearson, (2015).

[67] F. Pedrotti and P. Bandettini, "*Faraday rotation in the undergraduate advanced laboratory*", American Journal of Physics, **58**, 542-545, (1990).

[68] DrBob, "Faraday effect. https://commons.wikimedia.org/wiki/file:faraday-effect.png."

[69] S. Yamamoto and I. Matsuda, "*Measurement of the Resonant Magneto-Optical Kerr Effect Using a Free Electron Laser*", Applied Science, **662**, no. 7, 1-23, (2017).

[70] J. Kerr, "*On rotation of polarization by reflection from the pole of a magnet*", Philosophical Magazine and Journal of Science, **5S**, no. 19, 319-342, (1877).

[71] W. Wettling, "Magneto-optics of ferrites", *Journal of Magnetism and Magnetic Materials*, **3**, 147-160, (1976).

[72] J. W. Lee, J. R. Jeong, D. H. Kim, J. S. Ahn, J. Kim, and S. C. Shin, "*Three-configurational surface magneto- optical Kerr effect measurement system for an ultrahigh vacuum in situ study of ultrathin magnetic films*", Review of scientific and instruments, **71**, no. 10, 3801-3805, (2000).

[73] S. Visnovský, "*Magneto-Optical permittivity tensor in crystals*", Czechoslovak Journal of Physics B, **36**, 1424–1433, (1986).

[74] M. Champagne, The development of an AC Magneto-Optic Kerr Effect system for the characterization of pulsed laser deposited Co2MnSixAl1-x heusler alloy thin films. Master dissertation, Louisiana State University, (2013).

[75] G. Gomes, Estudo in-situ de filmes magnéticos ultrafinos por magnetometria Kerr e técnicas de superfície. Master dissertation, Universidade Federal de Minas Gerais, (2009).

[76] H. Lüth, Solid Surfaces, Interfaces and Thin Films. Spring, (2010).

[77] Ponor, "Leed pattern. https://commons.wikimedia.org/wiki/file:superstructures_in_low-energy_electron_diffraction_(leed).svg."

[78] G. Binning, H. Rohrer, C. Gerber, and E. Weibel, "*Surface studies by scanning tunneling microscopy*", Physical Review Letters, **49**, 57-61, (1982).

[79] Schmid and Pietrzak, "https://commons.wikimedia.org/wiki/file:rastertunnelmikroskop-schema.svg."

[80] I. Horcas, R. Fernández, J. M. Gómez-Rodríguez, J. Colchero, J. Gómez-Herrero, and A. M. Baro, "WSXM*: A software for scanning probe microscopy and a tool for nanotechnology*", Review of Scientific Instruments, **78**, no. 013705, 1-8, (2007).

[81] K. Merazzo, Ordered magnetic antidot arrays. PhD thesis, Instituto de Ciencia de Materiales de Madrid, (2012).

[82] R. Osgood, S. Bader, B. Clemens, R. White, and H. Matsuyama, "*Second-order magneto-optic effects in anisotropic thin films*", Journal of Magnetism and Magnetic Materials, **182**, 297-323, (1998).

[83] P. Gambardella, M. Blanc, H. Brune, K. Kuhnke, and K. Kern, "*One-dimensional metal chains on* P*t vicinal surfaces*", Physical Review B, **61**, no. 3, 2254-2262, (2000).

[84] P. Gambardella, M. Blanc, L. Bürgi, K. Kuhnke, and K. Kern, "C*o growth on* P*t(997): from monatomic chains to monolayer completion*", Surface Science, **449**, 93-103, (2000).

[85] V. Repain, J. Berroir, S. Rousset, and J. Lecoeur, "*Growth of self-organized cobalt nanostructures on* A*u(111) vicinal surfaces*", Surface Science, **447**, L152-L156, (2000).

[86] P. Gambardella and K. Kern, "*Ni growth on vicinal* P*t(111): low temperature exchange and formation of ordered surface alloys*", Surface Science, **745**, L229-L234, (2001).

[87] P. Gambardella, A. Dallmeyer, K. Maiti, M. C. Malagoli, W. Eberhardt, K. Kern, and C. Carbone, "*Ferromagnetism in one-dimensional monatomic metal chains*", Nature, **416**, 301–304, (2002).

[88] H. J. Elmers, J. Hauschild, H. Höche, U. Gradmann, H. Bethge, D. Heuer, and U. Köhler, "*Submonolayer Magnetism of* F*e(110) on* W*(110): Finite Width Scaling of Stripes and Percolation between Islands*", Physical Review Letters, **73**, no. 6, 898-901, (1994).

[89] T. Jung, R. Schlittler, J. Gimzewski, and F. Himpsel, "*One-dimensional metal structures at decorated steps*", Applied Physics A, **61**, 467-474, (1995).

[90] J. Shen, J. P. Pierce, E. W. Plummer, and J. Kirschner, "*The effect of spatial confinement on magnetism: films, stripes and dots of* Fe *on* Cu*(111)*", Journal of Physics: Condensed Matter, **15**, R1-R30, (2003).

[91] C. ViolBarbosa, J. Fujii, G. Panaccione, and G. Rossi, "*Structure and magnetism of self-assembled Fe nanowires on a faceted* cu*(32) surface: the influence of oxygen-induced reconstruction*", New Journal of Physics, **11**, no. 113046, 1-10, (2009).

[92] R. Cheng, K. Y. Guslienko, F. Y. Fradin, J. E. Pearson, H. F. Ding, D. Li, and S. D. Bader, "*Step-decorated ferromagnetic* Fe *nanostripes on* Pt*(997)*", Physical Review B, **72**, no. 014409, 1-7, (2005).

[93] E. Jal, M. D. abrowski, J. M. Tonnerre, M. Przybylski, S. Grenier, N. Jaouen, and J. Kirschner, "*Noncollinearity of the canted spins across ultrathin* Fe *films on vicinal* Ag *surfaces*", Physical Review B, **91**, no. 214418, 1-8, (2015).

[94] S. Rohart, Y. Girard, Y. Nahas, V. Repain, G. Rodary, A. Tejeda, and S. Rousset, "*Growth of iron on gold (788) vicinal surface: From nanodots to step flow*", Surface Science, **602**, 28-36, (2008).

[95] V. Repain, G. Baudot, H. Ellmer, and S. Rousset, "*Two-dimensional long-range–ordered growth of uniform cobalt nanostructures on a* Au*(111) vicinal template*", Europhysics Letters, **58**, no. 5, 730-736, (2002).

[96] T. Lee, S. Sarbach, K. Kuhnke, and K. Kern, "*Growth and surface alloying of* Fe *on* Pt*(997)*", Surface Science, **600**, 3266-3273, (2006).

[97] G. Baudot, S. Rohart, V. Repain, H. Ellmer, Y. Girard, and S. Rousset, "*Temperature dependence of ordered cobalt nanodots growth on* Au*(788)*", Applied Surface Science, **212**, 360-366, (2003).

[98] A. Li, F. Liu, D. Y. Petrovykh, J.-L. Lin, J. Viernow, F. J. H. im psel, and M. G. . Lagally, "*Creation of "Quantum Platelets" via Strain-Controlled Self-Organization at Steps*", Physical Review Letters, **85**, no. 25, 5380-5383, (2000).

[99] K. Morgenstern, J. Kibsgaard, J. V. Lauritsen, E. Lægsgaard, and F. Besenbacher, "*Cobalt growth on two related close-packed noble metal surfaces*", Surface Science, **601**, 1967-1972, (2007).

[100] C. Lin, S. LinTsay, C. RongChen, X. LanHuang, and T. YiFu, "*Size Control of Co Islands Grown on* Ag/Ge*(111) Surface*", Journal of Nanoscience and Nanotechnology, **10**, 1-5, (2010).

[101] M. Wasniowska, W. Wulfhekel, M. Przybylski, and J. Kirschner, "*Submonolayer regime of Co epitaxy on Pd(111): Morphology and electronic structure*", Physical Review B, **78**, no. 035405, 1-8, (2008).

[102] G. Gumarov, A. Alekseev, and V. Petukhov, "*Magnetic properties of iron silicide films ion-synthesized in the field of mechanical stresses*", Journal of Magnetism and Magnetic Materials, **487**, no. 165322, 1-5, (2019).

[103] P. Anikeeva, G. Beach, and N. Holten-Andersen, Electronic, Optical and Magnetic Properties of Materials. https://ocw.mit.edu: Spring - Massachusetts Institute of Technology: MIT OpenCourseWare, (2013).